·ISSN : 2372-0484

AIMS Materials science

VOLUME NO. 10
ISSUE NO. 3
SEPTEMBER - DECEMBER 2023

EIS LEARNING
No - 198, Upper Hatia, Near Mahatma Gandhi
Smarak High School, Ranchi - 834003, Jharkhand
Ph : 919097302256 / Email : info@eislearning.com

·ISSN : 2372-0484

AIMS Materials science

AIM AND SCOPE

AIMS Materials science is an international journal devoted to publishing peer-reviewed, high quality, original papers in the field of Materials science. We publish the following article types: original research articles, reviews, editorials, letters, and conference reports.

AIMS Materials Science welcomes, but not limited to, the papers from the following topics:

- Biological materials
- Ceramics
- Composite materials
- Magnetic materials
- Medical implant materials
- New properties of materials
- Nanoscience and nanotechnology
- Polymers
- Thin films

·ISSN : 2372-0484

Editor in Chief

·ISSN : 2372-0484

·ISSN : 2372-0484

·ISSN : 2372-0484

·ISSN : 2372-0484

·ISSN : 2372-0484

AIMS Materials science

(Volume No. 10, Issue No. 3, September-December 2023)

Contents

·ISSN : 2372-0484

Numerical Simulations of Gradient Cooling Technique for Controlled Production of Dierential Microstructure in Steel Strip or Plate

Aarne Pohjonen*
Materials and Mechanical Engineering, Faculty of Technology, University of Oulu, PL4200, 90014 Oulun Yliopisto Oulu, Finland
* Correspondence: Email: Aarne.Pohjonen@Oulu.fi; Tel: +358505974261.

ABSTRACT

Numerical studies were conducted to investigate the applicability of cooling strategies for controlledly producing a microstructure in the steel strip or plate, which changes as function of the plate length. In the numerical simulations, the water spray cooling was varied as function of the plate length and as a result, the dierent parts of the plate were cooled at dierent rates. We applied the previously developed numerical code where the transformation latent heat is coupled with the heat conduction and transfer model, which has also been calibrated to correspond to experimental laboratory cooling line. The applicability of the method was investigated for controlledly creating alternating bainite and polygonal ferrite regions in plates of two dierent thicknesses (0.8 cm and 1.2 cm thick plates) by cooling dierent parts of the plate to dierent temperatures before switching o the water cooling so that polygonal ferrite forms in the part which has been cooled to higher temperature and bainite forms in the low temperature part. The simulation results indicate that the controlled production of such alternating regions is possible, but the resulting regions in the studied scenario cannot be very thin. The transition regions between the ferrite and bainite regions in the simulated cases are in the range of 5–15 cm. Controlled production of zones consiting of softer phase in the otherwise bainitic steel could oer a possibility for creating designed tracks in a steel bainitic strip or plate, where the mechanical working or cutting of the material is easier.

Keywords: modelling; numerical simulations; dierential treatment; temperature control; phase transformations; steel

1. INTRODUCTION

Controlled dierential treatment of materials oer possibility for tailoring the mechanical properties of the finished or semi-finished part to be suited for a specific application purpose. Dierential treatment can include both local mechanical deformation and local temperature control [1, 2]. As an example, dierential heating and cooling has been used in context of hot stamping for producing B-pillars for automobiles, which require high strength at the upper part and lower strength and high plasticity under crash conditions at the lower part. This is achieved by controlling the local temperature of the applied mold [3]. Phase transformations in hot stamping process have been investigated with numerical simulations in [4]. Dierential heat treatment has also been used to adjust the mechanical properties of rails by controlling local cooling rate by using controlled mixing of water and air [5].

During dierential cooling, distortions can occur since the thermal dilatation and volume changing transformations can occur at dierent places at dierent times [6].

In order to control the formation of microstructure during thermomechanical processing, it is very useful to apply numerical simulation methods that are calibrated to correspond to the experimental setting. The

virtual experimentation then allows for finding the optimal processing route to meet the needs of a specific application purpose. With the use of the calibrated numerical simulation tools, the thermomechanical treatment of initial material can be optimised to produce the required position dependent mechanical properties in the final product. In the current study, the previously developed and calibrated numerical models for water cooling of steel plate or strip are applied to study the method of producing dierential microstructures during cooling by virtual experimentation. In the current context the microstructure was designed to change within centimeter length scale from ferritic to bainitic microstructure. The terms dierential treatment and dierential microstructure are therefore applied to describe the dierences within this length scale in the current study, in the same way as in [1].

The focus of the current study is in application of the numerical modelling to see the feasibility of the approach and the approximate length scales that could be expected for the alternating polygonal ferrite/bainite regions. For the precise control of the regions in applied setting, also experimental trials will be needed to adjust the model parameters to describe the heat transfer corresponding to the cooling devices and the phase transformations occuring in a given steel grade. In the current study the previously developed phase transformation model [7, 8] is fully coupled with heat transfer and coduction model [9–11]. The heat transfer between the water and the steel has been calibrated to correspond to the experimental laboratory water cooling line [12].

The models have been previously used succesfully in the context of simulating phase transformations occuring during cooling of coiled steel strip [13], design of induction hardening of a slurry pipe [14] and for producing ultrafine-structured bainite in a steel plate [15]. In the current article, water cooling is studied as a method for producing the dierential cooling rates, but also dierent cooling methods, such as air cooling [16], mixed air–water [5] or metal contact cooling [17] could be modelled similarly, when the respective heat transfer coecients are known. Using the numerical model, it was possible to simulate cooling strategies that can be used for creating alternating polygonal ferrite and bainite regions in steel plate or strip.

2. MATERIALS AND METHODS

Current study focuses on the numerical simulations applying the previously published numerical model, described in [9] and [10]. The phase transformation model is based on [7,18]. The model steel applied in the numerical simulations is described in [10]. The steel composition in wt% was 0.052 C, 0.19 Si, and Mn + Cr = 1.9. In the experiments that were used for the model parameterization (cooling rates from 2 to 90 oC/s), only ferrite and bainite were observed to form. To provide an overview of the numerical method, the model is briefly described also here, while the details can be found in the previous publications.

As described in detail in [7, 8], and originally in [19], the transformation onset (assumed to correspond to 1% of austenite transformed to ferritic phase) is calculated with applying the rule of Scheil, i.e. the transformation starts when $\sum_i \frac{\Delta t}{\tau(T)} = 1$, where Δt is the simulation time-step. The function (T) descibed in Eq (2.1) is the time that would be required for the transformation to start during isothermal holding.

$$\tau(T) = K(A - T)^{-m} \exp\left(\frac{Q}{R(T + 273.15)}\right) \tag{2.1}$$

where T is the temperature in °C, A is the limiting temperature for transformation to occur (Ae3 temperature for ferrite and bainite start temperature for bainite), Q is the activation energy for transformation, K and m are fitting parameters. Similar form has been applied already by Kirkaldy [20].

The carbon concentration dependent equilibrium temperature Ae3 defines the condition for ferrite formation above the eutectoid temperature. Ferrite can hold only up to 0.02 wt% carbon. When ferrite forms, the excess carbon is partitioned to the surrounding austenite. When the carbon concentration in the austenite is suciently high, so that the local temperature exceeds the Ae3 line, the transformation stops. Below the eutectoid temperature, the maximum ferrite volume fraction is defined by the extrapolated Acm line. These conditions define the temperature dependence of the maximum ferrite fraction that can be transformed from the austenite. The maximum transformed fraction is denoted as max. The carbon concentration dependent equlibrium lines, Ae3 and Acm were calculated using the equations described in [10, 18], but they could also be obtained using thermodynamic softwares.

The transformation kinetics after the onset are calculated applying the Eq (2.2).

$$\frac{d\chi}{dt} = (\chi_{\max} - \chi)\left[\ln\left(\frac{\chi_{\max}}{\chi_{\max} - \chi}\right)\right]^{\frac{n-1}{n}} k^{1/n} \tag{2.2}$$

where $\frac{d\chi}{dt}$ is the transformation rate, χ the previously transformed volume fraction, k the temperature dependent rate parameter and n the Avrami exponent. The maximum fraction takes in to account the remaining austenite, and for the polygonal ferrite the thermodynamical equilibrium fraction for ferrite formation. To model the temperature dependence of the rate parameter, and the eect of carbon on slowing down the bainite formation, we applied the Eq (2.3)

$$\begin{aligned} k_\alpha &= \exp(-a_\alpha(T - b_\alpha)^2 - c_\alpha) \quad \text{for ferrite,} \\ k_b &= \frac{C}{C_\gamma}\exp(-a_b(T - b_b)^2 - c_b) \quad \text{for bainite.} \end{aligned} \tag{2.3}$$

as described in [9, 10]. Formation of the martensite fraction χ_m was simulated using the Koistinen-Marburger Eq (2.4), where the martensite start temperature M_S was calculated using the Stuhlmanns equation [21] and the usual parameter $\eta = 0.011$ was used.

$$\chi_m = [1 - \exp(-\eta(M_S - T))]\chi_{\max} \tag{2.4}$$

The fitted numerical parameters, obtained in the previous study [10] by numerical fitting to continuous cooling experiments, are given in Table 1. These parameters were applied for the phase transformation modelling in the current study.

Table 1. Numerical model parameters.

Product	K	A (°C)	m	Q (kJ)	a	b (°C)	c	n
Ferrite (α)	5.712×10^{-4}	833.8	2.956	184.6	2.079×10^{-4}	775.8	6.359	1.60
Bainite (b)	9.343×10^{-4}	652.7	0.3181	60.0	3.036×10^{-4}	452.2	0.250	2.21

The heat transfer and conduction model, as well as coupling of the latent heat release from the phase transformations was described in detail in our previous publications [9,10]. Briefly, the 2-dimensional heat Eq (2.5) was solved using explicit finite dierence method, which was implemented in Fortran language and parallelized using OpenMP library to enable ecient calculation speed.

$$\rho c\frac{\partial}{\partial t}T = \nabla \cdot (\kappa \nabla T) + s \tag{2.5}$$

where κ is the heat conductivity, t time, and s the latent heat released due to the phase transformations,

which is calculated as described in [10, 22, 23]. The determination of the heat transfer coecient for the laboratory water cooling line is described in [12]. In the rectangular finite dierence discretization the plate length (0.564 m) was divided in to 600 segments in the horizontal x-direction. In the vertical y-direction, the plate thickness was divided in to 80 segments for the 1.2 cm and in to 60 segments for the 0.8 cm plate. The simulation timestep was 0.2 ms.

The material is assumed to be initially fully homogenous in the austenitic state in the beginning of the simulation. The initial temperature of the cooled strip/plate is 1000 oC. Two types of dierential cooling cases were investigated with numerical simulations described in Sections 2.1 and 2.2. The hypothetical simulated cooling line is defined as having periodic array of water sprays placed regularly apart from each other, with separation distance equal to the plate length x. The strip/plate proceeds with a speed of 0.3 m/s at the cooling line. The dierence to the actual laboratory water spray cooling line applied in the calibration [12] is that in the real laboratory cooling line, the strip/plate direction is changed periodically (because the short scale of the cooling line), as in the current numerical study the strip/plate propagates continuously in the negative x-direction, corresponding a long line of periodic water sprays.

2.1. Simulation case 1: step interruption in cooling

In the first studied case, the purpose was to see the size of a ferritic region that can be created to the strip/plate by leaving a short segment of the strip/plate at higher temperature, while cooling rest of the strip/plate to the bainitic formation temperature. Figure 1 schematically illustrates the geometry of the strip/plate moving towards left in a cooling line subjected to cooling by periodic array of water sprays, as well as the simulated water cooling strategy for dierent segments of the plate.

Initially the whole plate is subjected to the water spray cooling with water flux of 6.8 L/m2s. Once the temperature of the plate is in the region where polygonal ferrite forms (700–780 oC), the step interruption in the cooling is applied, as depicted in Figure 1: the regions A and C are still subjected to water spray cooling, but when the region B is below the water spray, the spray is turned o, so that this region cools only by conduction towards the regions A and C, and by radiation and convection towards the surface directions (up and down in the Figure 1). The formation of ferrite and bainite causes release of latent heat, which is included in the simulation. Once the regions A and C are cooled to the bainitic formation temperature, no further water cooling is subjected to these regions, so that the whole plate cools by radiation and convection, and internally by conduction within the plate.

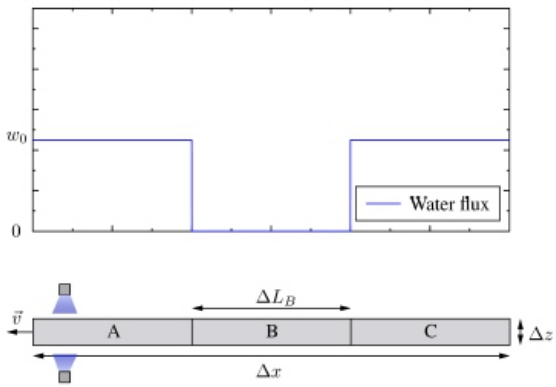

Figure 1. In the simulated case 1, the water cooling was interrupted for the segment B, while segments A and C were subjected to water spray cooling. The strip/plate propagates with velocity ~v. The simulations were conducted with altering LB and z. Constant plate length x = 56:4 cm was used in the simulations. The water flux !0 = 6:8 L=m2s.

To see how the size of the region B aects the resulting ferrite fraction in this region, simulations were conducted with dierent lengths of the region, LB = 2, 4, 6, 8 and 10 cm. To see how the thickness z of the strip/plate aects the resulting ferrite fraction, the simulations were conducted with the z = 0.8 cm and 1.2 cm thick strip/plate geometries.

2.2. Simulation case 2: gradual change in cooling

In the second investigated case, the purpose was to see how the gradual change in the cooling rate along the lengthwise x-direction of the strip/plate can be utilized to produce smoothly changing microstructure within the plate/strip in this direction. This was realized by changing the simulated water flux gradually from the left side of the plate to the right end of the plate for each water spray in the periodic water spray cooling line, as indicated in Figure 2. The left part (segment A) of the plate is cooled with lower water flux, !1 = 6.8 L=m2s. The mid part (segment B) is subjected to linearly rising water flux, and when the right part (segment C) of the plate is under the water spray, higher water flux !2 = 14.1 L=m2s is used to cool this part of the plate. This cooling procedure is repeated every time the plate passes through the water spray zone, so that the segment A is cooled at lower rate and segment C at higher rate and the cooling rate changes gradually within the segment B. The cooling is continued until the right part of the plate is at the bainite formation temperature (600 oC) and the left part of the plate is at the ferrite formation temperature (700–780 oC). Once this temperature distribution has been reached, the cooling is stopped so that the whole plate is cooled only by radiation and convection, and internally by conduction within the plate.

To see how the size of the region B aects the resulting ferrite fraction in this region, simulations were conducted with dierent lengths, LB = 56.4, 28.2, 14.1, 7.0 and 3.5 cm. To see how the thickness z of the strip/plate aects the resulting ferrite fraction, the simulations were conducted with the z = 0.8 cm and 1.2 cm thick strip/plate geometries.

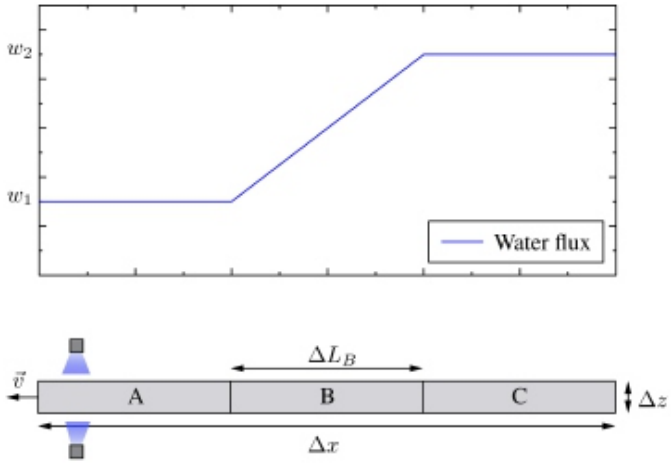

Figure 2. In the simulated case 2, the water flux was linearly changed from lower value w1 = 6.8 L=m2s to higher value w2 = 14.1 L=m2s when the segment B is under the water spray. The strip/plate propagates with velocity ~v. The simulations were conducted with altering LB and z. Constant plate length x = 56:4 cm was used in the simulations.

3. RESULTS AND DISCUSSION

To illustrate the simulated temperature distribution resulting from the water cooling in the two studied cases, the distribution is shown in Figure 3 for dierent simulation snapshots for both studied cases. The snapshots show the distribution when the plate passes through the water spray cooling region.

The Figure 3a–c depict case 1 (step interruption) and Figure 3d–f depict case 2 (gradual change). To quantitatively illustrate the temperature changes at dierent locations, the temperature is plotted along the horizontal x-direction at the upper surface, sub-surface and in the middle of the plate/strip. The Figure 3a–c show the temperature distribution in the snapshots when the plate passes below the water spray. The spray is turned o when region B (desribed in Figure 1) is in the spray cooling zone, which causes temperature to stay higher in this region. The water spray causes sharp drop in temperature on the surface, but a shallow descent in the mid thickness of the strip, in coherence with the previous study [12].

The Figure 3d–f describe the simulation case 2, where the water flux is gradually changing. In the simulated case depicted in the Figure 3d–f, the length of the region B (described in Figure 2), LB, equals to the whole plate length in this simulation. As the water flux rises when the plate proceeds under the spray, the magnitude of the temperature drop increases. When the temperature drops below the martensite start temperature, the formation of martensite releases latent heat, which slows down the temperature drop at the surface. Also the latent heat released due to polygonal ferrite and bainite transformations are included in the simulations. The results from the two analysed cases are presented in the Sections 3.1 and 3.2.

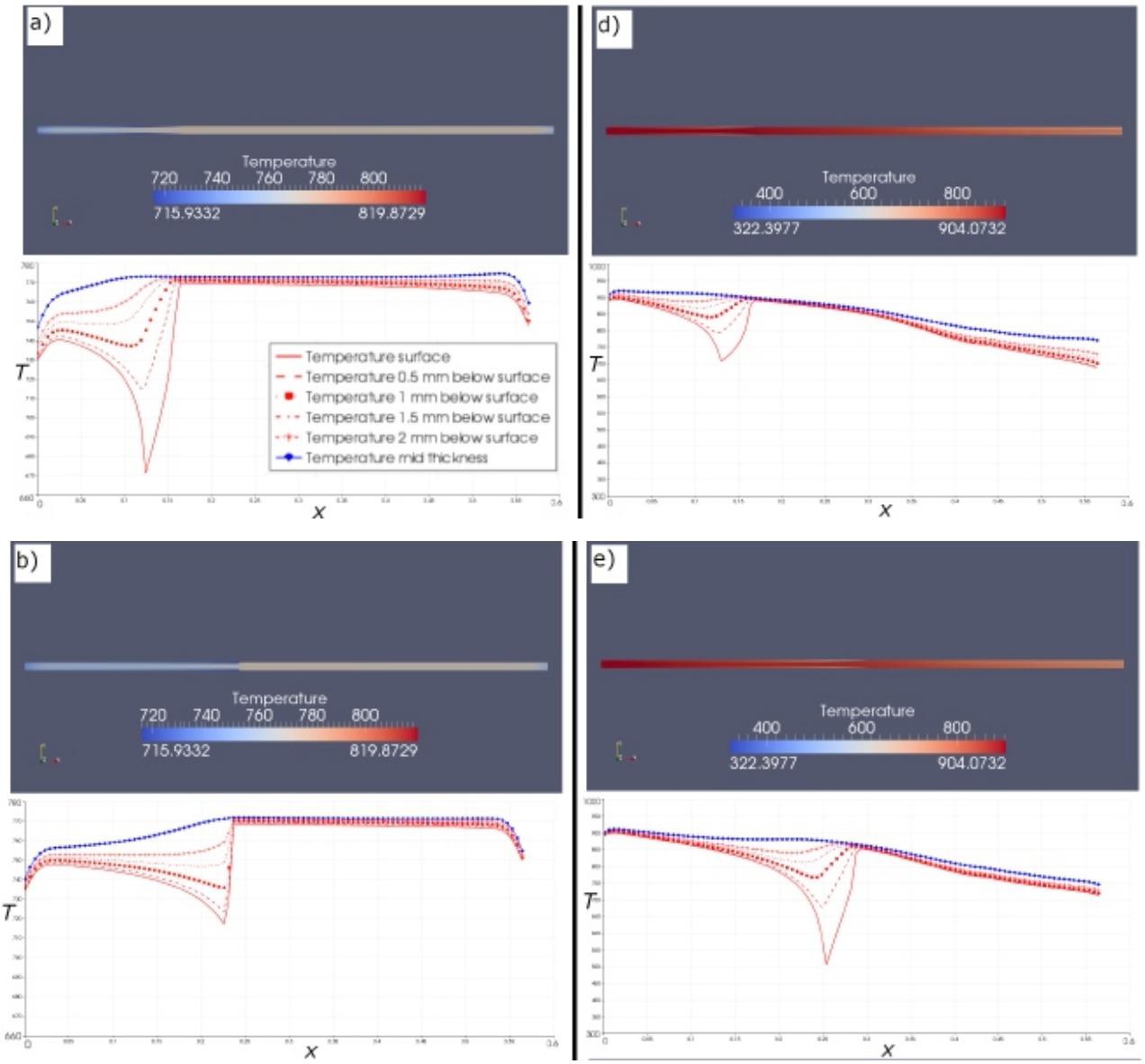

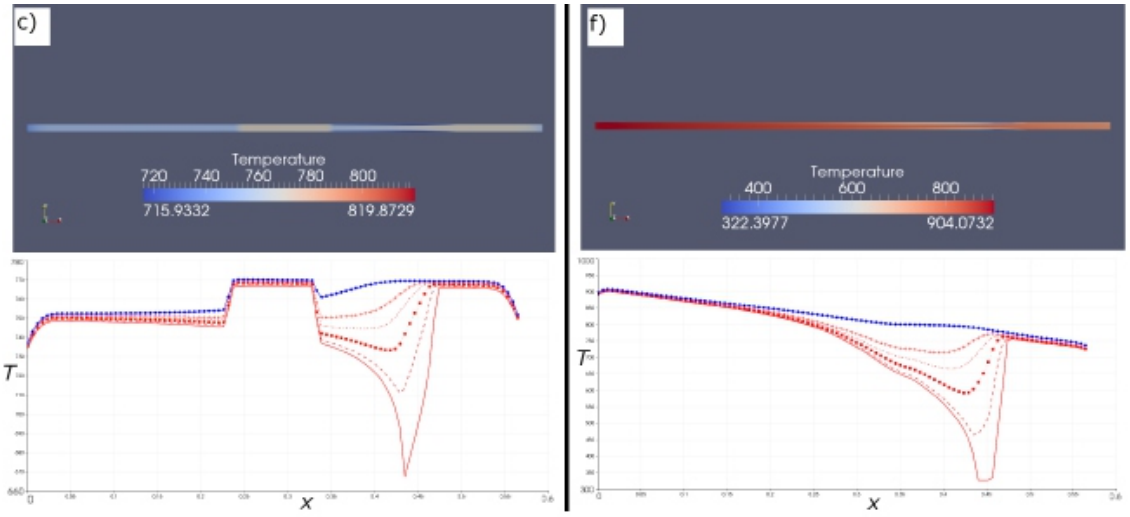

Figure 3. Temperature T (oC) at and near surface (red lines) and in the middle of the plate (blue) along horizontal x direction for simulation snapshots corresponding to the simulated cases (a–c): case 1 (step interruption, LB = 10 cm, z = 0.8 cm), (d–f): case 2 (gradual change, LB = 56.4 cm, z = 0.8 cm). Common legend for all of the figures is shown in (a).

3.1. Simulation case 1: step interruption in cooling

The evolution of temperature and phase fraction distributions along the horizontal x direction in the middle of the plate are shown in Figure 4 for the simulation case study 1. The simulation snapshots are shown for dierent time instants indicated in the figures. This figure depicts the simulation, where the gap length LB = 10 cm and plate thickness z = 0:8 cm.

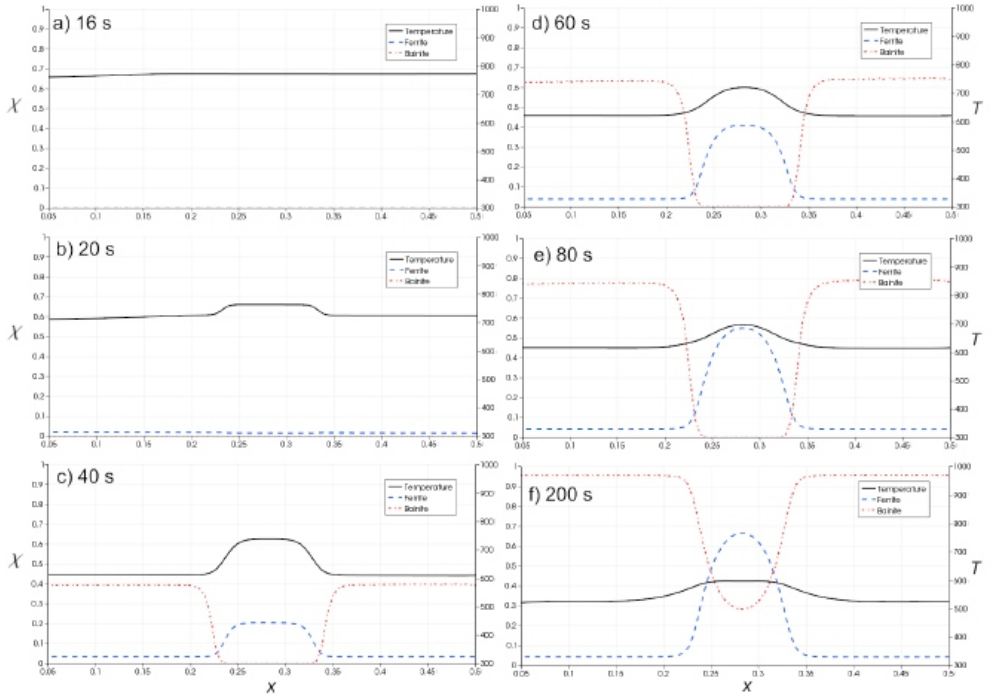

Figure 4. Simulation case 1 (step interruption) with thickness z = 0:8 cm, LB = 10 cm. : transformed fraction, x: x-coordinate (m). T: temperature (oC). Time (s) is indicated in the figures. (a) plate/strip has been uniformly cooled to desired temperature (c–e) ferrite forms at the higher temperature gap region B, bainite forms at the lower temperature regions (A and C) (f) the gap region B contains less bainite.

The result in Figure 4 shows the processes during the simulation: first, (Figure 4a) the whole plate is uniformly cooled to ferrite formation temperateure (780 oC). (Figure 4b) The spray cooling is continued in the regions A and C (depicted in Figure 1), but not in the region B. The region B is cooled by radiation and convection at the surface boundaries in the vertical y-direction and by conduction towards the regions A and C. The spray cooling of the regions A and C is continued until they are in the temperature range for bainite formation. After this water spray cooling is stopped, and the temperature change within the plate occurs due to radiation, convection and conduction (Figure 4c) Once the temperature in the regions A and C is low enough for the bainite formation (600 oC), the bainite forms rapidly in comparison to the slowly forming polygonal ferrite. (Figure 4d,e): polygonal ferrite forms slowly in the region B which is at higher temperature. In the transition region between bainitic and ferritic regions, austenite still stays untransformed for longer time, since this region is in the region where neither ferrite or bainite formation is rapid. (Figure 4f) Once the region B cools to the bainite formation temperature, the remaining austenite transforms to bainite.

The process illustrated in the Figure 4 was similar for the dierent values of LB and z, but for shorter gap lengths, the cooling occurred faster, resulting to lesser amount of ferrite in the region B, confined in thinner region. Thinner plates also cool faster. The resulting microstructures for dierent gap lenghts and for two plate thicknesses (z = 1:2, 0.8 cm) are shown in the Figures 5 and 6 respectively. Using the simulated cooling strategy, it is possible to produce a softer region consisting of polygonal ferrite within a bainitic steel strip or plate. Controlled production of this kind of regions could oer possibility for producing designed tracks within the plate/strip, where mechanical cutting of the steel is easier.

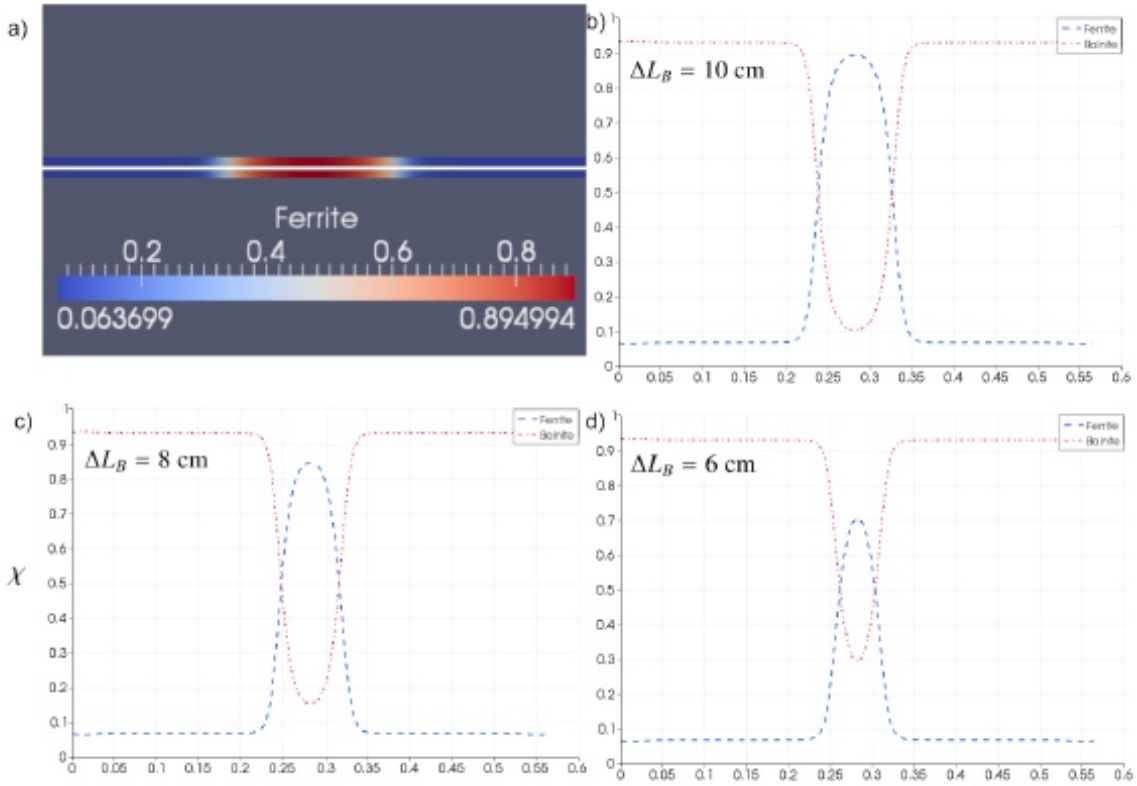

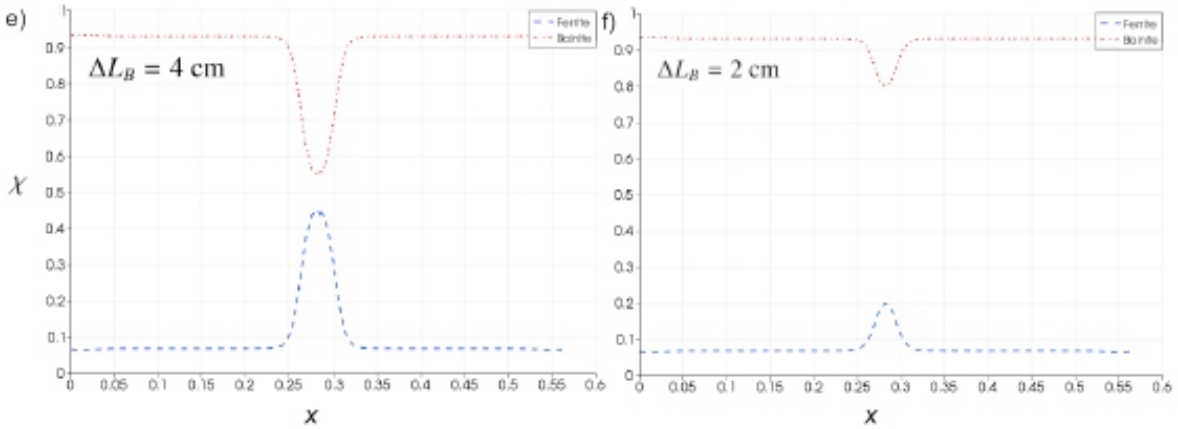

Figure 5. Simulation case 1 (step interruption) with thickness z = 1:2 cm, varying LB. : transformed fraction, x: x-coordinate (m). (a) Phase fractions were plotted along the line in the horizontal x-direction, (b) LB = 10 cm, (c) LB = 8 cm, (d) LB = 6 cm, (e) LB = 4 cm, (f) LB = 2 cm.

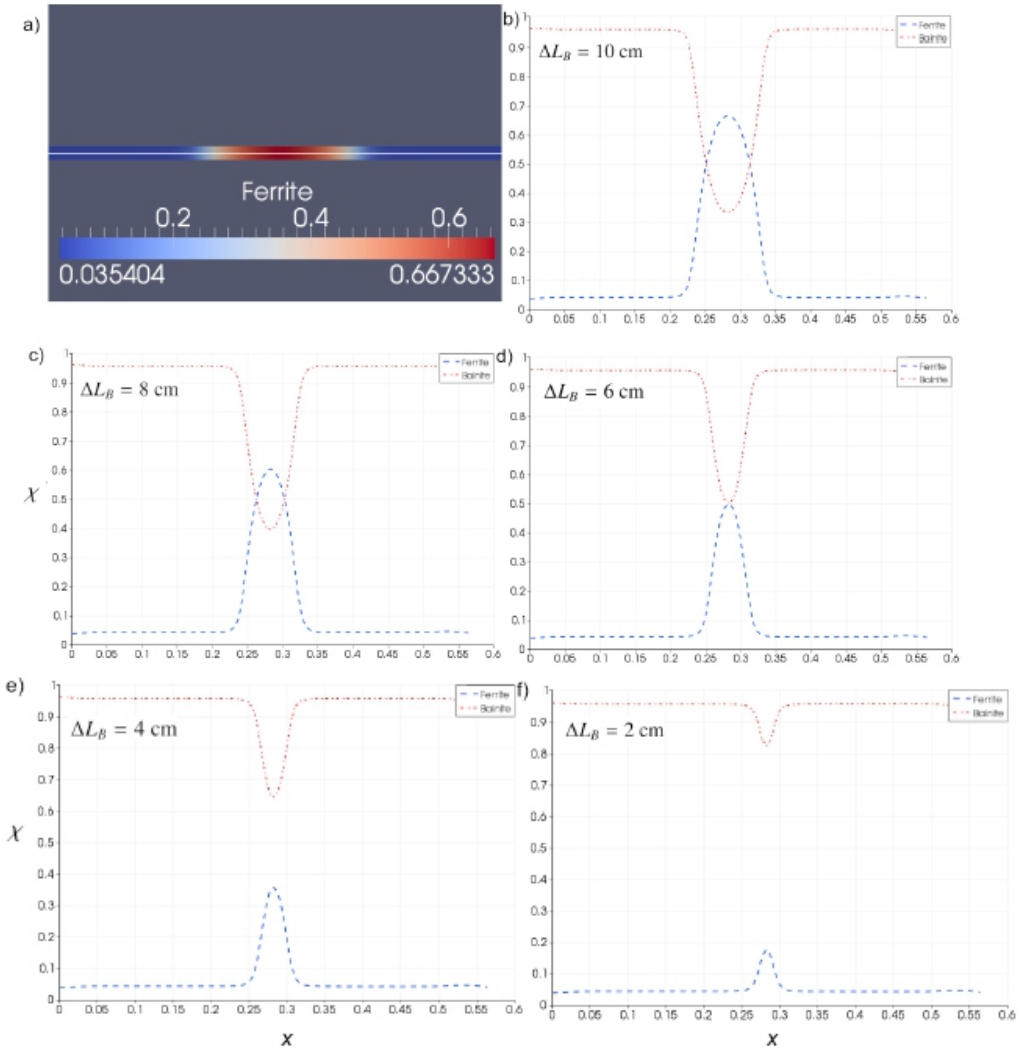

Figure 6. Simulation case 1 (step interruption) with thickness z = 0:8 cm, varying LB. : transformed fraction, x: x-coordinate (m). (a) Phase fractions were plotted along the line in the horizontal x-direction, (b) LB = 10 cm, (c) LB = 8 cm, (d) LB = 6 cm, (e) LB = 4 cm, (f) LB = 2 cm.

3.2. Simulation case 2: gradual change in cooling

The evolution of temperature and phase fraction distributions along the horizontal x direction in the middle of the plate are shown in Figure 7 for the simulation case study 2. For the simulation presented in this figure, the length of the transition region (Figure 2) was equal to the whole plate length in the x-direction, i.e. LB = 0:564 m. (Figure 7a) The right hand side of the plate has been cooled to bainite formation temperature (600 oC), and large fraction of bainite has formed rapidly. The left hand side is at the ferrite formation temperature range (700–780 oC), and austenite has started to transform to polygonal ferrite in this region. (Figure 7b,c) The latent heat release due to rapid bainitic transformation keeps the temperature on the right at almost constant value. On the left, the ferrite forms slowly and the temperature decays slowly due to conduction, radiation and convection. (Figure 7d,e) the left part of the plate is transformed to polygonal ferrie phase and right part is transformed to bainitic phase. At the transition region, large fraction of austenite remains untransformed, since this part is at temperature range between the ferrite and bainite formation temperatures. (Figure 7f) During the slow cooling the remaining austenite is transformed to bainite.

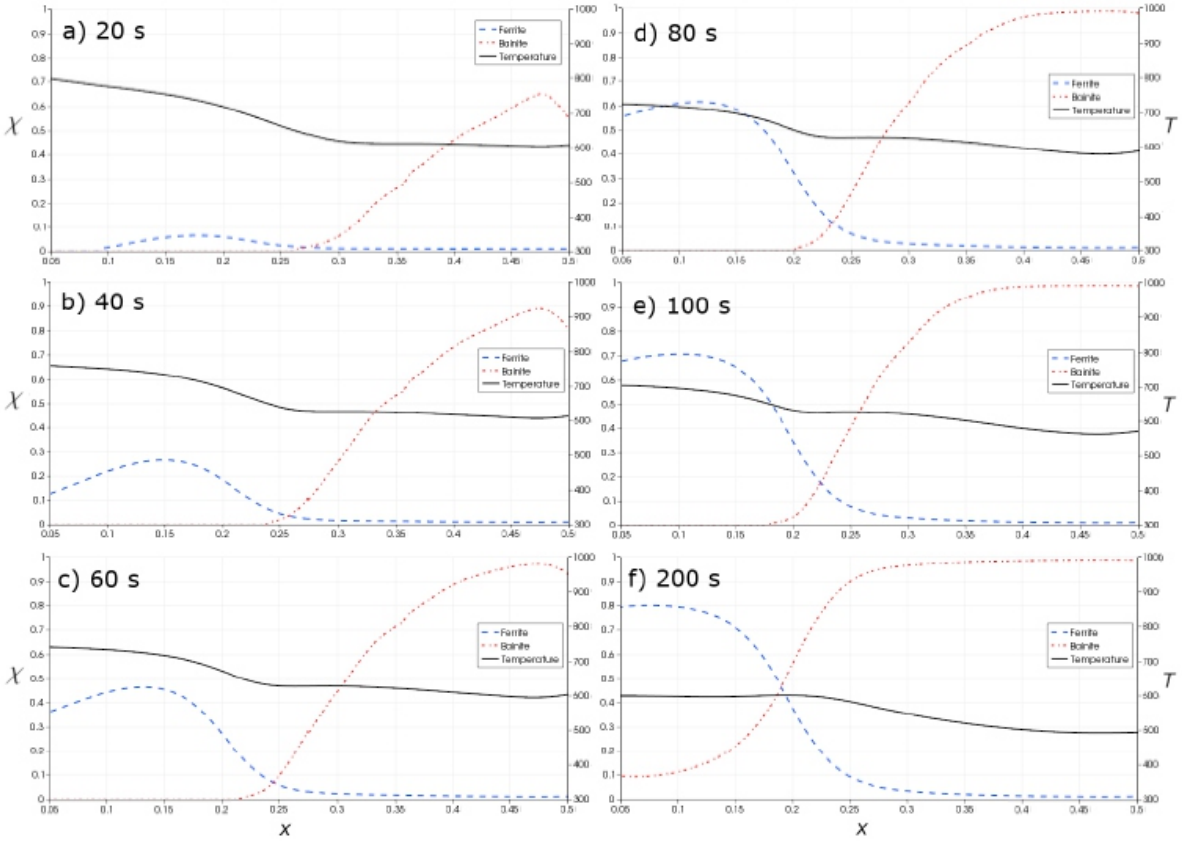

Figure 7. Simulation case 2 (gradual change) with LB = 0:564 m, z = 0:8 cm. : transformed fraction, x: x-coordinate (m), T: temperature (oC). Time (s) is indicated in the figures. (a) bainite has formed on the low temperature region, (b–d) ferrite forms gradually, (e,f) ferrite forms to the final extent and during cooling only small amount of the bainite forms.

The simulations with shorter transition region length, LB, yielded similar results to Figure 7, but with sharper change in temperature and phase fraction distributions, as expected. The resulting phase fractions obtained from these simulations for two plates of dierent thickness (z = 1:2 cm, 0.8 cm) and several transition gap lengths LB are depicted in Figures 8 and 9 respectively. However, when the transition gap length was reduced below 14.1 cm, there was almost no change in the resulting phase distribution.

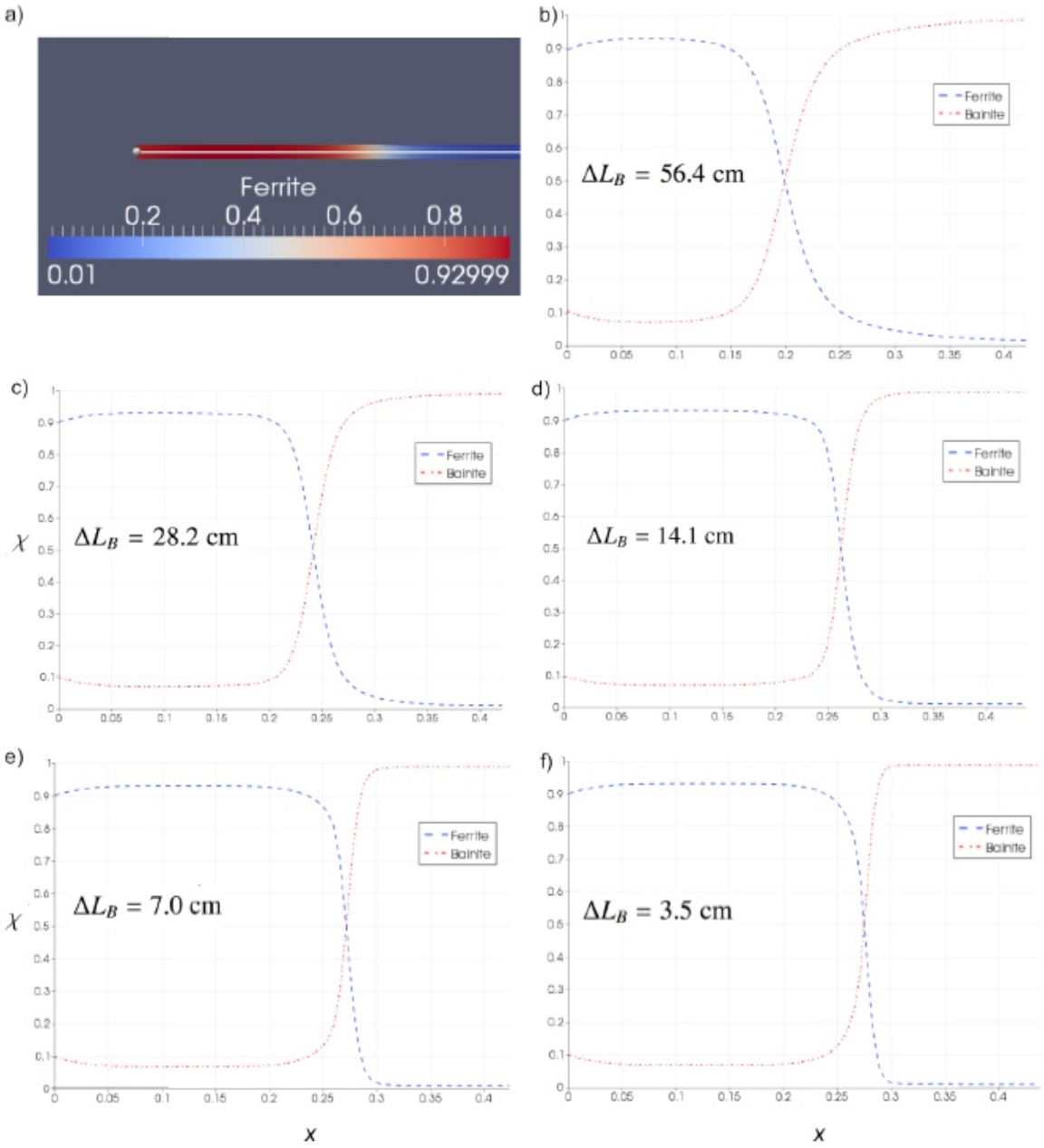

Figure 8. Simulation case 2 (gradual change) with thickness z = 1:2 cm, varying LB. : transformed fraction, x: x-coordinate (m). (a) Phase fractions were plotted along the line in the horizontal x-direction, (b) LB = 56:4 cm (whole plate length), (c) LB = 28:2 cm, (d) LB = 14:1 cm, (e) LB = 7:0 cm, (f) LB = 3:5 cm.

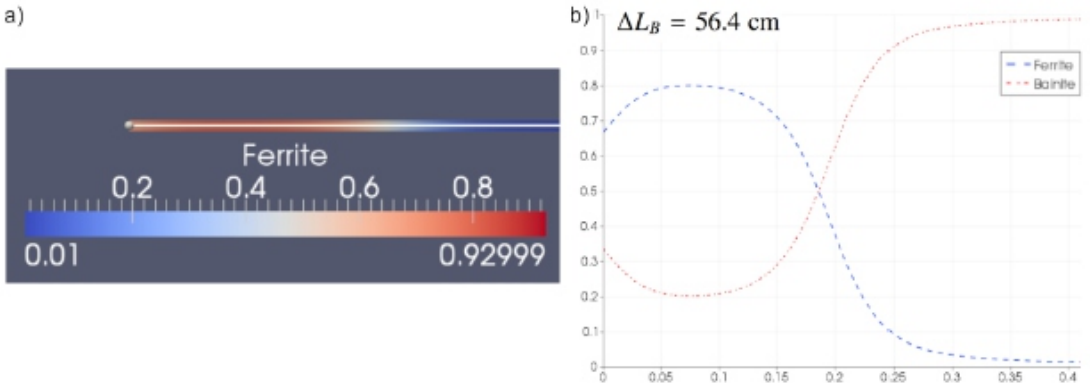

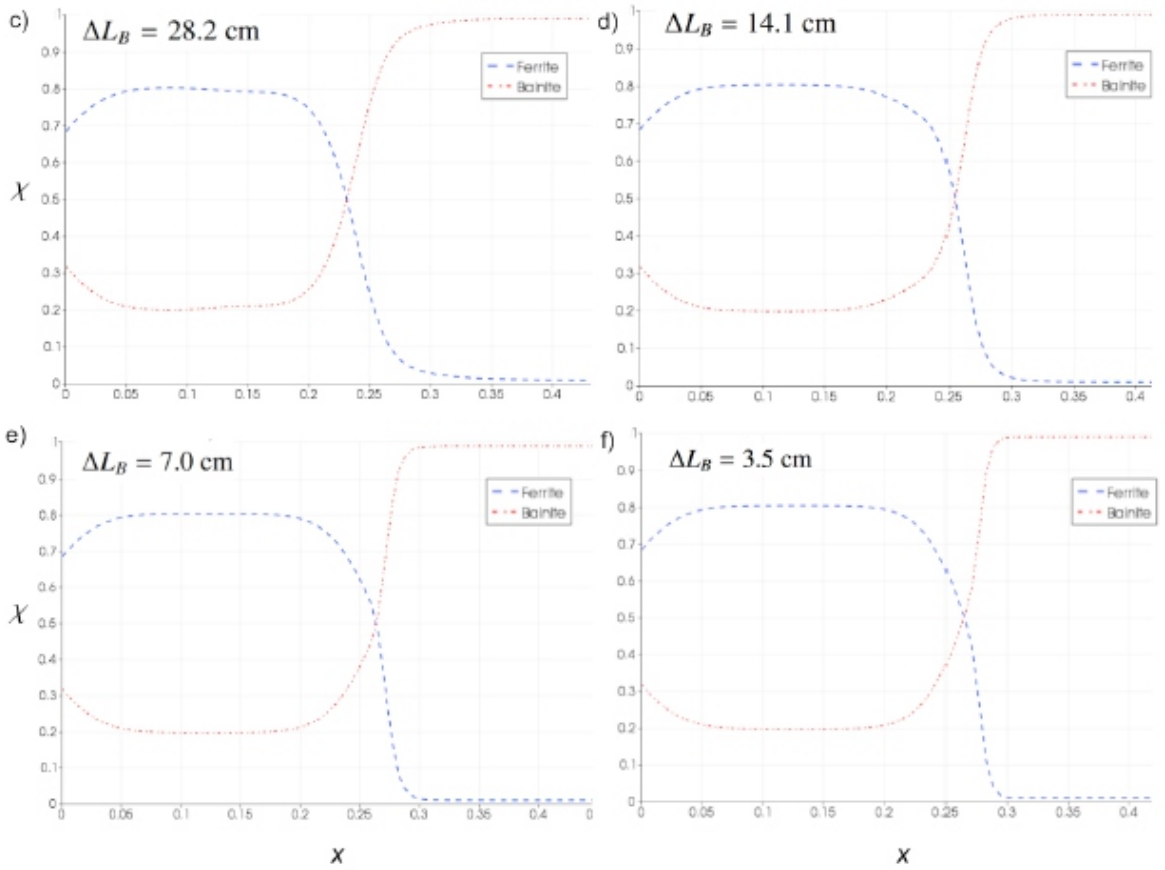

Figure 9. Simulation case 2 (gradual change) with thickness z = 0:8 cm, varying LB. : transformed fraction, x: x-coordinate (m). (a) Phase fractions were plotted along the line in the horizontal x-direction, (b) LB = 56:4 cm (whole plate length), (c) LB = 28:2 cm, (d) LB = 14:1 cm, (e) LB = 7:0 cm, (f) LB = 3:5 cm.

4. CONCLUSIONS AND OUTLOOK

Numerical simulations were used for studying controlled production of alternating polygonal ferrite and bainite regions in a steel plate or strip by means of applying dierential water spray cooling at dierent positions of the plate/strip. In the simulations, dierent regions were cooled to dierent temperatures, after which the water spray cooling was stopped, so that polygonal ferrite formed in the higher temperature region and bainite formed in lower temperature region. The results show that dierential microstructures can be controlledly created by the dierential cooling procedure, but the resulting ferrite/bainite regions in this case should not be expected to be very fine. The simulation results show that transition region between the ferrite and bainite could be controlled to be in the range of 5–15 cm for the applied cooling strategy. Bainite is seen to form rapidly in the low temperature region, and polygonal ferrite more slowly in the high temperature region. In the transition zone between the bainite and ferrite regions, austenite stayed untransformed for longer time. If mechanical forming is applied to the transition region at the time interval when it is still austenitic, it could be easy to form this region in relatively low temperature. The dierential cooling strategy could be applied to controlledly create softer ferrite regions in a bainite plate or strip where mechanical cutting would be easier. The polygonal ferrite zones in otherwise bainitic steel could also be applied in a setting where it is desirable to create easily deformable regions at desired positions. In future, the results obtained from the numerical simulations can serve as basis for conducting laboratory scale trials for precise determination of cooling parameters that are needed for accurately producing the alternating ferrite/bainite regions. Future studies could also consider combined heating, cooling, and deformation, as well as extending the simulations for dierent cooling strategies.

ACKNOWLEDGMENTS

The funding of this research activity under the auspices of Genome of Steel (Profi3) project through grant #311934 by the Academy of Finland is gratefully acknowledged.

Conflict of interest

Author declares no conflict of interest.

REFERENCES

1. *Malinov LS (1997) Obtaining a macroscopically nonuniform regular structure in steel by methods of dierential treatment. Met Sci Heat Treat+ 39: 139–143.*
2. *Estrin Y, Beygelzimer Y, Kulagin R (2019) Design of architectured materials based on mechanically driven structural and compositional patterning. Adv Eng Mater 21: 1900487.*
3. *Bao L, Nie Q, Wang B, et al. (2019) Development of hot stamping technology for high strength steel parts with tailored properties. IOP Conference Series: Materials Science and Engineering 538: 012016.*
4. *Bok HH, Lee MG, Pavlina EJ, et al. (2011) Comparative study of the prediction of microstructure and mechanical properties for a hot-stamped B-pillar reinforcing part. Int J Mech Sci 53: 744–752.*
5. *Kushnarev AV, Smirnov LA, Kirichkov AA, et al. (2020) Development of an innovative digital cooling technology (dierential heat treatment) for Evraz Ntmk rails. Steel Transl 50: 415–419.*
6. *Gale WF, Totemeier TC (2004) Heat treatment, Smithells Metals Reference Book, 8 Eds., Oxford: Butterworth-Heinemann, 29-1–29-83.*
7. *Pohjonen A, Somani M, Porter D (2018) Modelling of austenite transformation along arbitrary cooling paths. Comp Mater Sci 150: 244–251.*
8. *Pohjonen A, Kaijalainen A, Somani M, et al. (2017) Analysis of bainite onset during cooling following prior deformation at dierent temperatures. Comput Methods Mater Sci 17: 30–35.*
9. *Pohjonen A, Kaijalainen A, Mouruj¨arvi J, et al. (2018) Computer simulations of austenite decomposition of hot formed steels during cooling. Procedia Manuf 15: 1864–1871.*
10. *Pohjonen A, Paananen J, Mouruj¨arvi J, et al. (2018) Computer simulations of austenite decomposition of microalloyed 700 MPa steel during cooling. AIP Conference Proceedings 1960: 090010.*
11. *Ilmola J, Pohjonen A, Sepp¨al¨a O, et al. (2018) Coupled multiscale and multiphysical analysis of hot steel strip mill and microstructure formation during water cooling. Procedia Manuf 15: 65–71.*
12. *Uusikallio S, Koskenniska S, Ilmola J, et al. (2020) Determination of eective heat transfer coe-cient for water spray cooling of steel. Procedia Manuf 50: 488–491.*
13. *Ilmola J, Pohjonen A, Koskenniska S, et al. (2021) Coupled heat transfer and phase transformations of dual-phase steel in coil cooling. Mater Today Commun 26: 101973.*
14. *Javaheri V, Pohjonen A, Asperheim JI, et al. (2019) Physically based modeling, characterization and design of an induction hardening process for a new slurry pipeline steel. Mater Design 182: 108047.*
15. *Pohjonen A, Kaikkonen P, Sepp¨al¨a O, et al. (2021) Numerical and experimental study on thermomechanical processing of medium-carbon steels at low temperatures for achieving ultrafinestructured bainite. Materialia 18: 101150.*
16. *Garc´ıa Mateo C, Eres-Castellanos A, Garc´ıa Caballero F, et al. (2020) Towards industrial applicability of (medium C) nanostructured bainitic steels (TIANOBAIN). Available from: https://digital.csic.es/handle/10 261/217266.*
17. *Ilmola J, Pohjonen A, Sepp¨al¨a O, et al. (2020) The eect of internal contact pressure on thermal contact conductance during coil cooling. Procedia Manuf 50: 418–424.*
18. *Donnay B, Herman JC, Leroy V, et al. (1996) Microstructure evolution of C–Mn steels in the hotdeformation process: the stripcam model. 2nd International Conference on Modelling of Metal Rolling Processes, 23–35.*
19. *Scheil E (1935) Start time of austenite transformation. Archiv f¨ur das Eisenh¨uttenwesen 12: 565– 567 (In German). Available from: https://doi.org/10.1002/srin.193500186.*
20. *Kirkaldy JS (1983) Prediction of microstructure and hardenability in low alloy steels. Proceedings of the International Conference on Phase Transformation in Ferrous Alloys, 125–148.*
21. *Steven W (1956) The temperature of formation of martensite and bainite in low alloy steels, some eects of chemical composition. J Iron Steel Institute 183: 349–359.*
22. *Martin DC (2011) Selected heat conduction problems in thermomechanical treatment of steel, Oulu: University of Oulu.*
23. *Browne KM (1998) Modeling the thermophysical properties of iron and steels. Proc Mater 2: 433–438.*

·ISSN : 2372-0484

Assessing the Mechanical Properties of Molecular Materials from Atomic Simulation

Julian Konrad and Dirk Zahn*
Lehrstuhl für Theoretische Chemie/Computer Chemie Centrum, Friedrich-Alexander Universität Erlangen-Nürnberg, Nägelsbachstraße 25, 91052 Erlangen, Germany
* Correspondence: Email: dirk.zahn@fau.de.

ABSTRACT

We review approaches to deriving mechanical properties from atomic simulations with a special emphasis on temperature-dependent characterization of polymer materials. The complex molecular network of such materials implies only partial, rather local ordering stemming from the entanglement of molecular moieties or covalent bonding of network nodes, whereas the polymer strands between the nodes may undergo nm-scale reorganization during thermal fluctuations. This not only leads to a strong temperature-dependence of the elastic moduli, but also gives rise to viscoelastic behavior that complicates characterization from molecular dynamics simulations. Indeed, tensile-testing approaches need rigorous evaluation of strain-rate dependences, provoking significant computational demands. Likewise, the use of fluctuations observed from unbiased constanttemperature, constant-pressure molecular dynamics simulation is not straight-forward. However, we suggest pre-processing from Fourier-filtering prior to taking Boltzmann-statistics to discriminate elastic-type vibrations of the simulation models for suitable application of linear-response theory.

Keywords: molecular materials; polymers; mechanical properties; molecular dynamics simulations

1. INTRODUCTION

For crystalline materials, the prediction of elastic properties became a routine task that usually relies on energy minimization to get equilibrium structures, followed by (numerical) assessment of the second derivatives of energy upon simulation cell deformation [1–3]. While this approach leads to elastic moduli of quite reasonable accuracy when characterizing metals and ionic crystals, molecular materials—in particular if they are not crystalline—show strong, and often non-linear, temperature-dependence of mechanical properties [4,5]. This opposes to the zero Kelvin approximation inherent to structures derived from energy minimization. Instead, Monte-Carlo or molecular dynamics simulation methods are required to account for temperature effects to atomistic models [6,7].

A very intuitive molecular dynamics simulation approach for the assessment of mechanical properties is to essentially mimic the corresponding experiment by inducing a deformation of the simulation model and sampling the restoring forces. On this basis, each mode of deformation (tensile loading, shear, bulk compression) can be probed, and the elastic moduli attributed to the curvature of the respective stress-strain diagram. On the other hand, a very elegant route was originally suggested more than 50 years ago—by attributing the spontaneous fluctuations of a sample volume to a linear response model [8,9]. This allows for simultaneous sampling of all elastic moduli from constanttemperature, constant-pressure molecular dynamics or Monte-Carlo simulations.

Both of these approaches call for careful implementation when applied to complex molecular materials. In what follows, we will review the fundamental simulation protocols and outline strategies for error

control. To demonstrate the assessment of temperature-dependent elastic moduli, we selectively picked a recent molecular dynamics simulation model that mimics an epoxy polymer [10]. This not only reflects a particularly prominent class of molecular materials, but also a rather rigorous benchmark for system complexity. Indeed, freshly cured epoxy resins are noncrystalline (and desired to remain so within most technical applications), like most polymer materials, and show little ordering beyond the range of 1–2 nm. On the other hand, there is significant local ordering at the <1 nm scale stemming from the well-defined chemistry of binding the monomeric units into polymer strands. These strands may occur as in principle stand-alone fibers which are however twisted and entangled with each other [11]. More robust polymer materials, such as epoxy resins, are however comprised of covalently bonded networks [12,13]. As a consequence, the entire sample of the material may be considered as a single molecule. The mechanical properties dramatically depend on the degree of cross-linking which, in state-of-the-art industrial application, reaches almost 100% of the available binding sites [14]. In our benchmark model, we achieved 98% crosslinking of the base monomer (bisphenol F diglycidyl ether, BFDGE) and the linker species (4,6- diethyl-2-methylbenzene-1,3-diamine, DETDA) [10,15]. This could be achieved from systematically exploring the curing process from combined quantum/molecular mechanical treatment of linking reactions and extended analyses of overall network relaxation upon increasing degree of crosslinking [10,15].

Despite this high level of crosslinking, epoxy resins are best described as molecular networks with a clear distinction between strands and nodes [12,13]. The nodes that (covalently) connect 2-4 strands are separated by 1–2 nm, whereas the strands comprise of molecular moieties which atoms are bonded at ~0.15 nm distance. This structural diversity has important implications on the mechanical properties. While damaging and fracture is related to the cleavage of crosslinks or, much less frequently, rupture of strands, even the network of intact nodes gives rise to non-linear stressstrain characteristics [10]. The 1–2 nm sized strands are comparably flexible and may rotate, bend, or twist in response to mechanical load—but also by thermal fluctuations. For this reason, we find strong changes of the mechanical properties as functions of temperature. For the same reason, we however also find strong dependence of the stress-strain diagrams as functions of the strain rates used to deform the material [4,5].

2. ELASTIC MODULI FROM ENERGY MINIMIZATION

The most frequently used approach to computing elastic moduli from atomic simulations is based on non-dynamic calculations [16,17]. Starting points are relaxed structures resulting from

energy minimization. These are then subjected to small deformations $\bar{\varepsilon}$ (e.g. by linearly shifting atom positions according to ±1% uniaxial deformation $\epsilon_{11}, \epsilon_{22}$ and ϵ_{33} or ±1° shear in $\epsilon_{23}, \epsilon_{13}$ and ϵ_{12}, respectively) and the corresponding stress $\bar{\sigma}$ is related to (using Voigt notation) [18]:

$$\bar{\sigma} = \begin{pmatrix} \sigma_{11} \\ \sigma_{22} \\ \sigma_{33} \\ \\ \sigma_{23} \\ \sigma_{13} \\ \sigma_{12} \end{pmatrix} = \begin{pmatrix} c_{11} & \cdots & c_{61} \\ \vdots & \ddots & \vdots \\ c_{16} & \cdots & c_{66} \end{pmatrix} \begin{pmatrix} \varepsilon_{11} \\ \varepsilon_{22} \\ \varepsilon_{33} \\ \\ \varepsilon_{23} \\ \varepsilon_{13} \\ \varepsilon_{12} \end{pmatrix} = \bar{\bar{c}} \cdot \bar{\varepsilon} \qquad (1)$$

Despite the inherent zero Kelvin approximation, this is the method of choice for crystalline materials, provided that the melting point is far above the technically relevant temperature (usually 300 K) for which the prediction of elastic properties shall apply.

For such systems, typical calculations focus on units cells subjected to periodic boundary conditions —which implies only few explicit atoms and hence allows for high-accuracy quantum mechanical description. Using this single crystal approximation, symmetry-equivalent elastic moduli c_{ij} may be ruled out and the independent deformation modes may be either probed individually or concerted fitting of $\bar{\bar{C}}$ according to Eq 1 is performed [19]. Along this line, tensile deformations and shear are typically implemented as <5% deformation and <10° shear of the unit cell vectors, whereas the explicit atoms therein are allowed to relax according to energy minimization as a function of $\bar{\varepsilon}$.

For simple crystals like pure metals, structure relaxation typically leads to linear atomic displacements according to $\bar{\varepsilon}$. however for more complex systems such as intermetallic phases, ionic and molecular crystals the atomic displacements significantly depend on the interplay of overall unit cell deformation and the heterogeneity of local interactions. This is particularly evident for molecular crystals which feature strong covalent bonds within the molecules and much weaker interactions (Hbonds, π-stacking, van-der-Waals) between the molecules.

3. TEMPERATURE-DEPENDENT STRESS-STRAIN PROFILES

Inhomogeneous atomic displacements upon crystal deformation are also crucial for rationalizing the temperature-dependence of the elastic properties. The reorganization of local atomic moieties may involve significant displacements normal to the overall mode of deformation $\bar{\varepsilon}$ crystal. Examples are zig-zag shifts leading to the puckering of layers or rotation/slipping of molecular fragments such as polymer strands [5]. Subject to the strength of local interactions, these displacements may occur spontaneously during deformation—or involve the crossing of energy barriers ΔE before locking into a favorable configuration. While the former situation is well described by energy minimization approaches, barrier crossing calls for explicit account of temperature T and thus requires Monte-Carlo or molecular dynamics (MD) simulations. Among these two techniques, MD simulations are widely preferred for rationalizing complex materials because of its direct insights into reorganization dynamics.

In MD simulations of material deformation, the likeliness of reorganization events triggered by the crossing an energy barrier ΔE is related to $p = p_0 e^{-\frac{\Delta E}{k_B T}}$ with k_B being the Boltzmann constant and p_0 being a kinetic pre-factor which depends on the strain rate applied to induce deformation. Atomic displacements confined by only small barriers, say $\Delta E < k_B T$, typically occur on time scales that are much lower than the time scales at which deformation experiments are performed. Such small-barrier reorganization hence appear as elastic modes unless the deformation rate reaches the speed of sound. On the other hand, local reorganization events that require the crossing of large barriers happen only rarely. As a consequence, the material will undergo only a fraction of all possible relaxation moves. Each reorganization event lowers the stress and the overall restoring force response to a given deformation will thus depend on the available relaxation time.

As a simplified picture, such pseudo-elastic behavior may be considered as a first order kinetics assuming at least two types of local deformations, (a) linearly strained regions with comparably large potential energy and (b) domains in which atomic displacements normal to the applied deformation mode helped to lower energy. The overall stress σ will then result from a combination of type (a) and type (b) contributions, subject to the corresponding occurrences h_a and $h_b = 1 - h_a$, respectively:

$$\sigma = h_a \cdot \sigma_a + (1 - h_a) \cdot \sigma_b \quad with \; h_a(t) = 1 \cdot e^{-t/\tau_{relaxation}} \qquad (2)$$

where the characteristic relaxation time scale $\tau_{relaxation}$ is the inverse of the a→b transition rate $r_{a\to b}(T)$—which is a function of temperature as given by the Arrhenius law [20].

$$\tau_{relaxation} = {}^{1}/_{r_{a\to b}} = const \cdot e^{+{}^{\Delta E}/_{k_B T}} \quad (3)$$

To illustrate the importance of local reorganization events, in Figure 1 we depicted snapshots from an epoxy polymer model taken from [10]. In this 100 ns MD simulation run we did not apply external loading to the model system, but only used an (anisotropic) barostat-thermostat algorithm to inspect thermal fluctuations at 1 atm and 300 K, respectively. Comparing the two snapshots, we find (i) a quite homogeneous distribution of atomic displacements in the ball-park of 0.1–0.2 nm and (ii) a strongly inhomogeneous pattern of atomic displacements up to 1 nm. Here, (i) reflects typical vibrations of atoms with respect to their lattice site. In contrast to this, the much rarer, but larger displacements of type (ii) illustrate local reorganization of polymer strands. For the latter, the system must overcome energy barriers stemming from the dissociation of strand-strand contacts and the sliding of adjacent molecular moieties [5].

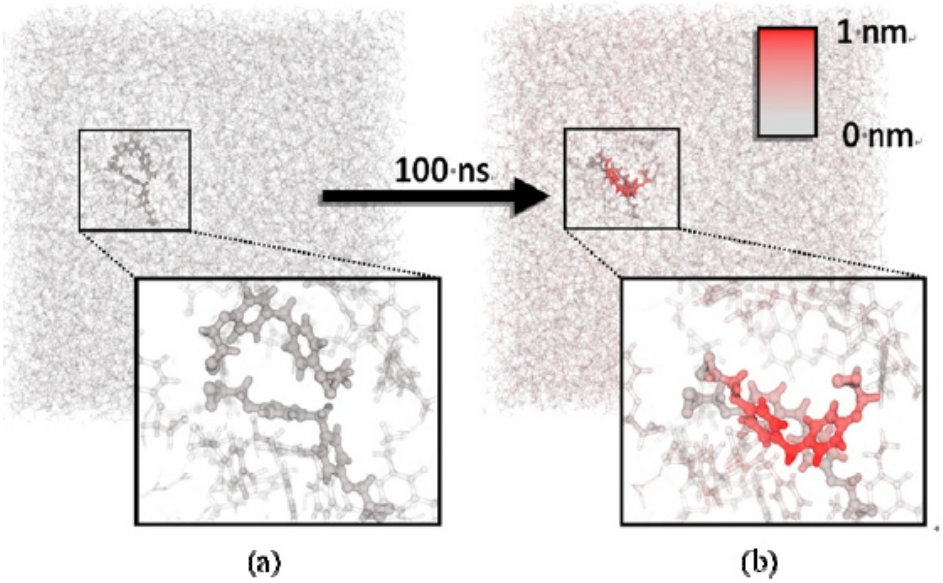

Figure 1. (a): Snapshot from a 98%-cured epoxy polymer model as adopted from [10]. (b): same system after 100 ns MD simulation at 1 atm and 300 K. The scale bar indicates 1 nm. The extend of atomic displacements is highlighted by a color code to discriminate (i) 0.1–0.2 nm scale fluctuations (grey) that are homogeneously distributed in the polymer model—and actually occur on much faster time scales <10 ns. On the other hand, (ii) we identified 0.5–1 nm scale atomic displacements that stem from local rearrangement of polymer strands with respect to each other. The close-ups highlight the flipping of a polymer strand (red) with a maximum atomic displacement of about 1 nm. This kind of reorganization events (ii) involves the crossing of energy barriers and thus occurs on much slower time scales as compared to the 0.1–0.2 nm vibrations (i). Note that the extent of chain flexibility strongly depends on the type of polymer and increases with decreasing degree of cross-linking.

In absence of external loading, such local rearrangement events occur without orientation preference and thus lead to fluctuations of the simulation cell (which we will inspect more closely in the next section). However, in a model system which experiences deformation, the rotation of polymer strands

within the twisted network gets biased in favor of stress reduction. This leads to an exponential decay of σ(t) as predicted by Eq 1—and monitored within MD simulations at constant strain as illustrated in Figure 2.

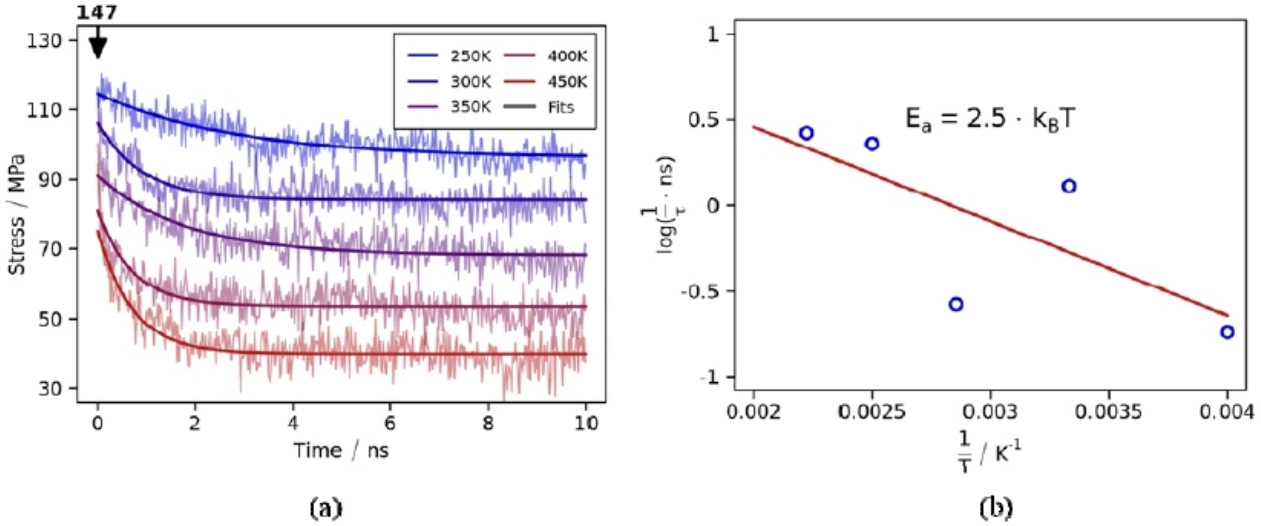

Figure 2. (a): tensile stress relaxation as a function of time as observed in deform-andhold MD simulations. Using the same starting point, relaxation at constant elongation of the simulation model is explored at different temperatures and subjected to exponential fits. On this basis, the cascade of relaxation moves is approximated by first-order kinetics triggered by an average reorganization barrier ΔE .(b): the Arrhenius plot of therelaxation rate according to Eq 3 leads to $\Delta E = 2.5\ (\pm 0.7)\ k_B \cdot 300\ \mathrm{K}$. simulation model uses a reactive force-field that diminishes barriers from bond formation/cleavage. The relaxation kinetics reported here hence refer to the sliding and twisting of polymer strands, exclusively (see also Figure 1).

The most widely spread approach to assessing elastic moduli at non-zero temperature is to perform MD simulations combined with induced deformation of the simulation cell. In analogy to the experiment, tensile testing or shearing within MD runs may be implemented by application of external stress with is ramped up linearly as a function of time. The fundamental difference here is however the large gap between experimental time scales and the ns to μs time scales available to MD simulation using force-fields of atomic resolution. This is even worse for ab-initio MD with offer electronic resolution, but barely reach the ns time scale. To get meaningful stress-strain diagrams from molecular simulation, the common route is to apply strain to the simulation cell and sample the resulting stress.

Along this line, the shape of the simulation cell is controlled externally, typically whilst maintain the overall volume of the system. In ref. [10], we used an unbiased approach for this purpose, namely via implementation of axial deformation at constant rate using $\epsilon_{11} = 1 + \dot{\epsilon} \cdot (t - t_0)$ and fixing the length of the corresponding cell vector $\vec{a}$ to $a = \epsilon_{11} \cdot a(t_0)$, whereas a 2-dimensional barostat algorithm allows relaxation in the perpendicular directions [10]. Stress-strain profiles collected in this manner will nevertheless depend on the applied rates and convergence checks from comparing a series of deformation runs of different strain rates are advised. For simple single crystalline systems, this often suffices to obtain reasonable agreement with the experiment. In turn, molecular materials—like the polymer model used as a demonstrator system in Figures 1 and 2—are however quite likely to display very slow relaxation modes [5]. Indeed, tensile testing of epoxy polymer shows strain rate dependence even in experiments performed on the time scale of up to 105 s—which exceeds the scope of MD simulations by more than 10 orders of magnitude [21].

To model such systems in a more realistic manner, MD simulations need to be redirected to mimic quasi-static conditions. For this, a series of deformed simulation cells may initially be prepared from taking snapshots from constant strain rate runs. Next, the corresponding models are inspected in parallel MD runs at constant strain. This allows investing up to μs of relaxation time to an individual data point of the stress-strain diagram. The underlying relaxation process can be followed by monitoring stress as a function of time—as illustrated in Figure 2. While the overall relaxation might require even longer time scales, already 10 ns scale runs may offer insights into partial relaxation which suffices for exponential fits of the decay in σ(t) as denoted in Eq 2. Using the asymptotic stress $\sigma(t \to \infty)$rom this procedure for comparison to the experiment, we indeed found quite convincing agreement of the elastic part of the stress-strain diagrams and even the ultimate stress of the epoxy system before fracture [10,21].

4. STRESS RESPONSE FROM TEMPERATURE-DEPENDENT FLUCTUATIONS

A very elegant way of assessing elastic properties of materials is to take use of spontaneous fluctuations from the equilibrium geometry [8,22]. For a given set of temperature and pressure conditions, we can describe the equilibrium cell of a simulation model by the length of the box edges

a_0, b_0, c_0 and the angles between the cell vectors $\alpha_0, \beta_0, \gamma_0$, respectively, and expand a Taylor series for describing the energy cost ΔE of deviations $\Delta a, \Delta\alpha, \Delta b, \Delta\beta, \Delta c$ and $\Delta\gamma$, respectively. For the example of bulk compression ΔV, we thus get:

$$E(\Delta V) = E_0 + \left.\frac{\partial E}{\partial V}\right|_{V_0} \cdot \Delta V + \frac{1}{2}\left.\frac{\partial^2 E}{\partial V^2}\right|_{V_0} \cdot (\Delta V)^2 + \frac{1}{6}\left.\frac{\partial^3 E}{\partial V^3}\right|_{V_0} \cdot (\Delta V)^3 + \frac{1}{24}\left.\frac{\partial^4 E}{\partial V^4}\right|_{V_0} \cdot (\Delta V)^4 + .. \quad (4)$$

whereas full analogous expansions $\Delta E(\Delta a)$, $\Delta E(\Delta\alpha)$ etc. are obtained for tensile and shear deformation modes, respectively. Note that all derivatives are taken with respect to the equilibrium geometry which causes the first derivatives in Eq 4 to vanish.

Per definition, elastic deformation implies a linear response of the restoring stress as a function of strain, namely:

$$p = -\frac{\Delta E}{\Delta V} = -K \cdot \Delta V \quad (5)$$

with

$$K = \begin{cases} \left.\frac{\partial^2 E}{\partial V^2}\right|_{V_0} & (ideal\ elastic) \\ \left.\frac{\partial^2 E}{\partial V^2}\right|_{V_0} + \frac{1}{2}\left.\frac{\partial^3 E}{\partial V^3}\right|_{V_0} \cdot (\Delta V) + \frac{1}{6}\left.\frac{\partial^4 E}{\partial V^4}\right|_{V_0} \cdot (\Delta V)^2 + .. & (non-linear\ elastic) \end{cases} \quad (6)$$

In absence of external loading, the deviations of simulation cell volume $\Delta V = V(t) - V_0$ (and likewise $\Delta a, \Delta\alpha$ etc.) only stem from thermal fluctuations and are hence as small as actually possible at non-zero temperature. As a consequence, the elastic behavior is typically well described by the idealized linear formulation of Eq 5 with $K = \left.\frac{\partial^2 E}{\partial V^2}\right|_{V_0}$ being a constant. While the implementation of so-called non-linear elastic moduli is straight-forward [23], in what follows we focus on the ideal elastic case.

After sufficient relaxation of a material under investigation to ensure thermodynamic equilibrium by means of constant-temperature, constant-pressure MD simulation, the fluctuations of the simulation cell

are simultaneously obtained by monitoring the cell vectors as functions of time [22]. Taking use of Boltzmann statistics, the occurrence profile h of spontaneously observed deformations related to a given mode can directly be related to the corresponding energy profile. For the example of volume fluctuations $\Delta V = V(t) - V_0$ this implies

$$h(\Delta V) = h_0 \cdot e^{\frac{E(\Delta V)}{k_B T}} = h_0 \cdot e^{\frac{E_0 + \frac{1}{2}K(\Delta V)^2}{k_B T}} = const \cdot e^{\frac{(\Delta V)^2}{2d_{\Delta V}}} \quad (7)$$

where the right part of Eq 7 refers to the fitting of a Gaussian distribution to the occurrence statistics of $\Delta V = V(t) - \langle V \rangle_t$ with $V_0 = \langle V \rangle_t$ and $d_V = d_{\Delta V}$ being the standard deviation of $\Delta V(t)$. Likewise, Gaussian fits may be performed for the occurrence profiles of cell vector dimensions, e.g. $\Delta a(t)$ or the cell angles, e.g. $\Delta \alpha(t)$ to provide the corresponding standard deviations d_a and d_α, respectively. Thus, the analyses of a single MD run at thermodynamic equilibrium offers the entire set of elastic constants:

$$K = \frac{k_B T}{(d_V)^2} \cdot \langle V \rangle_t \qquad \text{(bulk modulus)}$$

$$Y_a = \frac{k_B T}{(d_a)^2} \cdot \frac{(\langle a \rangle_t)^2}{\langle V \rangle_t} \qquad \text{(Youngs modulus in } \boldsymbol{a} \text{ direction)} \quad (8)$$

$$G_{ab} = \frac{k_B T}{(d_\gamma)^2} \cdot \frac{1}{\langle V \rangle_t} \qquad (\boldsymbol{ab} \text{ shear modulus})$$

Despite the elegant simplicity of this approach, practical application to characterizing complex materials is complicated by the overlapping of elastic modes with other processes such as viscoelastic deformation. Indeed, for molecular materials models subjected to direct sampling of occurrence statistics we typically find the elastic moduli from Eq 8 to be underestimated. This is nicely illustrated by our beforehand discussed benchmark system modelling an epoxy polymer [10].

To assess the Youngs modulus for deformations along a, we find a superposition of elastic and visco-elastic fluctuations than can formally be written as:

$$a(t) = a_0 + \Delta a^{elastic}(t) + \Delta a^{visco}(t) \quad (9)$$

As a consequence, the standard deviation taken from the overall occurrence statistics d_a is equal or larger than that of the purely elastic deformation models, Figure 3 clearly indicates $d_a > d_{a^{elastic}}$ in the epoxy model.

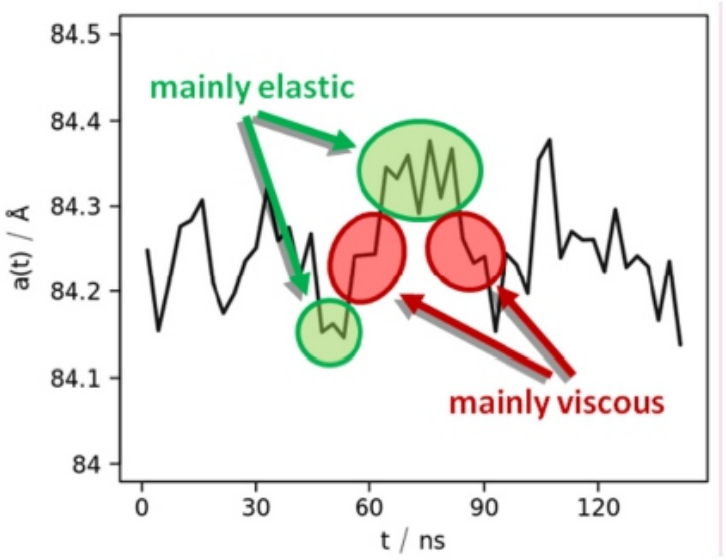

Figure 3. Dimension of the cell vector a as a function of time as obtained for the epoxy polymer benchmark model. The plot shows a running average over (t, t-3 ns) to help discriminating fast fluctuations from the much slower viscous modes of reorganizing of the model. While the latter reflects rare transitions from one local energy minimum to another, elastic deformation implies fluctuations within a local energy minimum configuration.

Ideally, the elastic constants should be derived from an exclusive statistics of $\Delta a^{elastic}(t)$. For this, we however must discriminate elastic from non-elastic deformation which is far from trivial in a complex molecular material. The only guide for such differentiation is given by the different timescales of elastic deformation (fastest modes) and the usually much slower visco-elastic modes. Indeed, when sampling the occurrence profiles over short (here 5 ns) time intervals we found the standard deviations d_a in line with experimental values of the Youngs modulus [10].

In case of extended sampling over longer periods we therefore suggested to sample d_a in 5 ns intervals, and then use the overall average $\langle d_a \rangle$ as input to Eq 8 [10,15]. While this lead to excellent agreement of bulk, Youngs and shear moduli in line with the experiment, the obvious downside of this approach is the somewhat arbitrary choice of the time intervals. Moreover, few but still some of these intervals include larger scale deformation stemming from viscous modes of molecular movements. Anyway, we argue that fragmenting the statistics in time intervals converges to $\langle d_a \rangle \cong \langle d_a \text{elastic} \rangle$ for sufficiently short sampling periods, whereas the direct sampling of overall statistics implies $\langle d_a \rangle = \langle d_a \text{elastic} \rangle + \langle d_a \text{visco} \rangle$ and thus inadequate inputs to Eq 8. In ref. [10], the choice of 5 ns was motivated by choosing the sampling intervals short, whilst still providing smooth occurrence profiles for fitting the Gaussians reliably.

From a materials science perspective, the separation of (ideal) elastic and pseudo/visco-elastic modes reflects the spatial and time-depend fluctuations of elastic constants in polymer materials at the nm (ns) length (and time) scales, respectively [5,24]. From a mathematical viewpoint, the separation of scales is routinely performed by means of Fourier filtering. To bring this together, we analyzed the Fourier transforms of the simulation cell shape and dimensions as shown in Figure 4.

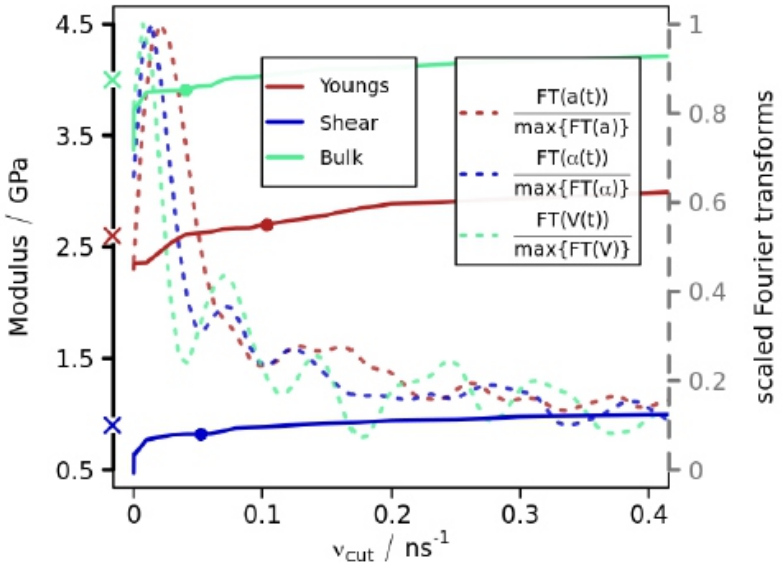

Figure 4. Fourier transforms (FT) of the fluctuations of $a(t), \alpha(t)$ and $V(t)$ being functions of ν as shown by dashed curves in red, blue and green, respectively (right axis). Estimates of $a^{elastic}(t), \alpha^{elastic}(t)$ and $V^{elastic}(t)$ are obtained from back-transformation using $\nu \geq \nu_{cut}$ filtering. On this basis, we obtain the Youngs, shear and bulk moduli (solid curves) at 300 K and 1 atm as functions of ν_{cut}, respectively (left axis). To identify the best choice of cut-off delimiters ν_{cut} for separating the time scales of fast, elastic modes and longer termed viscous reorganization, we suggest the first minimum in the corresponding FT-plot. Indeed, this leads to excellent agreement with the experimental data as indicated by (x) along the left axis [21,25,26].

The intensities of the Fourier transforms of $a(t), \alpha(t)$ and $V(t)$ show a clear peak at low frequencies $\nu < 0.05 - 0.1\ \mathrm{ns}^{-1}$, subject to the mode of deformation. In turn, a broader spectrum is found for the faster vibrational modes. To separate elastic and visco-elastic type fluctuations, we suggest Fourier-filtering by means of a cut-off frequency delimiter ν_{cut}:

$$a(t) = a^{elastic}(t) + a^{visco}(t) = FT^{-1}[FT[a(t)], \nu \geq \nu_{cut}] + FT^{-1}[FT[a(t)], \nu < \nu_{cut}] \quad (10)$$

with

$$a^{elastic}(t) \cong FT^{-1}[FT[a(t)], \nu \geq \nu_{cut}] \quad (11a)$$

$$a^{visco}(t) \cong FT^{-1}[FT[a(t)], \nu < \nu_{cut}] \quad (11b)$$

Likewise, analogous filtering of $\alpha(t)$and $V(t)$ is obtained, however using individual frequency delimiters ν_{cut} to account for the different dynamics of tensile ($\nu_{cut} = 0.1\ \mathrm{ns}^{-1}$), shear ($\nu_{cut} = 0.05\ \mathrm{ns}^{-1}$) and bulk volume ($\nu_{cut} = 0.04\ \mathrm{ns}^{-1}$) deformations.

On the basis of these approximations, we sampled the fluctuations $d_{a^{elastic}}$ and $d_{a^{visco}}$ of merely elastic $a^{elastic}(t)$ and viscous $a^{visco}(t)$ deformation modes of the simulation cell as illustrated in Figure 5. This separation of time scales leads to more reliable sampling of the elastic-type fluctuations $d_{a^{elastic}}$ as compared to the statistics taken from a series of time intervals we discussed earlier. This is also reflected by comparing our modeling results to the experimental assessment of the Youngs, shear and bulk moduli as functions of temperature, respectively.

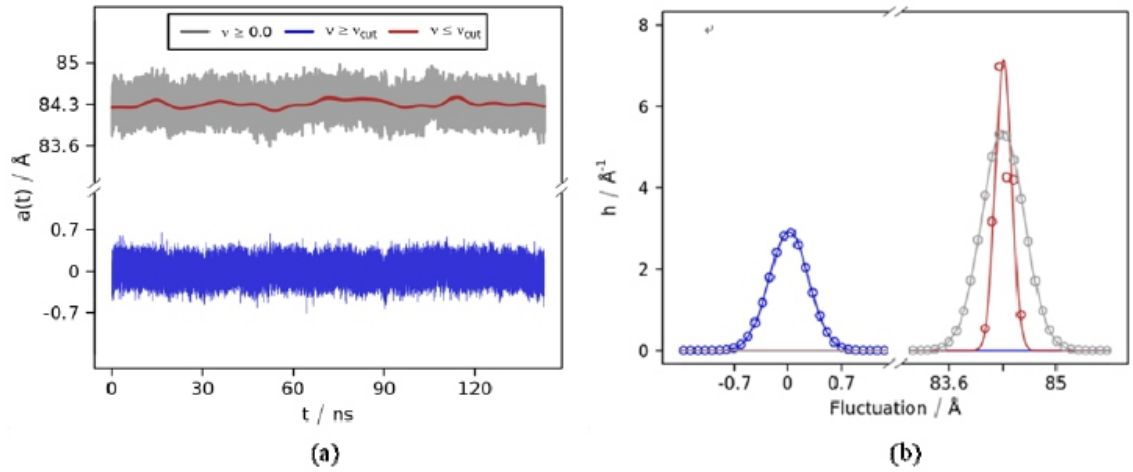

Figure 5. (a) Profiles of $a(t)$, grey curve, and its Fourier-filtered ($\nu_{cut} = 0.1$ ns^{-1}) components $a^{elastic}(t)$ and $a^{visco}(t)$ shown in blue and red, respectively. Note that the 10 ns scale shifting of the simulation cell dimension $a(t)$ is practically exclusively described by $a^{visco}(t)$, whereas the fast, elastic-type vibrations within local energy minima is obtained as $a^{elastic}(t)$. The standard deviations $d_{a^{elastic}}$ (and likewise $d_{\alpha^{elastic}}$ and $d_{V^{elastic}}$) provide reliable estimates of the Youngs, shear and bulk moduli, respectively. (b) Occurrences h of $a(t)$, $a^{elastic}(t)$ and $a^{visco}(t)$ and corresponding Gaussian fits shown as dots and solid curves, respectively. The color code is analogous for both figures.

For such benchmarking, we decided to focus on the study of Littell et al. in which a consistent series based on a constant experimental setup was used (Figure 6) [21]. Likewise, we analyzed the elastic properties as a function of temperature using the same atomic configuration as starting point for MD runs at 300,350,400 and 450 K, respectively. While the modeling data obtained at 300 and 350 K nicely agrees with the experimental data available, we find that a clear-cut separation of time scales for elastic/viscous deformation modes may not be achieved for MD runs at 400 K or even larger temperatures. This limitation is in line with the intrinsic difficulty in discriminating elastic and viscous deformations in polymers near their glass transition temperature (~440 K) [10].

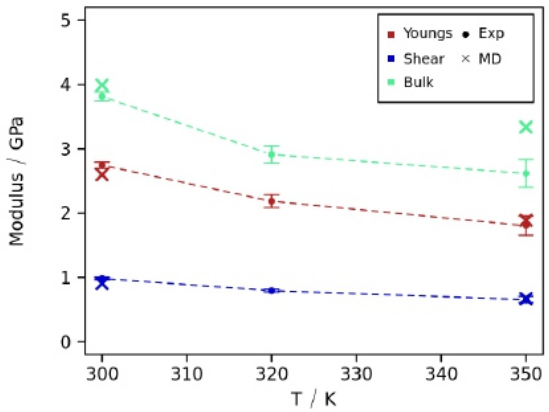

Figure 6. Elastic moduli of epoxy polymers cured from bisphenol F diglycidyl ether and 4,6-diethyl-2-methylbenzene-1,3-diamine as functions of temperature. The dashed lines show the average results of tensile and compression experiments performed at a strain rate of 10−3 s−1 as taken from ref. [21]. Youngs, shear and bulk moduli as obtained from MD simulations at 300 and 350 K are marked as (x) using red, blue and green color, respectively.

5. CONCLUSIONS

Molecular modeling and simulation approaches are continuously catching up with the complexity of modern molecular materials. While early simulation studies of polymer networks mainly coped with the appropriate description of molecular interactions [11], current computational resources allow all-atom modeling based on robust empirical interaction potentials such as the OPLS or GAFF force-fields [27,28]. Clearly, the length scales inherent to proper modeling of complex polymer networks still oppose a full ab-initio description, in particular when it come to dynamics calculations. However, reactive force-field approaches and combined quantum/classical techniques help to provide near ab-initio accuracy where needed, namely for the cross-links between the polymer precursors [10,15,29–31].

This not only boosted the quality of assessing the atomic interactions of a given polymer model, but also greatly helped to create the model itself. Indeed, for non-crystalline networks of molecules it is far from trivial to provide realistic starting structures and extensive relaxation of the simulation systems is needed to ensure convergence. With typically dimensions exceeding the 10000 atoms scale and relaxation times beyond the 10 ns scale, the use of smart molecular mechanics models is likely to prevail the state-of-the-art also in the nearer future.

The issue of structural complexity, and the time-dependent diversity of local ordering in molecular materials is also reflected in the analysis and the understanding of mechanical properties. The techniques reviewed in the present work offer a versatile toolbox for this purpose. Among these methods, the computational demand differs quite significantly. Temperature-dependent analyses of molecular dynamics simulation runs are clearly the most expensive option—but allow exciting atomic scale insights into complex network dynamics in parallel to computing macroscopic properties. Thus, for the actual understanding of molecular materials we consider molecular simulations as an important, if not indispensable extension to the experiment.

ACKNOWLEDGEMENTS

This work was funded by the Graduiertenkolleg GRK 2423, “Frascal” of the Friedrich- Alexander-Universität Erlangen-Nürnberg.

CONFLICT OF INTEREST

The authors declare no conflict of interest.

REFERENCES

1. *Kresse G, Furthmüller J (1996) Efficiency of ab-initio total energy calculations for metals and semiconductors using a plane-wave basis set. Comp Mater Sci 6: 15–50.*
2. *Giannozzi P, Baseggio O, Bonfà P, et al. (2020) Quantum ESPRESSO toward the exascale. J Chem Phys 152: 154105.*
3. *Gale JD (2005) GULP: Capabilities and prospects. Z Krist-Cryst Mater 220: 552–554.*
4. *Treloar LRG (1975) The Physics of Rubber Elasticity, Oxford: Oxford University Press.*
5. *Doi M, Edwards SF (1986) The Theory of Polymer Dynamics, Oxford: Clarendon Press.*
6. *Rapaport DC (1996) The Art of Molecular Dynamics Simulation, Cambridge University Press.*
7. *Frenkel D, Smit B (2002) Understanding Molecular Simulation: From Algorithms to Applications, Elsevier.*
8. *Landau LD, Lifshitz EM (1958) Statistical physics: Theory of the condensed state, In: Sykes JB, Kearsley MJ, Course of Theoretical Physics, Pergamon Press.*
9. *Lebowitz JL, Percus JK, Verlet L (1967) Ensemble dependence of fluctuations with application to machine computations. Phys Rev 153: 250.*
10. *Konrad J, Meissner RH, Bitzek E, Zahn D (2021) A molecular simulation approach to bond reorganization in epoxy resins: From curing to deformation and fracture (in press). ACS Polym Au.*

11. Everaers R, Kremer K (1996) Elastic properties of polymer networks. J Mol Model 2: 293–299.
12. Lee H, Neville K (1987) Chemistry and Technology of Epoxy Resins, 2 Eds., CRC Press.
13. Ellis B (1993) Chemistry and Technology of Epoxy Resins, Springer Science + Business Media.
14. Cai H, Li P, Sui G, et al. (2008) Curing kinetics study of epoxy resin/flexible amine toughness systems by dynamic and isothermal DS. Thermochim Acta 473: 101–105.
15. Meissner RH, Konrad J, Boll B, et al. (2020) Molecular simulation of thermosetting polymer hardening: Reactive events enabled by controlled topology transfer. Macromolecules 53: 9698– 9705.
16. Fast L, Wills JM, Johansson B, et al. (1995) Elastic constants of hexagonal transition metals: Theory. Phys Rev B 51: 17431.
17. Karki BB, Stixrude L, Clark SJ, et al. (1997) Structure and elasticity of MgO at high pressure. Am Mineral 82: 51–60.
18. Nye JF (1985) Physical Properties of Crystals: Their Representation by Tensors and Matrices, Oxford: Oxford University Press.
19. Yu R, Zhu J, Ye HQ (2010) Calculations of single-crystal elastic constants made simple. Comput Phys Commun 181: 671–675.
20. Arrhenius S (1889) Über die Reaktionsgeschwindigkeit bei der Inversion von Rohrzucker durch Säuren. Z Phys Chem 4: 226.
21. Littell JD, Ruggeri CR, Goldberg RK, et al. (2008) Measurement of epoxy resin tension, compression, and shear stress-strain curves over a wide range of strain rates using small test specimens. J Aerospace Eng 21: 162–173.
22. Parrinello M, Raman A (1982) Strain fluctuations and elastic constants. J Chem Phys 76: 2662– 2666.
23. Duan G, Lind ML, Demetriou MD, et al. (2006) Strong configurational dependence of elastic properties for a binary model metallic glass. Appl Phys Lett 89: 151901.
24. Muliana AH (2021) Spatial and temporal changes in physical properties of epoxy during curing and their effects on the residual stresses and properties of cured epoxy and composites. Appl Eng Sci 7: 100061.
25. Bajpai A, Alapati AK, Klingler A, et al. (2018) Tensile properties, fracture mechanics properties and toughening mechanisms of epoxy systems modified with soft block copolymers, rigid TiO2 nanoparticles and their hybrids. J Compos Sci 2: 72.
26. Kallivokas SV, Sgouros AP, Theodorou DN (2019) Molecular dynamics simulations of EPON- 862/DETDA epoxy networks: Structure, topology, elastic constants, and local dynamics. Soft Matter 15: 721–733.
27. Jorgensen WL, Maxwell DS, Tirado-Rives J (1996) Development and testing of the OPLS allatom force field on conformational energetics and properties of organic liquids. J Am Chem Soc 118: 11225–11236.
28. Wang J, Wolf RM, Caldwell JW, et al. (2004) Development and testing of a general amber force field. J Comput Chem 25: 1157–1174.
29. Varshney V, Patnaik SS, Roy AK, et al. (2008) A molecular dynamics study of epoxy-based networks: Cross-linking procedure and prediction of molecular and material properties. Macromolecules 41: 6837–6842.
30. Nouri N, Ziaei-Rad S (2011) A molecular dynamics investigation on mechanical properties of cross-linked polymer networks. Macromolecules 44: 5481–5489.
31. Li C, Strachan A (2010) Molecular simulations of crosslinking process of thermosetting polymers. Polymer 51: 6058–6070.

·ISSN : 2372-0484

Development of Compressive Testing Device for Glass Fiber Based Single Face Corrugated Structure Sheet, and Estimation of Buckling Strength of Straight Panel of That Structure Sheet

Songtam Laosuwan[1,2] and Shigeru Nagasawa[1,*]

[1] Department of Mechanical Engineering, Nagaoka University of Technology, 1603-1 Kamitomioka, Nagaoka, Niigata 940-2188, Japan

[2] Department of Mechanical Engineering, Pathumwan Institute of Technology, 833 Rama 1 Rd., Pathumwan, Bangkok, 10330 Thailand

* Correspondence: Email: snaga@mech.nagaokaut.ac.jp.

ABSTRACT

This work aims to reveal the in-plane-compressive characteristics of Glass Fibre based single face corrugated Structure Sheet (GFSS) by developing a loading holder of the both ends of the panel of GFSS in the direction of the cross machine direction. A grooved end-support device was developed and exmined. In order to set stably and quickly a straight panel of GFSS on the compressive-testing apparatus, the width and the depth of the holder's groove were varied against the geometrical size of the panel, and the stability and reproducibility of compressive deformation of the panel was experimentally investigated. When changing the height of the panel and reinforcing the both ends of the panel by dipping instant adhesives, the deformation behavior and the buckling strength was characterized in three modes: a short height crushing without lateral deflection, a small lateral deflection mode as the intermediate state, and a triangle-like folding as a long height crushing.

Keywords: end crush; bending; buckling; fabrics of glass fibre; compressive strength

Abbreviations: λ: A wave length (pitch) of GFSS, 7.1 mm; h_o: t_L; t_W: A height of GFSS, a thickness of liner, and a thickness of wave layer; hf: A height of free zone of panel supported by upper/lower grooves on holder; h_g: A depth of groove of the edge holder, 10 mm; w_{gs}: A width of groove of the edge holder for the straight panel, 3, 3.2, 3.5 and 4.0 mm; H: A height of specimen of GFSS, $H = 2h_g + h_f$; B_S: A width of straight specimen of GFSS, 46 mm (=6.5 λ). It includes closed 6 waves; F: A compressive force on a GFSS panel in the heightwise direction (N), f = F/B: a compressive line force applied to GFSS (N/mm). The width of panel was chosen as B_S; f_p: A peak maximum line force of f = F/B during a compressive test; d: A compressive displacement of the fixture on a press machine at the heightwise compressive test of GFSS; dp: A corresponded displacement of the fixture to the peak maximum line force fp; $Fcr = \pi^2 EI/(kh_f)^2$: An Eulerian critical buckling force at a compressive test of straight panel. Here, k was 0.5 when the upper/lower ends of panel were fixed with rotation. I is the equivalent second moment of area in the in-plane cross (heigtwise) direction of GFSS when B = BS, while E is the equivalent Young's modulus of GFSS. $f_{cr} = F_{cr}/B_S$ is the critical buckling strength as line force (N/mm); $EI = (B_S/B_{3p})(L^3/48)(\Delta F/\Delta\delta)$: A bending stiffness in the in-plane cross (heigtwise) direction of GFSS panel when B = Bs. Here, L = 30 mm was a span length of specimen, B3p = 25 mm = 3.5λ was a width of specimen at three-point-bending test. The gradient of force by deflection $\Delta F/\Delta\delta$ was experimentally measured from a three point bending test of GFSS

1. INTRODUCTION

Glass fiber based structure sheet (GFSS) is commercially produced and used as a core sheet for making a reinforced plastics structure [1]. A combination of two layers as the liner and the corrugated medium is called as a single face type in the packaging industry of corrugated fiberboard (CFB) [2–4]. A GFSS is geometrically similar to the single face structure of CFB, but the joint mechanism of liner and wave layer is different from that of CFB. They (a liner and a wave layer) are interweaved against common crossed fibres of liner layer. A GFSS is composed of the wave and the liner layers, which are periodically intersected with each other. The wave layer makes a bridge across the liner layer by knitting. As for the mechanical properties of CFBs, there are various testing and measurement methods such as the standard JIS Z 0401, JIS Z 0212. To know the mechanical strength of CFBs, the flat crush test (out-of-plane compressive test), the edgewise crush test (end crush test, an in-plane height wise compressive test) [5–8], the ring crush test (in-plane compressive test) of a liner or intermediate sheet, and a compression test on a corrugated box are well known. However, since a GFSS is based on glass fibre fabrics, it is seemed that these testing methods are not applied to estimate the mechanical properties of GFSS without any consideration or modification. GFSS is made of single-face corrugated glass fiber fabrics and a light-weight sheet. It has a high stiffness in the in-plane height wise and flexural for bending in the out-of-plane. GFSS seems to be suitable for making a curved structure of reinforced resin. It is convenient for making electric wave shielding and then well used for making a rotor of electric driving motor. The authors developed a flexible-fitted fixture for gripping the specimen and investigated the tensile strength and the elongated behavior of GFSS in the producing machine direction (Machine direction, MD) [9,10].

Regarding the in-plane tensile test of GFSS in the MD, an advanced fixing condition of GFSS specimen was developed using a combination of insert pins and instant adhesives. This fixture device was designed by referring the tensile test method of CFB using fixing pin and wax filling [11].

Wahab et al. [12] studied a fundamental usage of single parallel pins for fixing a double face corrugated fiberboard (CFB) made of kraft paper. Cox [13] has studied effects of orientation of the fibers on the stiffness and the strength of paper and other fibrous materials.

When designing various packaging panels of GFSS, the in-plane height wise compressive (or buckling) strength of GFSS is necessary for estimating the mechanical behavior of panel structure, and needless to say, that of a resin-reinforced GFSS is important for determining the strength of structural panels. But the in-plane height wise compressive strength of GFSS is not sufficiently investigated due to the fragile behavior [2] and the complexity of three-dimensional structure composed of a wave layer and a liner layer [5].

As advantages, GFSS has easiness of cylindrical bending for making a curved wall structure. However, the mechanical properties of GFSS under bent condition was not well known due to its complex structure and fragile property. The buckling mode of breaking zone of cylinderical wall is not well understand yet.

Therefore, in this work, to reveal the compressive strength of a straight panel of GFSS, a fixing device for compressive loading on a vertical (height wise) panel of GFSS was developed, and the compressive test of the straight panel was carried out, when varying the groove profile of the fixture for supporting the upper/lower ends of GFSS panel.

2. MATERIALS AND METHODS

2.1. Principle of in-plane compressive test and condition of specimen

The primary specifications of GFSS are the basic weight or the average density of glass wires, the pitch size of the flute and so on. A prepared specimen of GFSS was illustrated in Figure 1 [1].

Here, a total outside height of h0, a wave length of λ, a liner thickness of tw, a wave layer thickness of tL of GFSS were arranged in Table 1. According to JIS Z0104-1003, since B type flute of corrugated paper board has ho = 3 mm, λ = 6 mm, the specification of GFSS is geometrically similar to the B type flute. Raw sheets of GFSS were produced using the twisted yard, E-glass of Nittobo, ECG75-1/2-3.8S (Fineness: 135 (fineness: 135 ± 8.1 TEX, a diameter of filament: 9.5 μm, number of twists: 3.8 per 25 mm) [14–16]. After knitting, a few of acrylic based adhesives were injected on the raw sheets of GFSS. The cord count (density) of the upper wave layer and the lower liner of GFSS was 25 ± 1 per 25mm width in the longitudinal direction (Machine transforming direction) and in the lateral direction (cross machine direction), respectively.

As an advanced purpose, a compressive strength of box structure of GFSS is attractive. Figure 2a illustrates a box of GFSS subjected to a compressive load. However, since GFSS is a complex structural sheet, an in-plane heightwise compressive strength of a simple straight panel of GFSS is here investigated, as shown in Figure 2b.

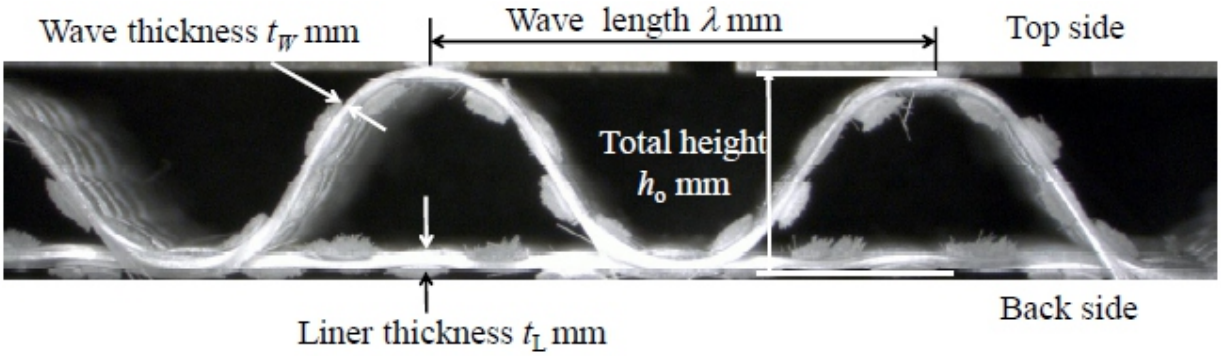

Figure 1. Side view of two flutes of GFSS (glass fibre based single face corrugated structure sheet).

Table 1. Structural dimensions of a side view of GFSS.

Geometrical parameters of GFSS shown in Figure 3	Average of 5 samples (maximum-minimum)
Total outside height, h_o (mm)	3.0 (3.05–2.95)
Wave-length λ (mm)	7.1 (6.86–7.58)
Liner thickness t_L (mm)	0.25 (0.17–0.31)
Wave thickness t_W (mm)	0.25 (0.14–0.30)

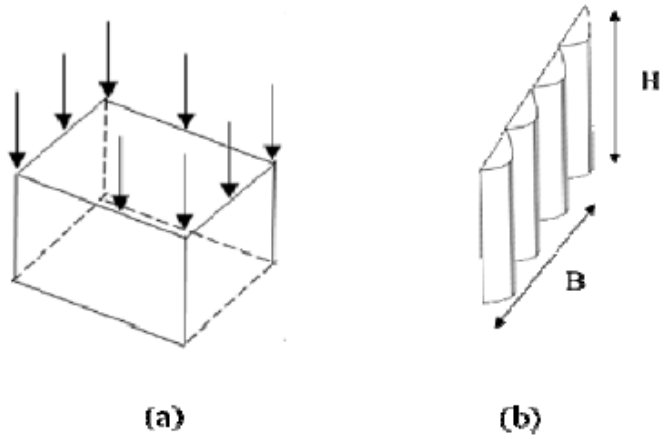

Figure 2. General views of a straight panel of GFSS in heightwise direction and box structure as example of closed panels subjected to in-plane heightwise load. (a) Compression of a box or closed panels, (b) General view of a rectangle straight panel of GFSS.

When considering the compressive strength of such a panel which is some elemental parts of a box, a central zone of panel is often noted from the aspects of panel strength. The height of panel is restricted by a kind of folded hinge of top or bottom flap. The upper/lower edges of panel are normally fixed to prohibit to rotate in the out-of-plane of panel. Therefore, when varying the height of panel in the heightwise direction, the deformation of panel seems to be classified in two modes, shown in Figure 3a,b. The former ($H \leq 4h0$) is understood as an edgewise crush (ISO 3037, edge crush test, ECT) without any lateral deflection of panel. Here, regarding the B flute type, a height of panel specimen is 32 mm for ECT, whereas the height of guide block is chosen as 20 mm [7,8].

Therefore, a free height of panel is expected 12 mm as 4 times of ho. The latter ($H >> 4h0$) seems to be deflected in the lateral direction at the central zone, while the upper/lower edges are fixed with rotation in the out-of-plane. Since the deflected direction of out-of-plane is generally unknown, the deflection was tentatively assumed to be on a wave layer side (b-1) or a liner layer side (b-2) in this picture.

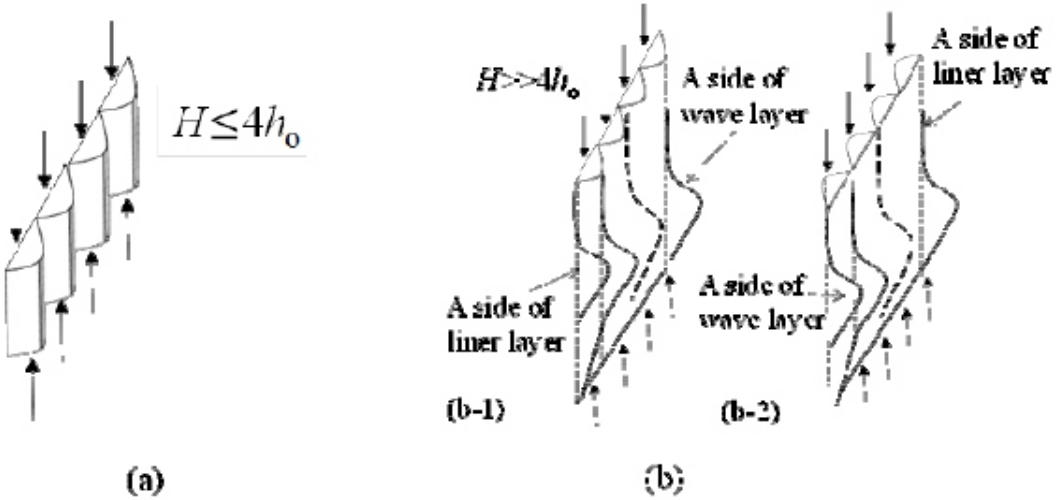

Figure 3. Deflection modes of GFSS panel subjected to heightwise compressive load when fixing out-of-plane rotational freedom of upper/lower edges of panel. (a) Compressive state of a short height panel at the end crush testing without lateral bending; (b) Compressive state of a long height panel at the lateral buckling of tall pillar or shell.

2.2. Experimental conditions of straight panel at compressive loading

2.2.1. Set-up condition of straight panel specimen

To investigate the heightwise buckling strength of GFSS, a grooved aluminum plate (edge holder) was prepared as shown in Figure 4a, which was used for compressing a straight panel of GFSS. Figure 4b illustrated an assembled state of a straight panel of GFSS using the upper/lower edge holders. The upper edge holder was set up on the upper rod of the compressive machine, while the lower edge holder was mounted on the base block of the compressive machine. The straight panel of GFSS was inserted into the upper and lower grooves without applying any self weight of the upper holder to the panel. For examining the compressive test of a 46 mm-width panel of GFSS, the maximum capacity of the load cell was 10 kN.

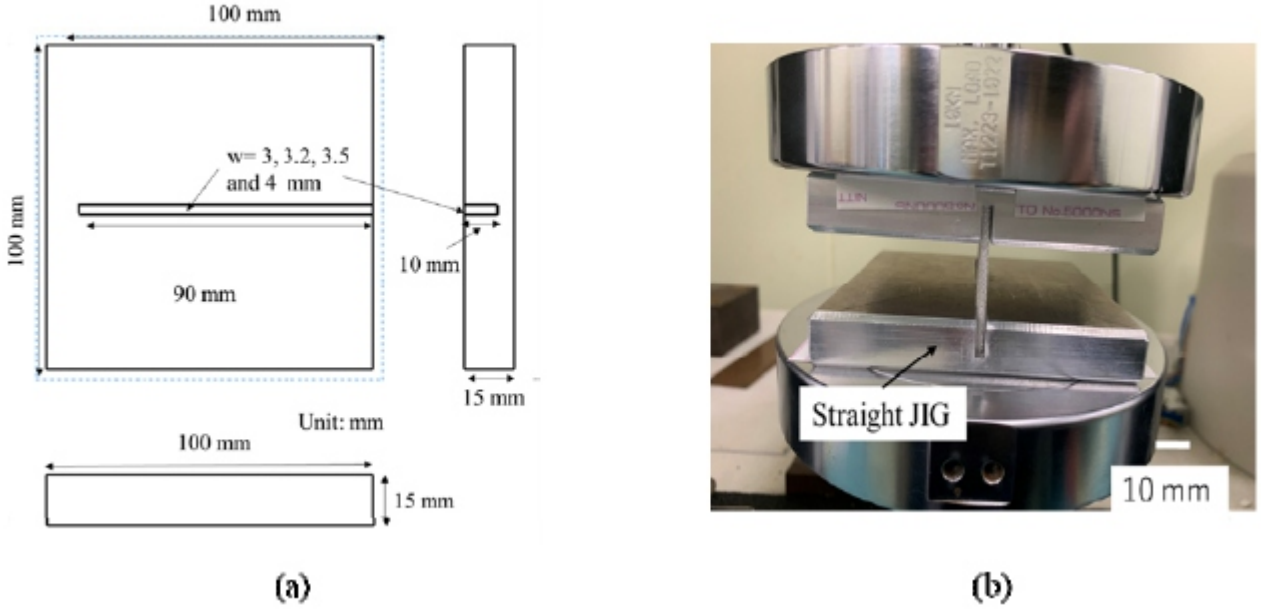

Figure 4. Experimental apparatus of in-plane compressive test of a straight panel of GFSS. (a) A half of edge holder of straight panel of GFSS, (b) Setup of straight panel on upper/lower edge holders.

The depth of groove hg was chosen as 10 mm which was deeper than 3 times of the height of GFSS ho = 3.0 mm. When using the zero depth of groove as the panel holder, the panel of GFSS could not be kept in the vertical attitude. Therefore, appropriate groove is necessary for the compressive test. The width of groove wgS was chosen as 3.0, 3.2, 3.5 and 4.0 mm, which were compared for knowing the effects of the clearance wgS-ho. Herein, wgS = 3.0 mm was assumed to be the respresentative width when chaning the free height of panel.

Figure 5 shows a zoomed-up side view of GFSS specimen and a schematic of specimen which was clamped by the upper/lower edge holders to know the size effects of the free zone. The number of specimens were five for each case. The side views of compressed GFSS was recorded as video movies for knowing occurred deflection modes. As for the size of specimen of GFSS in the case of straight panel, the width of specimen BS = 46 mm was fixed as 6.5 λ of the wave layer, while the height of specimen H = 25, 30, 40, 50, 60, 70, 80, 90, 100, 110, 120, 130 and 140 mm was chosen.

Namely, the height of free zone of specimen hf = H-2hg = 5–120 mm was chosen. The compressive displacement of the edge holder was chosen as d = 4 mm at hf = 5 mm, and d = 8 mm for hf = 10–120 mm, while the compressive velocity V = 0.21 mm/s was fixed during the compressive test. Through the compressive test of the straight panel of GFSS, the relationship between the displacement d and the line force f = F/BS was measured and the peak maximum line force fp was investigated.

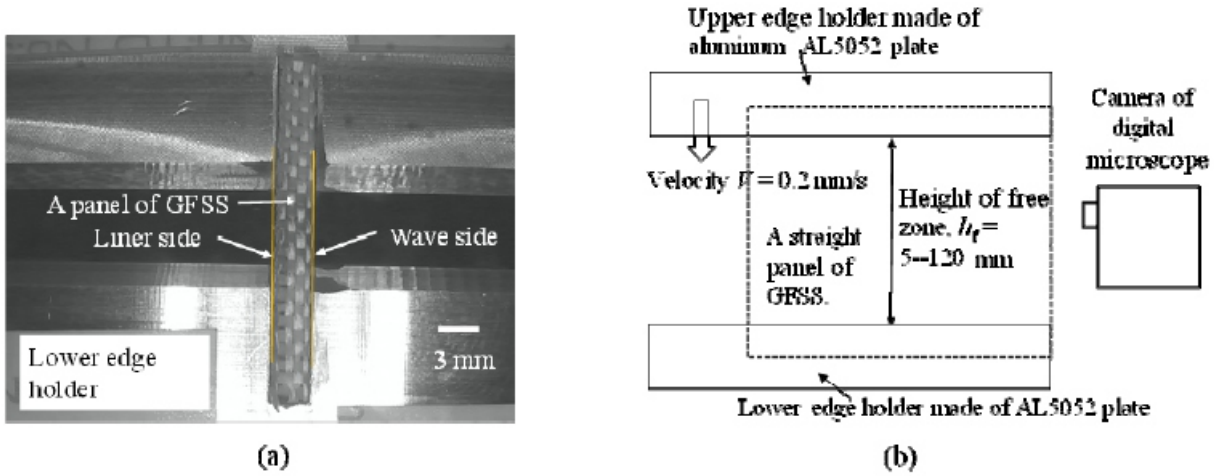

Figure 5. Zoomed-up views of a straight panel of GFSS for compressive test. (a) Side view of compressed panel; (b) Straight panel and upper/lower holders.

Since the crush of both ends of a panel affects the initial buckling behavior of the panel, a brief reinforcement by adding instant adhesives on the both ends of the panel was considered as shown in Figure 6. On four points on the edge of 6 waves of a straight panel, instant adhesives (liquid arone alpha) were dipped, and the panel was dried for 24 h after dipping. Comparing a weight variation of the panel with this dipping, its additional weight was totally 0.116 g (as the average) on the edge of the straight panel.

All the experiments were carried out in a room temperature of 296 K and in a humidity of 50% RH. Five pieces of GFSS specimen were examined for the basic and reinforced models.

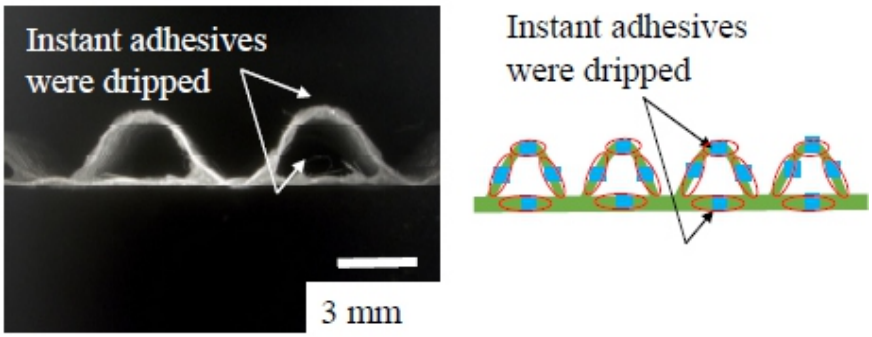

Figure 6. Some brief reinforcement of edges of GFSS by dipping instant adhesives at a straight panel.

2.2.2. Discussion model of critical buckling strength on a straight panel

Regarding the out-of-plane bending stiffness of GFSS, the three point bending test [17] was applied to a rectangle sheet of GFSS which had a width of B3p = 25 mm and a heightwise length of 35 mm. The punching tool had a round-edge of 0.36 mm radius and the supporting anvil had a groove which had a

span length of L = 30 mm. Since the GFSS was asymmetric sturucture of wave layer and liner layer, as two kinds of pushing direction, the liner side and the wave side were pushed respectively by the punching tool, while the GFSS was mounted on the supporting anvil. From the Timosienko's beam deflection theory [17], the bending stiffness of D = EI is estimated from Eq 1. Here, the gradient of force by deflection ΔF/Δδ was experimentally estimated as the first order coefficient of linear approximation for the early stage of 0.03 mm < δ < 0.4 mm (corresponding from 20% to 80% of peak maximum load) from the three point bendind test of GFSS.

$$D=EI = (B_S/B_{3p})(L^3/48)(\Delta F/\Delta\delta) \quad (1)$$

To estimate the critical buckling strength of a straight panel supported by the upper/lower grooves, a simple beam buckling theory by Timosienko was tried to be applied to this compressing test. Denoting the free surface length of panel as hf, the out-of-plane bending stiffness as D = EI (E: Equivalent Young modulus, I: the second order sectional moment of 7.5 wave length = BS), and the factor of boundary condition as k, a line force of critical buckling force fCR is expressed as Eq 2 [18].

$$F_{CR}/B_S = f_{CR} = \pi^2 D/B_S/(kh_f)^2 \quad (2)$$

Herein, since the both (upper/lower) ends of a panel were assumed to be fixed with rotation, k was determined as 0.5. From the three point bending flexural test of GFSS across the flute structure, as a value of D was analyzed and gotten from Eq 1, the critical line force fCR was estimated by Eq 2.

3. RESULTS AND DISCUSSIONS

3.1. Mechanical sizes and properties of GFSS

Seeing the 3 points bending flexural test of GFSS specimens (shown in Figure 7), values of the bending stiffness D (=EI) (estimated by Eq 2), the sectional area A, and the second moment of area I calculated from a CAD data were shown in Table 2. It was found that the out-of-plane bending stiffness of GFSS was a little different with respect to the pushing direction. Namely, the bending stiffness of wave layer's pushing was about 32% larger than that of liner layer's pushing.

Referring the tensile test of GFSS [10], a nominal tensile Young's modulus of a plain glass fibre sheet which was equivalent to the liner sheet of GFSS was estimated as E = 6.2–6.3 GPa. Therefore, the three-point-bending test based Young's moudulus was about 18% compared with the in-plain tensile mode.

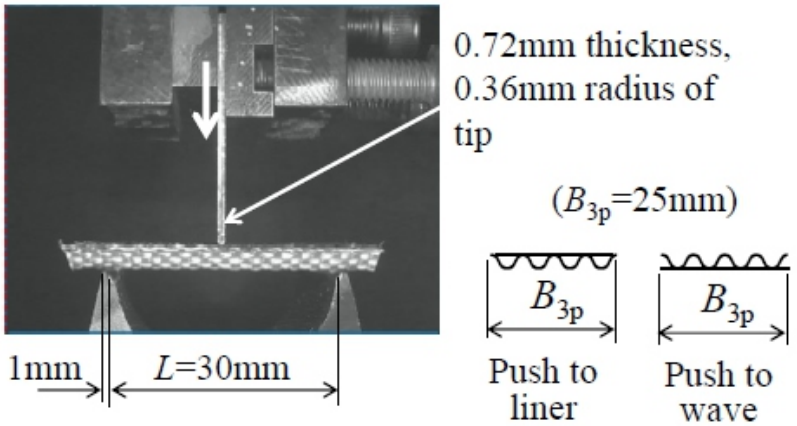

(a) Front view of specimen (b) Side view of specimen

Figure 7 Schematics of three point bending test of GFSS specimen.

Table 2. In-plane mechanical sizes and properties of GFSS which had 6.5 waves of flutes.

Mechanical condition of specimen and fixture	Estimated Young's modulus E MPa from the measured EI by the calculated I.	Measured bending stiffness D (=EI) (Yong's modulus x a second moment of area) when L = 30 mm	Sectional area of 6.5 waves of GFSS A (mm^2), calculated from a CAD drawing data	Second moment of area of 6.5 waves of GFSS, I (mm^4), calculated from a CAD drawing data
The three-point bending test of GFSS (liner layer was pressed by using a blade).	21609/21.66 = 997.6 MPa	21609 Nmm^2 (Standard deviation, 403.4 Nmm^2, 1.8%)	26.52 mm^2	21.66 mm^4
The three-point bending test of GFSS (wave layer was pressed by using a blade).	28595/21.66 = 1320.2 MPa	28595 Nmm^2 (Standard deviation, 876.0 Nmm^2, 3.1%)		

3.2. Buckling behavior of straight panel and load response

Figure 8 shows representative compression processes of straight panel which had hf = 5, 20, 40 and 80 mm at wgs = 3mm without dipping instant adhesives. In Figure 8a hf = 5 mm and (b) hf = 20 mm for the displacement of 5 mm, there were not any large lateral deflection (in the out-ofplane), but a local bulging appeared to occur in the in-plane direction at the free zone and also at the both ends of the panel. Figure 8c shows a representative compression process of a middle span of hf = 40 mm, while (d) shows that of a long span of hf = 80 mm. When hf > 30mm, the triangular buckling as a lateral deflection occurred at the middle zone. Herein, the moving direction of deflection was observed in two directions with the liner side and the wave side of the panel.

Regarding the compressive test of the straight panel without dipping instant adhesions, Figure 9 shows the relationship between the compressive force f = F/BS per unit width of the specimen (the line force) and the displacement of upper edge holder d. The line force f was kept in a certain resistance in a range of d < 8 mm at hf < 30 mm, while it had a peak maximum of line force in a range of d < 3 mm at hf > 30 mm. Seeing Figures 8 and 9, since the critical condition of lateral deflection as the out-of-plane buckling appeared to occur at hf = 30 mm, it was found that the peak maximum line force (at the early stage for d < 3 mm) corresponded to the occurrence of out-of-plane buckling. Referring the crtical condition of edge crush test (ECT), the corresponded height of free zone is estimated as hf = 4h0 = 12 mm. In this experiment without dipping instant adhesives, since the both ends of the panel was easily crushed due to its fragile structure and then as the in-plane reaction force decreased, the experimental critical condition of lateral buckling appeared to increase up to hf = 30 mm.

Figure 10 shows representative compression processes of a straight panel which had hf = 5, 20, 40, 80 mm and wgs = 3 mm when dipping instant adhesives on the both ends. Namely, in this case, the both ends of the panel were reinforced by a small volume of resin materials.

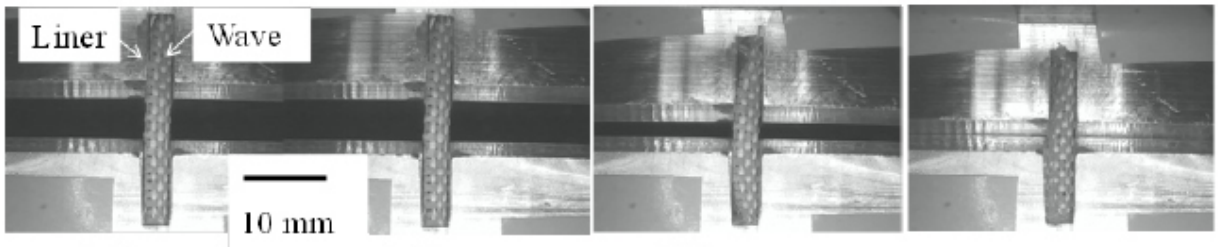

(a)

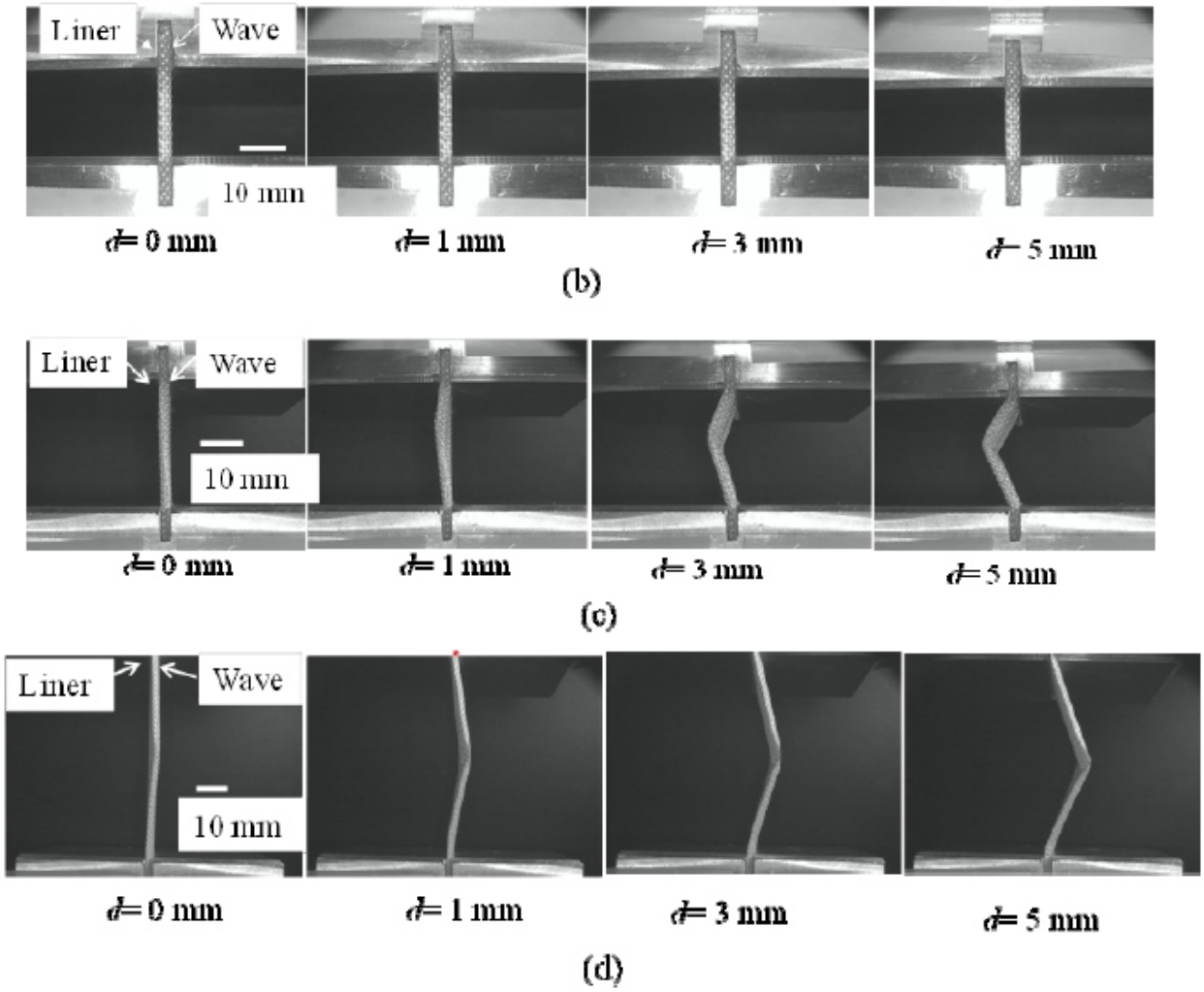

Figure 8. Deformation behavior of GFSS during in-plane compression at a width of groove wgs = 3mm without dipping instant adhesives (not reinforced). (a) In a case of the height of free zone hf = 5 mm; (b) In a case of the height of free zone hf = 20 mm; (c) In a case of the height of free zone hf = 40 mm; (d) In a case of the height of free zone hf = 80 mm.

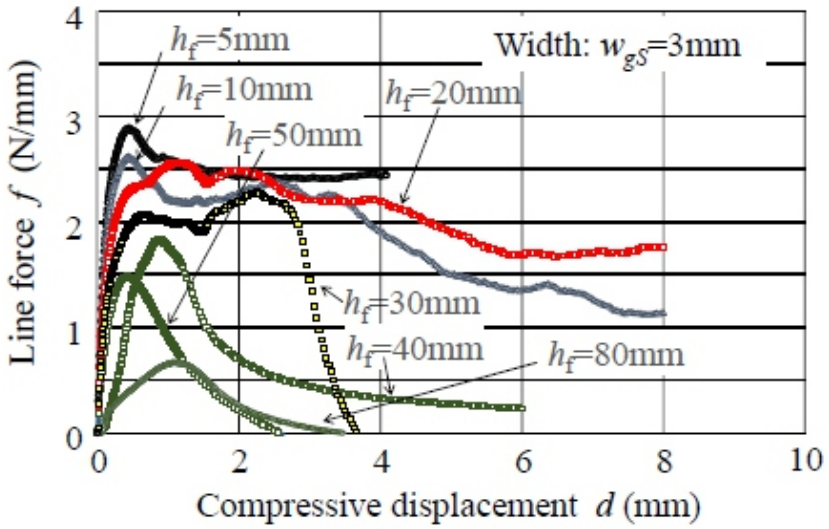

Figure 9. Load response diagram of compressive test of straight panel when varying hf without dipping instant adhesives (not reinforced).

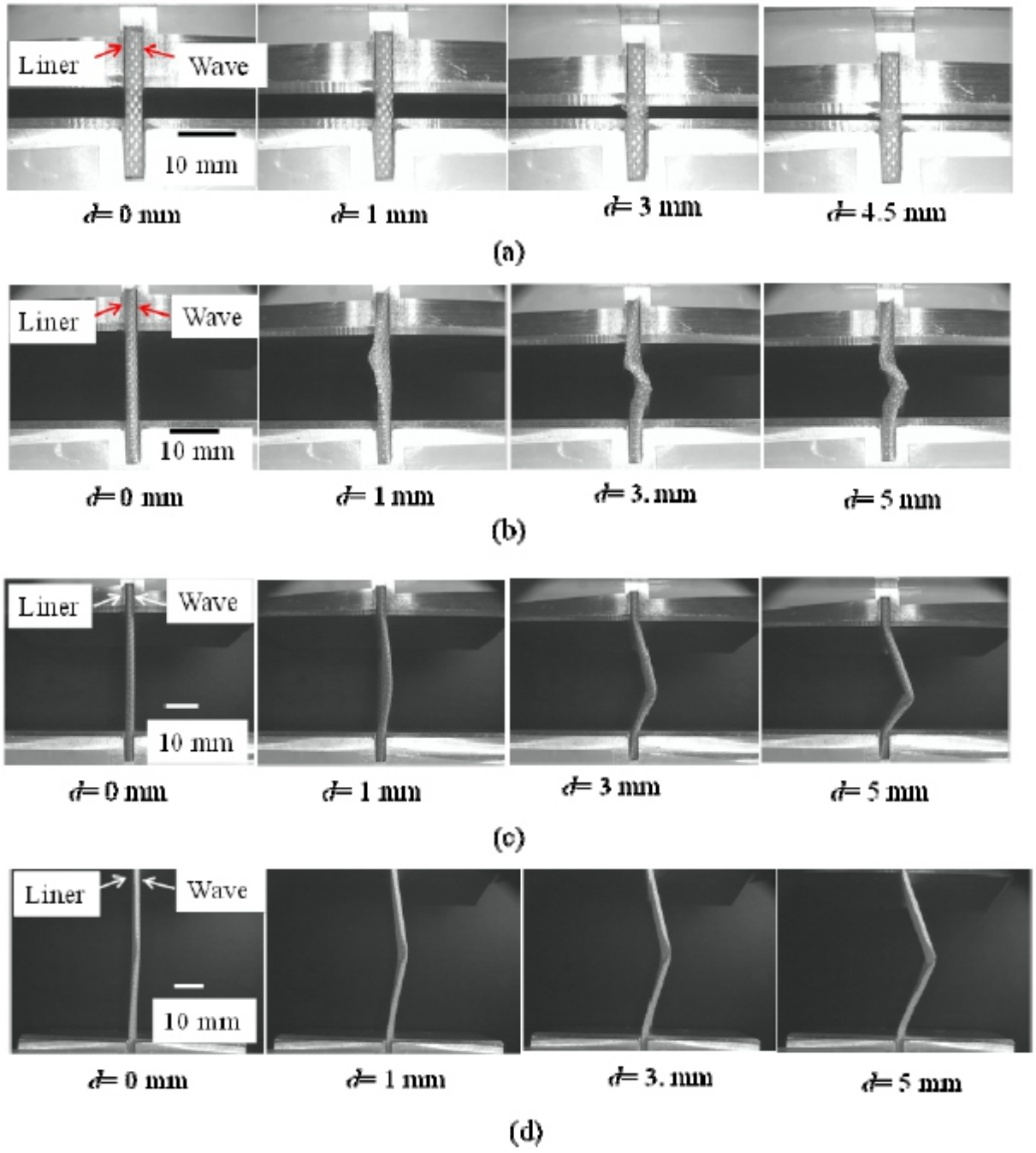

Figure 10. Deformation behavior of GFSS during in-plane compression at a width of groove wgs = 3mm with dipping instant adhesives (reinforced by glue). (a) In a case of the height of free zone hf = 5 mm; (b) In a case of the height of free zone hf = 20 mm; © In a case of the height of free zone hf = 40 mm; (d) In a case of the height of free zone hf = 80 mm.

Figure 11 shows the relationship between the compressive line force f and the displacement of the upper edge holder d, when the both ends of the panel was dipped with instant adhesives.

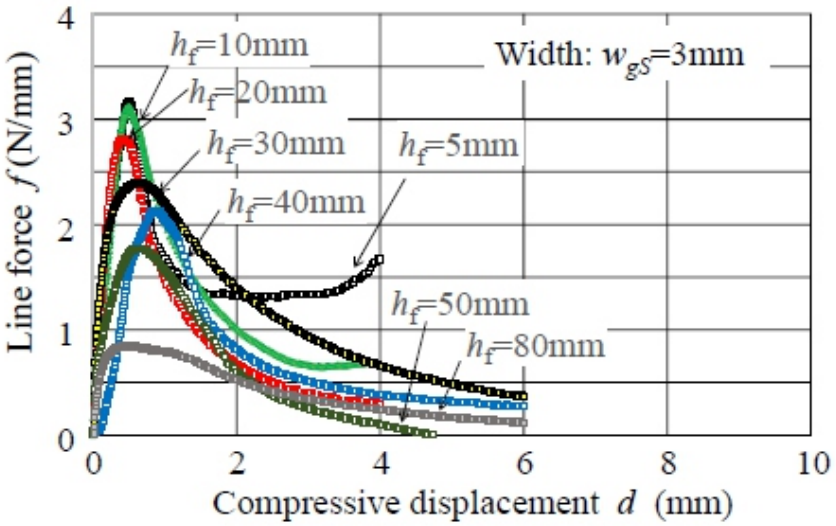

Figure 11. Load response of compressive test of straight panel when varying hf with dipping instant adhesives (reinforced by glue).

In this experiment, the peak maximum of line force remarkably occurred in the early stage (d < 2 mm). When hf = 5 mm, as any out-of-plane buckling was not observed, a certain level of compressive resistance was kept for a range of d < 4 mm. The out-of-plane buckling occurred for hf >10 mm. This transition condition seemed to be caused from the crtical condition of ECT: 4h0 = 12 mm. Seeing Figures 8–11, it was found that a certain saturated resistance of the line force appreaed for hf < 30 mm when the lateral buckling did not occur at that timing. Since this saturation apted to disappeare or vary when the compressive displacement increased furthermore, that was here called as the quasi-saturated. This seemed to be caused from the edge crush mode of the panel. Figure 12 shows the quasi-saturated resitance of line force after passing the peak maximum. Here, to briefly detect the saturated state of the compressive resistance, the quaqsi-saturated line force was evaluated for a short duration when d > 3mm. The quasi-saturated state was detected for hf <30 mm in Figure 12. In Figure 9, the short height condition of hf < 30mm showed a certain resistance larger than 2 N/mm due to this quasi-saturated state by the in-plane end crushing mode, while the long height condition of hf > 30mm showed a large lateral deflection characterized by the triangle-like deflection. In the latter, only one peak force occurred, whereas there were some quasisaturated resistance by the in-plane end-crushing mode or the out-of-plane bulging of the panel in the former case. In the middle zone of 20 mm < hf < 30 mm, the deformation consisted of the in-plain end crush mode and the lateral defelection mode under the end-fixing condition, although the former (in-plane end-crush) was the primary mode when the both ends pressure fitted to the groove's bottoms by the initial crushing of the both ends (it was performed without instant adhesives). In the case of the reinforced condition shown in Figure 11, the reinforced ends contributed to make the span length of the panel larger and then the lateral deflection as a pillow's buckling appeared to be easily generated. Hence, the case of hf < 20 mm was recognized as the in-plane end-crush mode, while the case of hf > 20 mm behaved as the lateral deflection mode when considering the dipping of instant adhesives.

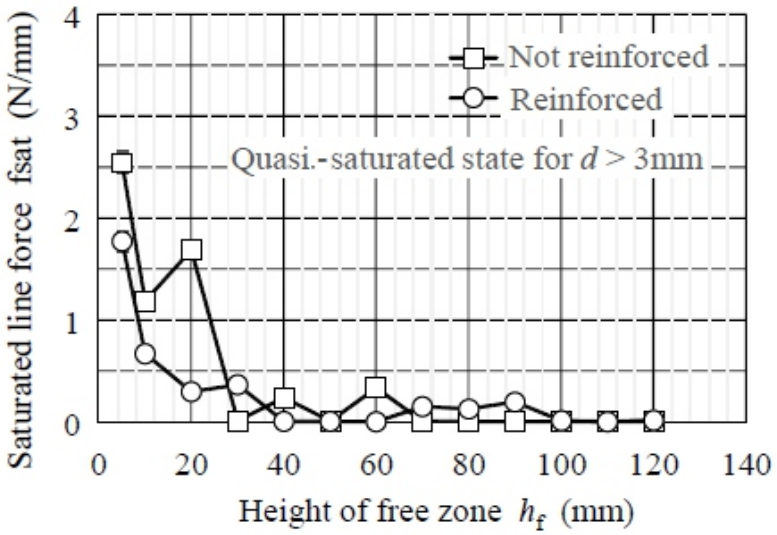

Figure 12. Quashi-saturated line force derived from Figures 9 and 11.

Figure 13 shows the relationship between the peak maximum line force fp and the height of free zone hf. Since there were sometimes multiple peaks of the line force in a range of compressive displacement 8 mm when the instant adhesives were not dipped on the both ends, the first peak was additionally picked up when the peak maximum was detected after the first peak occurrence. In Figure 9, the case of hf = 30 mm was a representative response which included several peaks. Herein, the lateral deflection was not detected at the first peak position (d < 1 mm) but that was a little observed at the secondary peak position (d ≈2mm) when h_f = 30mm.

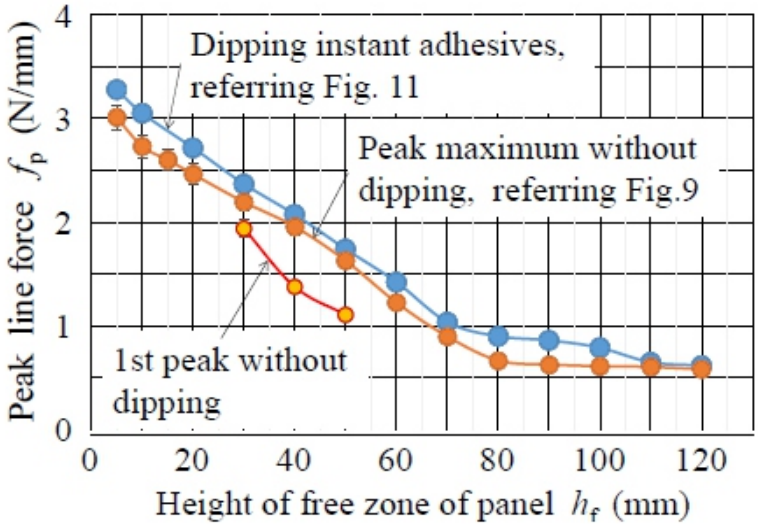

Figure 13. Dependency of peak maximum line force on height of free zone when w_{gs} = 3 mm.

Seeing Figure 13, the peak maximum of reinforced case was about 0.2–0.3 N/mm larger than that of non-reinforced case. This difference seemed to be caused from the crushing resistance of the both ends due to the dipping reinforcement of instant adhesives.

For the range of hf < 80 mm, as the peak maximum line force fp linearly decreased with hf, the following approximations Eqs 3 and 4 were derived by the least square method. Here, The values of R2 were the coefficient of determination with Eqs 3 and 4, respectively.

$$f_p = -0.0307\, h_f + 3.10 \text{ (non-reinforced for } 5 < h_f < 80 \text{ mm, } R^2 = 99.6\%) \quad (3)$$

$$f_p = -0.0323\, h_f + 3.375 \text{ (reinforced for } 5 < h_f < 80 \text{ mm, } R^2 = 99.6\%) \quad (4)$$

Figure 14 shows the critical buckling strength of the panel using the pillar's buckling theory Eq 2 and the values of bending stifness D of Table 2. The approximations of Eqs 3 and 4 were also plotted in this graph.

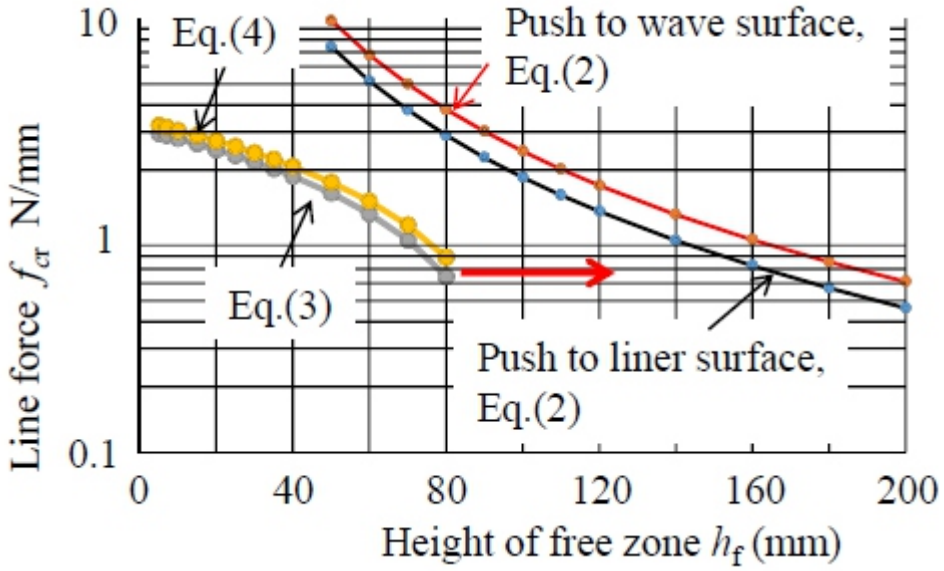

Figure 14. Calculated strength of Eulerian equation Eq 2 and experimental approximations.

Seeing Figure 14, as the gradient ∂ fp/ ∂ hf of Eqs 3 and 4 was almost equal to the results of Eq 2 for hf = 40–80 mm, the buckling behavior in this range appeared to be explained from the Eulerian equation of Eq 2, except for the absolute value of buckling strength. Its mismatching ratio was estimated as 4 times for hf = 40–80 mm. For the range of hf < 30 mm, the buckling behavior was understood as the edge crush mode (in-plane crushing or buldging of the panel without a lateral deflection). When increasing the height of the panel for hf = 80–120 mm, the decreasing of compressive strength fp was quite slow, or almost constant. Seeing Figure 8d and Figure 10d at d = 1 mm, the initial buckling seemed to be caused as a triangle bending of the panel at the clamped-end position of upper/lower grooves. This saturation of fp seems to be caused from the complexed mode such as a cylindrical-shell buckling [19] for hf = 80–120 mm, because the buckling strength was almost independent to the height of the panel.

3.3. Buckling directions of panel

The direction of lateral deflection of the panel is classified in two modes: (a) it moves from the liner to the wave side as shown in Figure 3(b-1), or (b) it moves from the wave to the liner side as Figure 3(b-2). From the results of three point bending test of GFSS and Table 2, since the bending stiffness of pushing the wave surface was 32% stronger than that of pushing the liner surface, the lateral deflection of the in-plane compressive test seemed to be eccentricly the pattern of Figure 3(b-1) direction. However, the results included two patterns of Figure 3(b-1) and (b-2). Figure 15 shows the occurrence distribution of buckling directions (Red: the deflection moved to the liner side or Blue: it moved to the wave side at the center zone of the panel). Seeing the experimental results, it was found that the initialization appeared to be affected by the reinforcement by the instant adhesives, while the pattern of Figure 3(b-2) (move to liner) apted to easily occur for hf > 60 mm. Considering the difference of bending stiffness with two

buckling directions and the triangle buckling of the panel at the early stage (d ≈ 1 mm), the initiation of the first buckling seemed to occur at the clamped-end position of the groove. Namely, if the pattern of Figure 3(b-1) occurs at the clamped-end position of the groove, then the central zone tends to move to the opposite side, to the liner side. On the other hand, if the pattern of Figure 3(b-1) occurs at the central zone, the mode was not changed. Hence, two patterns of buckling direction are possible, principally.

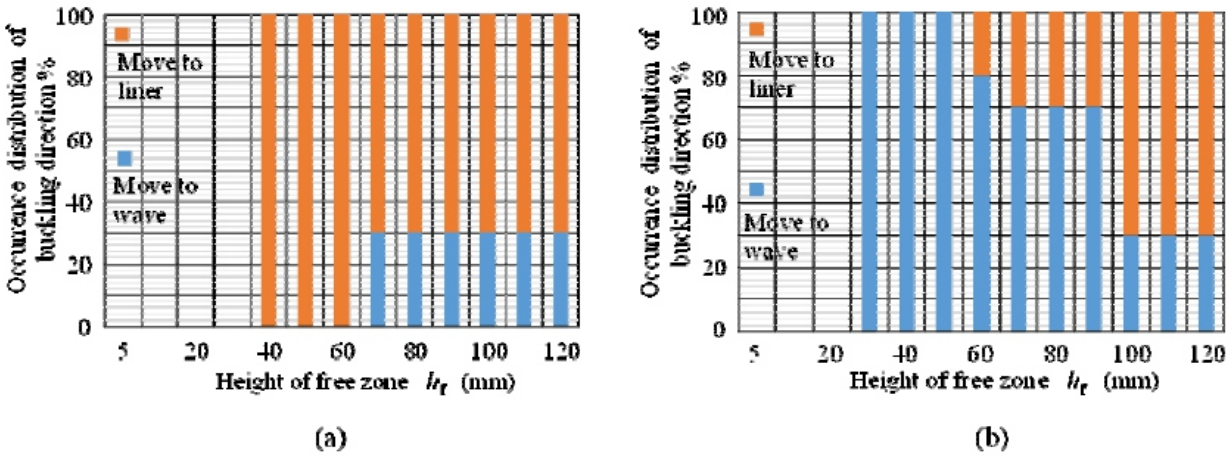

Figure 15. Occurrence distribution of buckling direction. (a) Not reinforced (without dipping instant adhesives); (b) Reinforced (dipping instant adhesives).

3.4. Effects of groove's width on the buckling strength

Since the freedom of rotation at the clamped-end position of the holder's groove seems to be important to determine the critical buckling strength of the panel, the width of the holder's groove wgS was varied from 3.0 mm up to 4.0 mm when the both ends of the panel was not reinforced by the instant adhesives.

Figure16 shows representative compression processes of the straight panel which had hf = 5, 20, 40, 80 mm and wgs = 4mm without dipping instant adhesives on the both ends. Figure 17 shows the relationship between the compressive line force f and the displacement of the upper edge holder d. when choosing wgS = 4 mm and hf = 10 mm without dipping instant adhesives on the both ends. Seeing Figure 16, the upper ends (and the lower ends) of the panel were crushed and clearly inclined in one side (left or right) at the groove zone, due to a 1mm-clearance between the groove's width and the panel's thickness. This inclination of the ends of the panel in the groove zone seems to cause some decreasing of the gradient $\partial f / \partial d$ at the early stage ($0 < d < 0.5$ mm). As the result, the peak maximum line force fp decreased with wgS, while the corresponded displacement dp apted to increase.

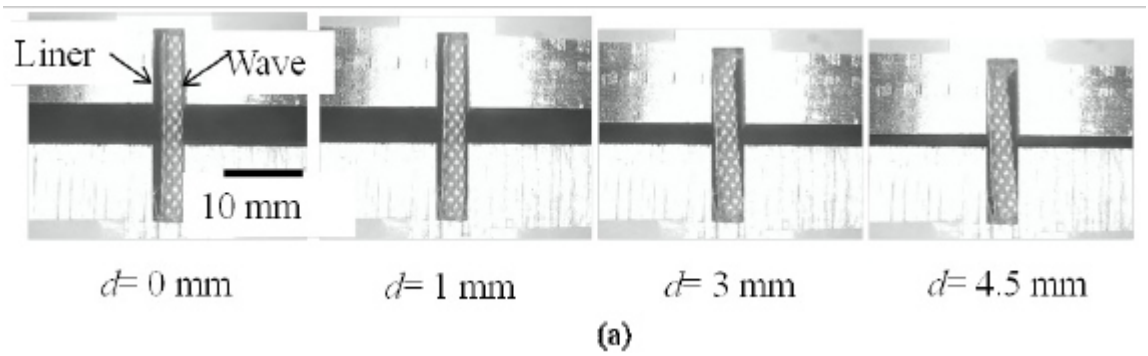

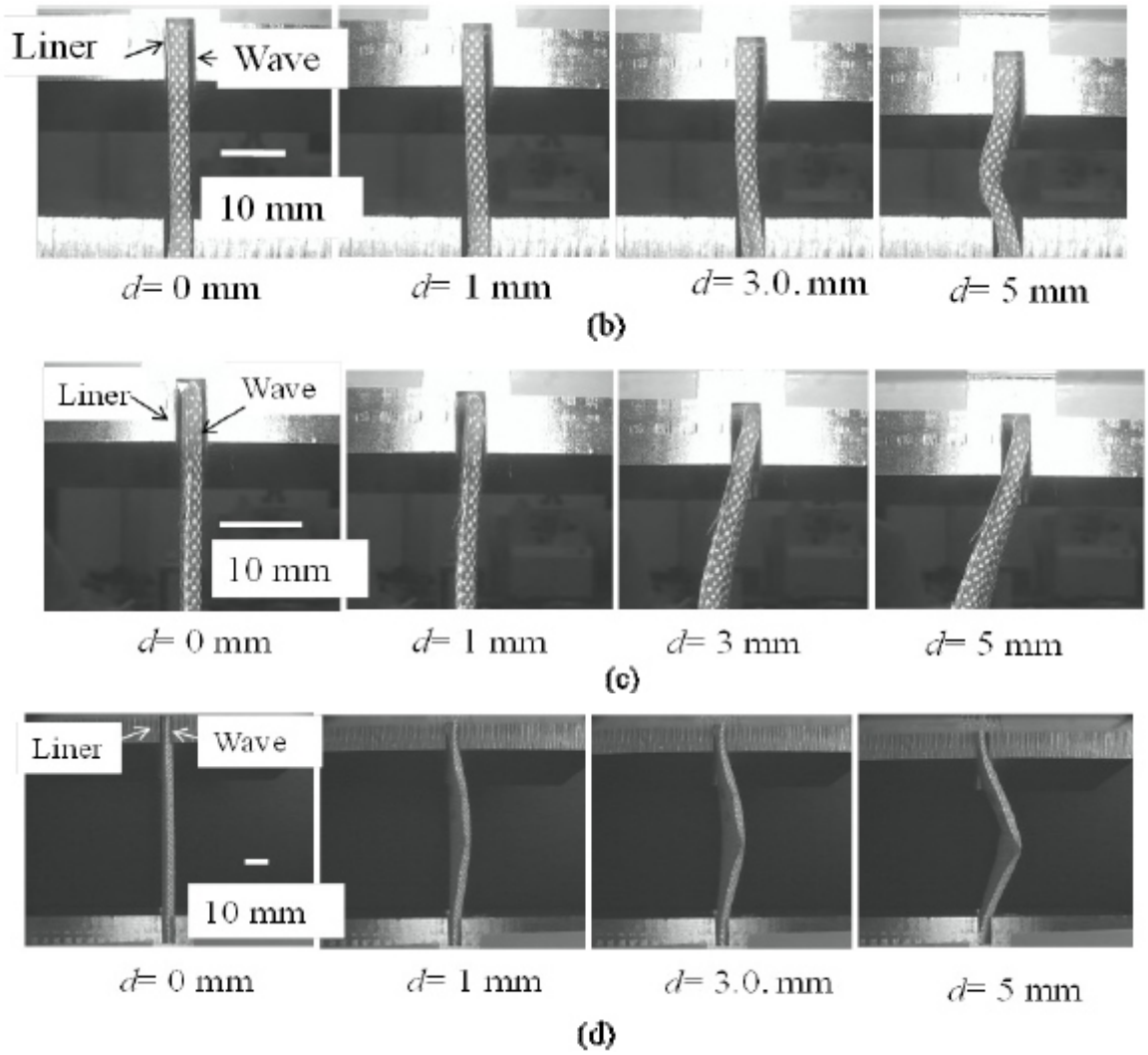

Figure 16. Deformation behavior of GFSS during in-plane compression at a width of groove wgs= 4 mm without dipping instant adhesives (not reinforced). (a) In a case of the height of free zone hf =5 mm, (b) In a case of the height of free zone hf =20 mm, (c) In a case of the height of free zone hf =40 mm, (d) In a case of the height of free zone hf =80 mm.

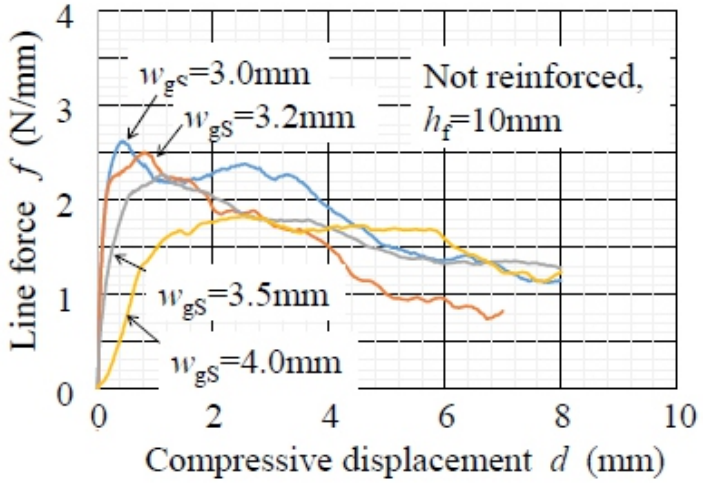

Figure 17. Load response diagram of compressive test of straight panel at hf = 10 mm under varying groove's width wgS without dipping instant adhesives (not reinforced).

Figure 18 shows the peak maximum line force for h_f = 5–80 mm. When h_f < 50 mm (=16.7h_0), f_p decreased with w_{gS}. Since this relationship between f_p and w_{gS} was similar for h_f < 50 mm, focusing on the case of h_f = 40 mm, a linear approximation of f_p with w_{gS} was derived from Figure 18, and its relation was shown as Eq 5. Herein, the dependency of f_p on w_{gS} disappeared for h_f > 70 mm.

$$f_p = 4.725 - 0.916\, w_{gS} \quad (\text{for } w_{gS} = 3\text{–}4 \text{ mm at } h_f = 40 \text{ mm}, R^2 = 98.9\%) \qquad (5)$$

Seeing the first peak without dipping in Figure 13, it disappeared for h_f > 60 mm. The dependency of f_p in Figure 18 also disappeared for h_f > 60 mm. Therefore, the buckling strength of the panel seems to be primarily determined by the height of panel hf, not by the local crushing condition of both ends of the panel in the holder's groove, when h_f > 60 mm.

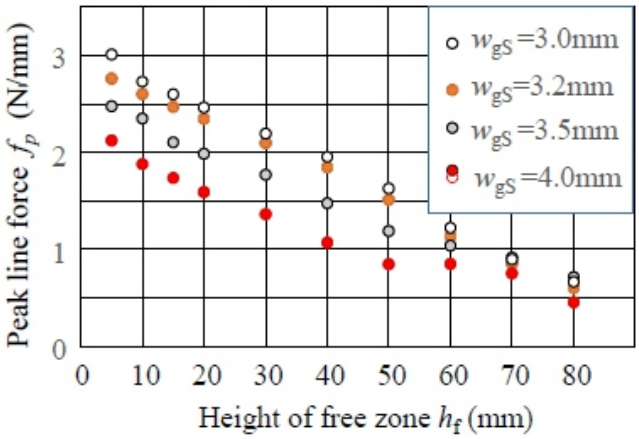

Figure 18. Dependency of peak maximum line force on width of holder's groove when both ends were not reinforced by instant adhesives.

4. CONCLUSIONS

To perform an in-plane compressive test of fragile glass fibre based single faced corrugated structure sheet (GFSS), and to reveal the buckling strengh of the straight panel of GFSS, a holding tool which has appropriate groove for supporting the panel in the perpendicular attitude was developed. To discuss the buckling strength under an in-plane-compressive loading of GFSS across the machine producing direction (along the flute's longitudinal direction), a three-point-bending flextural test of GFSS was preliminary carried out and a reinforced condition of the both ends of the panel was inspected by dipping a small volume of instant adhesives. Furthermore, to investigate the effects of clearance of the groove, several width of the groove were prepared for the experiment.

The revealed results were as follows:

(1) A plain panel of GFSS without dipping instant adhesives was locally crushed at the both ends of the panel in the holder's groove, while the panel reinforced by dipping the instant adhesives (liquid arone alpha) on the both ends stably resisted in the holder's groove and it had the higher strength of 0.2–0.3 N/mm when varying the height of free zone hf = 0.5–120 mm.

(2) Using the three-point-bending stiffness and the Eulerian piller's theory Eq 2, the critical buckling strength of the panel was estimated. The gradient of the buckling strength ∂ f_p/ ∂ hf with hf matched to the theoretical behavior for a certain range 40mm < h_f < 80mm.

(3) When h_f < 30 mm, the compressive deformation of the panel behaved as an end-crush and inplane bulging without any lateral deflection. The transition condition was almost estimated as 4– 10 times of the height (h_0= 3 mm) of GFSS.

(4) When choosing 120 mm > hf > 80 mm, the decreasing tendency of fp was changed (quite slow state), compared to the middle range 40 mm <hf < 80 mm.
(5) A local initiation of buckling was revealed at the clamping-end position of the holder's groove, and the lateral deflection profile of the panel behaved as a triangle-like folding of the panel when hf > 40 mm.
(6) The dependency of fp on the holder's width wgS almost disappeared for hf > 60mm.

ACKNOWLEDGMENTS

The authors thank Syotaro Takeda of KUBO corporation, for his assistance with preliminary experiments and preparing glass fiber based fabrics structural sheets.

CONFLICT OF INTEREST

All authors declare there is no conflict in this paper.

REFERENCES

1. Kubo corporation, Glass fibre based structural sheet, 2017. Available from: http://www.kuboco. net/.
2. Kirwan MJ (2013) Corrugated fiberboard packaging, Handbook of Paper and Paperboard Packaging Technology, 2 Eds., John Wiley & Sons, 313–321.
3. Jonson G (1999) Corrugated Board Packaging, 2 Eds., Leather head: Pira International, 145– 159.
4. Lubin G (1982) Characterization of corrugated board, Handbook of Composite, Springer, Boston, MA, 145–149.
5. Mark RE, Habeger C, Borch J, et al. (2002) Characterization of corrugated board, Handbook of Physical Testing of Paper, 2 Eds., CRC Press, 1: 571–574.
6. Twede D, Selke SM, Kamdem D, et al. (2015) Single face, Cartons, Crafts and Corrugated Board: Handbook of Paper and Wood Packaging Technology, DEStech publication, 460–464.
7. Twede D, Selke SEM, Kamdem D, et al. (2015) Cartons, Crafts and Corrugated Board: Handbook of Paper and Wood Packaging Technology, DEStech publication, 250–252.
8. Bronkhorst CA, Keith AB (2002) Deformation and failure behaviour of paper (Edge wise crush test), In: Mark RE, Habeger C, Borch J, et al., Handbook of Physical Testing of Paper, 2 Eds., CRC Press, 1: 401–409.
9. Nagasawa S, Kudo H, Songtam L, et al. (2017) Tensile characteristics of glass fiber based single face board. Procedia Eng 207: 78–83.
10. Laosuwan S, Nagasawa S, Umemoto K (2020) Development of tensile fixture with corrugated structure sheet and estimation of tensile strength of glass fibre fabrics based single face corrugated structure sheet. AIMS Mater Sci 7: 75–92.
11. Matsushima S, Okuda T, Miyauchi O, et al. (1982) Strength of tensile deformation for corrugated fibre board. Japan TAPPI J 36: 377–387.
12. Wahab N, Arafah A, Fukuzawa Y et al. (2016) Estimation of corrugated cardboard strength using tensile test, In: MFB Abdollah, MAB Salim, TB Tuan, Proceeding of Mechanical Engineering Research Day 2016, Melaka: Centre for Advanced Research on Energy.
13. Cox HL (1952) The elasticity and strength of paper and other fibrous materials. Br J Appl Phys 3: 72–79.
14. T glass, Niitobo corporation, 2019. Available from: https://www.nittobo.co.jp/business/glassfibre/sp_material/t-glass.htm.
15. Loewenstein KL (1973) The Manufacturing Technology of Continuous Glass Fibres, 2–94, Elsevier Scientific.
16. Loewenstein KL (1975) The manufacture of continuous glass fibres. Platinum Met Rev 19: 84– 87
17. Popil RE (2017) Bending stiffness of corrugated board, Physical Testing of Paper, UK: Smithers Pira, 67–77.
18. Timoshenko S (1955) Elementary theory and problems, Strength of materials, 3 Eds., D. Van Nostrand Company, 252–266.
19. Mihara Y, Kobayashi T, Fujii F (2011) Postbuckling analyses of elastic cylinderical shells under axial compression. Trans JSME 77: 582–589.

·ISSN : 2372-0484

Cyclic Response of A Reinforced Concrete Frame: Comparison of Experimental Results with Different Hysteretic Models

Pedro Folhento[1], Manuel Braz-César[2] and Rui Barros[3,*]

[1] CONSTRUCT, Faculdade de Engenharia da Universidade do Porto (FEUP), PhD student at FEUP, Rua Dr. Roberto Frias, s/n 4200-465 Porto, Portugal

[2] CONSTRUCT-FEUP. Instituto Politécnico de Bragança-ESTiG, Campus de Santa Apolónia -5300-253 Bragança, Portugal

[3] CONSTRUCT, Faculdade de Engenharia da Universidade do Porto (FEUP), Department of Civil Engineering-Structural Division, Rua Dr. Roberto Frias, s/n 4200-465, Porto, Portugal

* Correspondence: Email: rcb@fe.up.pt.

ABSTRACT

An accurate hysteresis model is fundamental to well capture the non-linearity phenomena occurring in structural and non-structural elements in building structures, that are usually made of reinforced concrete or steel materials. In this sense, this paper aims to numerically estimate through simplified non-linear analyses, the cyclic response of a reinforced concrete frame using different hysteretic models present in the literature. A commercial Finite Element Method package is used to carry out most of the simulations using polygonal hysteretic models and a fiber model, and additionally, a MATLAB script is developed to use a smooth hysteresis model. The experimental data is based on the experiments carried out in the Laboratório Nacional de Engenharia Civil, Portugal. The numerical outcomes are further compared with the experimental result to evaluate the accuracy of the simplified analysis based on the lumped plasticity or plastic hinge method for the reinforced concrete bare frame. Results show that the tetralinear Takeda's model fits closely the experimental hysteresis loops. The fiber model can well capture the hysteresis behavior, though it requires knowledge and expertise on parameter calibration. Sivaselvan and Reinhorn's smooth hysteresis model was able to satisfactorily reproduce the actual non-linear cyclic behavior of the RC frame structure in a global way.

Keywords: cyclic response; reinforced concrete; non-linear analysis; hysteresis models; optimization

1. INTRODUCTION

Natural events, such as earthquakes, induce structural vibrations in building structures that can provoke permanent damage or even the collapse of the entire structural system. These negative consequences arise from the substantial floor's lateral deformation induced by moderate seismic events, being currently one of the main concerns in structural design. Hence, some level of damage is expected and may be purposely lumped at pre-determined locations, i.e., plastic hinges, to dissipate energy through inelastic deformation, preventing global collapse by holding the main structural elements, viz. the columns, during the seismic event, and thus not compromising the structure's stability.

Moderate to severe earthquakes can compromise the structural and seismic performance of structures, causing significant and unexpected damage to the structural and non-structural elements, which can further lead to the collapse of buildings or part of these as observed during recent events [1,2]. A large number of studies have been carried out by different investigators to assess the non-linear cyclic behavior of reinforced concrete framed structures under different conditions and to validate the respective results with experimental data [3–6]. Experimental tests in this context, allow for the

development of numerical models that should be capable of replicating the real behavior of a structure under cyclic loading with reasonable accuracy. Hence, permitting further studies and leading to valuable conclusions about such behavior.

To assess the level of damage experienced by structural elements, e.g., beams and columns in moment-resisting frames, hysteresis models can be used to represent the corresponding constitutive relationships at the critical sections (usually at the extremities of the structural elements). Hysteresis is associated with the rate-independence effect and the memory nature of inelastic behavior in which the restoring force depends on the instantaneous deformation and the previous history of the deformation [7]. Thus, different hysteresis models are present in the literature to emulate the physical behavior of distinct structural or non-structural elements, materials, or structural systems, under cyclic loading. These models are broadly categorized into polygonal and smooth hysteresis models [8], and can be developed for a specific purpose or can be more versatile. Nowadays, versatile hysteresis models are often developed rather than for specific purposes, exhibiting degradation features, such as stiffness degradation, strength deterioration, and the pinching effect.

The main purpose of this work is then to validate a set of simplified nonlinear models used to carry out a material nonlinear analysis.

2. EXPERIMENTAL RESULTS

The experimental campaign performed at LNEC [9] aimed to study the cyclic response of reinforced concrete (RC) bare frames and with masonry infill walls. Figure 1a presents a sketch of the general description of the RC bare frame, which is loaded at each column with a constant vertical load of 100 kN and is subjected to an increasing cyclical load/displacement pattern at the beam's level, obeying the law of displacements in Figure 1b. The bare frame structure is made of concrete C20/25, longitudinal steel reinforcement of S400, and transverse reinforcement (stirrups) of S500. At the critical location (plastic hinges), near the end of each structural member, accurate concrete confinement is guaranteed by tightening the spacing between the stirrups as can be observed in Figure 2.

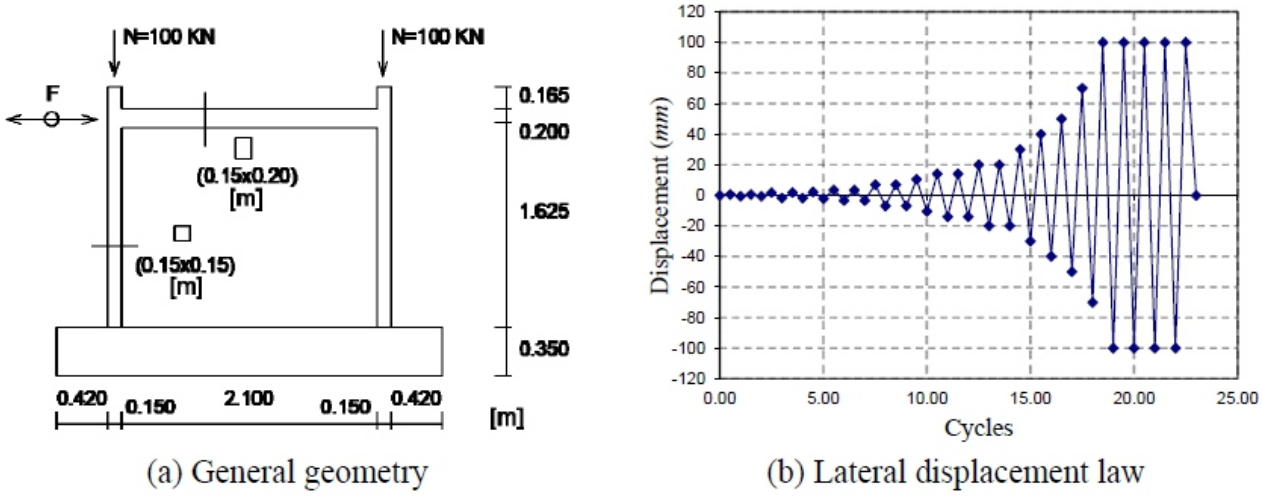

(a) General geometry (b) Lateral displacement law

Figure 1. Experimental frame and loading pattern [10].

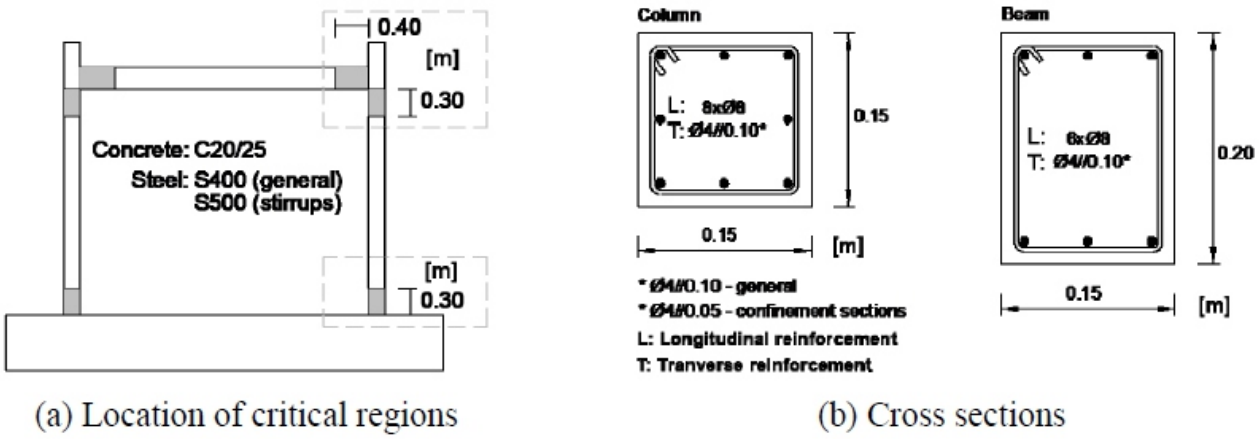

Figure 2. RC frame confinement of the critical regions [10].

Figure 3 shows the cyclic response of the RC bare frame. A smooth evolution is observed with a resulting maximum before the complete concrete cracking at the top and bottom ends of the columns. Subsequently, a soft stiffness decrease occurs without collapse, although with substantial damage and inelastic hinge spread in the columns.

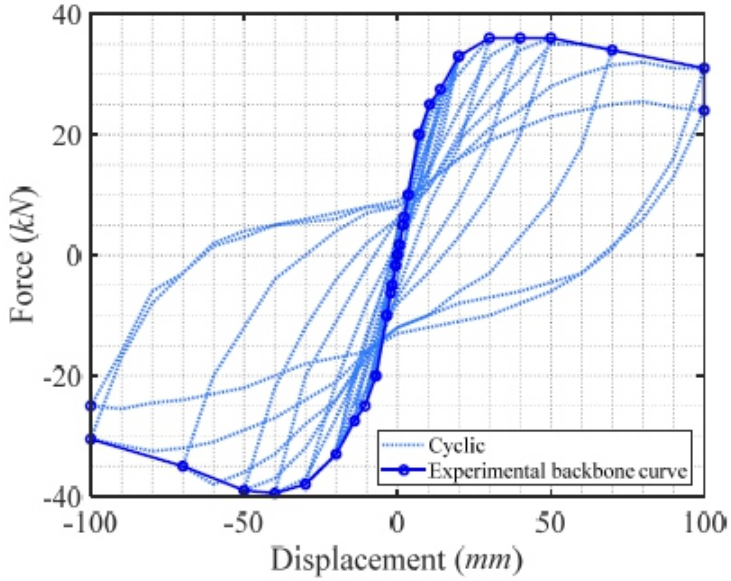

Figure 3. Experimental cyclic response and corresponding backbone curve of the RC frame structure.

3. NUMERICAL RESULTS AND DISCUSSION

The performance of different hysteresis models will be assessed, attempting to emulate the cyclic behavior of the RC frame structure, whose experimental result is presented in Figure 3.

The inelastic behavior of the frame structure is generally manifested by the formation of plastic hinges at the extremities of the elements as represented in Figure 4. This type of behavior that admits the concentration of plasticity at specific locations, allowed the creation of several simplified methodologies that enable the performance of simpler static or dynamic non-linear analysis [11].

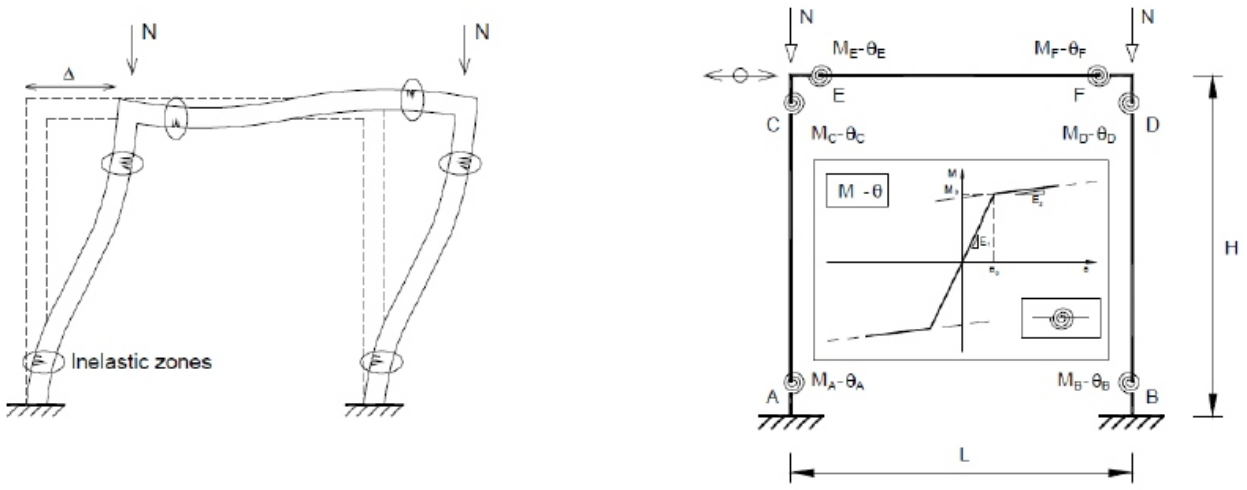

Figure 4. Critical zones of plastic hinges formation [10].

3.1. Simplified non-linear analysis of bare frames

To begin the mentioned simplified procedure, the definition of the constitutive relations in terms of moment-curvature of the columns and beam's sections must be derived, presented in Figure 5.

These will be important in the definition of the different initial levels of the structure's stiffness during cyclic loading.

This study considers two different methods to obtain the non-linear cyclic behavior of RC frame structures [12], viz., Plastic Hinge Model (PHM) and Fiber Model (FM). The key difference between the two models lies in the way the constitutive laws are defined and used. In the hinge models, an envelope curve is defined to represent the global behavior of the complete cross-section in terms of moment-curvature; the FM requires the establishment of constitutive laws associated with the axial deformation of each of the materials (or fibers) that comprise the section. The modeling of the plastic hinges in the PHM is carried out by including a zero-length element linking two adjacent beam elements, in which a constitutive law must be defined for each degree of freedom considered. A third way to analyze the non-linear cyclic behavior of the RC frame structure may be the use of a versatile hysteresis model, capable of modeling the respective behavior of the structural system in a global or macro way. This can be achieved by the proper optimization and calibration of the parameters defining the hysteresis model.

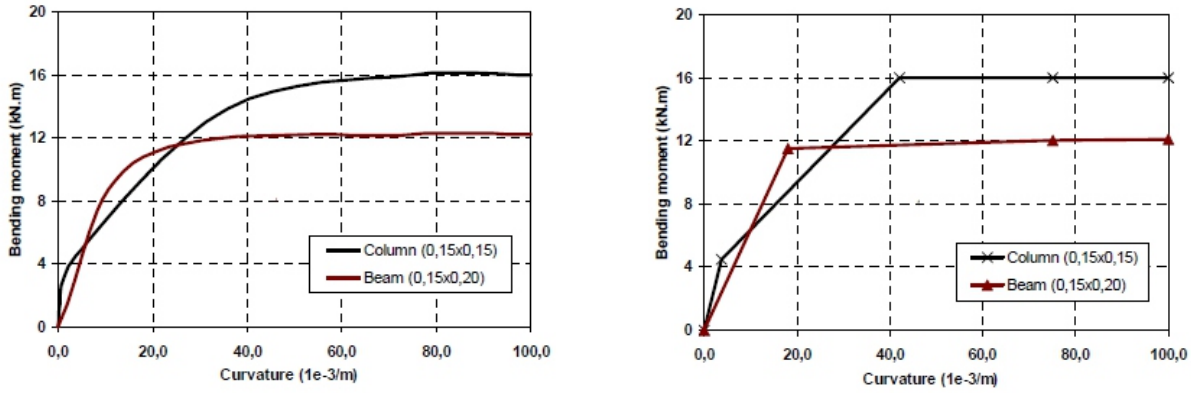

(a) Numerical (b) Ideal

Figure 5. Moment-curvature relationships for the columns and beam [10].

Hence, a Fiber model (FM) and four hysteresis models, i.e., three polygonal hysteresis models (Clough's model [13], trilinear Takeda's model [14], and tetralinear Takeda's model [15])—used as zero-length elements, and a smooth hysteresis model (Sivaselvan and Reinhorn's model [8])—used to analyze the global non-linear cyclic behavior; will be used and compared to the experimental response to assess the capability to model the non-linear cyclic behavior of RC bare frame structures.

The polygonal hysteresis models and the fiber model were carried out using the software Midas-Civil [15], and the smooth hysteresis model was developed using a MATLAB [16] script.

Table 1 presents the initial and reduced bending stiffness values of the different backbone curves of the polygonal hysteresis models, to be introduced in the next sections using the mentioned software.

Table 1. Bending stiffness levels according to the type of backbone curve admitted.

Structural element	Backbone curve	Bending stiffness (kN/m^2)			
		K_0	K_1	K_2	K_3
Columns	*Bilinear*	1380	6.9 (0.5%)		
	Trilinear		276 (20%)	6.9 (0.5%)	
	Tetralinear				−6.9 (−0.5%)
Beam	*Bilinear*	610	30.5 (5%)		
	Trilinear				
	Tetralinear				

The subsequent subsections present the models' outline or the representation of the hysteresis laws in generalized force-displacement relations, and the corresponding final iteration result that best fits the experimental results.

3.2. Clough's hysteresis model

Clough's model [13], one of the first hysteresis models, is based on the simplified constitutive law with a bilinear backbone curve as represented in Figure 6a and a formula that translates the stiffness reduction on unloading (KR), comprising an unloading stiffness parameter. The fitting to the experimental results is based on the values in Table 1 and on the variation of the parameter related to the unloading stiffness reduction (the value adopted for this parameter was 0.5).

This model does not represent the real cyclic behavior of the RC frame structure, since a substantial increase in the strength capacity is verified with the increase in lateral displacement, which is not consistent with the experimental results as proved by Figure 6b. This is mostly due to the bilinear backbone curve, which in reality is not associated with RC behavior due to concrete cracking.

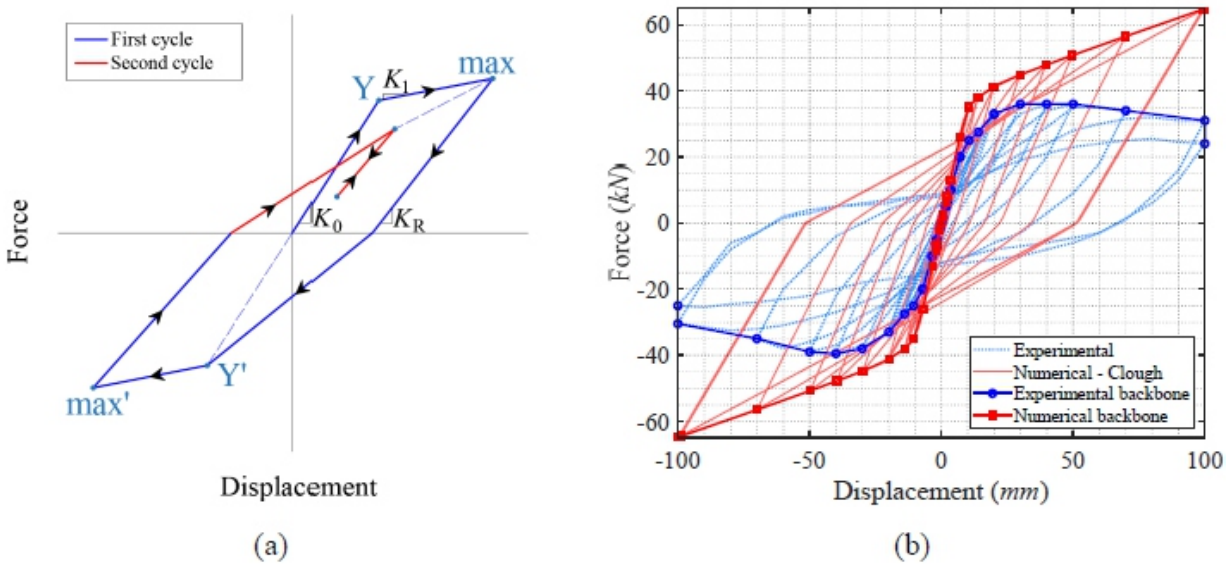

Figure 6. Clough's model. (a) Hinge model, (b) comparison of results.

3.3. Trilinear Takeda's hysteresis model

A trilinear backbone curve is more adequate to represent RC cyclic behavior. One example of a hysteresis model that considers a trilinear backbone curve and stiffness degradation in the unloading branches of the inner and outer loops is the trilinear Takeda's model [14]. Available in the software Midas-Civil and with the constitutive law represented in Figure 7a, the fitting of the experimental results with this model is based on the values in Table 1, and on the parameters that define the unloading stiffness in the corresponding branches of the cycles through the use of a formula (it was adopted for the input parameters in this formula 0.75 for the exponent in unloading stiffness calculation and 1.00 for the inner loop unloading stiffness calculation).

The trilinear Takeda's model can better predict the experimental results for smaller lateral displacements, compared with the previous model. However, much like the preceding model, it tends to overestimate the post-yielding stiffness, despite presenting a less pronounced increase (Figure 7b).

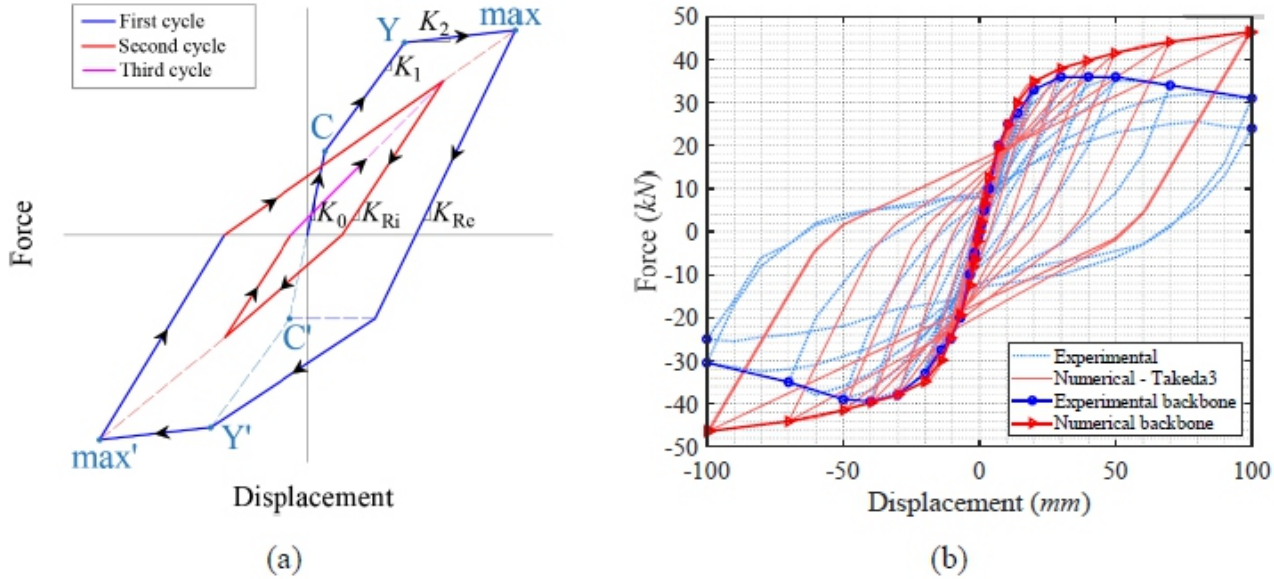

Figure 7. Takeda's trilinear model. (a) Hinge model, (b) comparison of results.

Hence, this model is unable to represent the negative stiffness verified immediately before unloading, resulting in an overestimation of the post-yielding stiffness.

3.4. Tetralinear Takeda's hysteresis model

To account for the drawbacks of the precedent hysteresis models, the tetralinear Takeda's model [15], shows a modification to the previous model that includes a fourth branch related to the negative stiffness on loading.

Following the typical relations presented in the ideal model in Figure 8a and the tabled values in Table 1, a close estimation of the experimental results can be obtained, as can be seen by Figure 8b. The fitting parameters (unloading stiffness parameters) used are the same as the previous version of the model, leading to a better approximation of the real cyclic behavior of the RC frame structure.

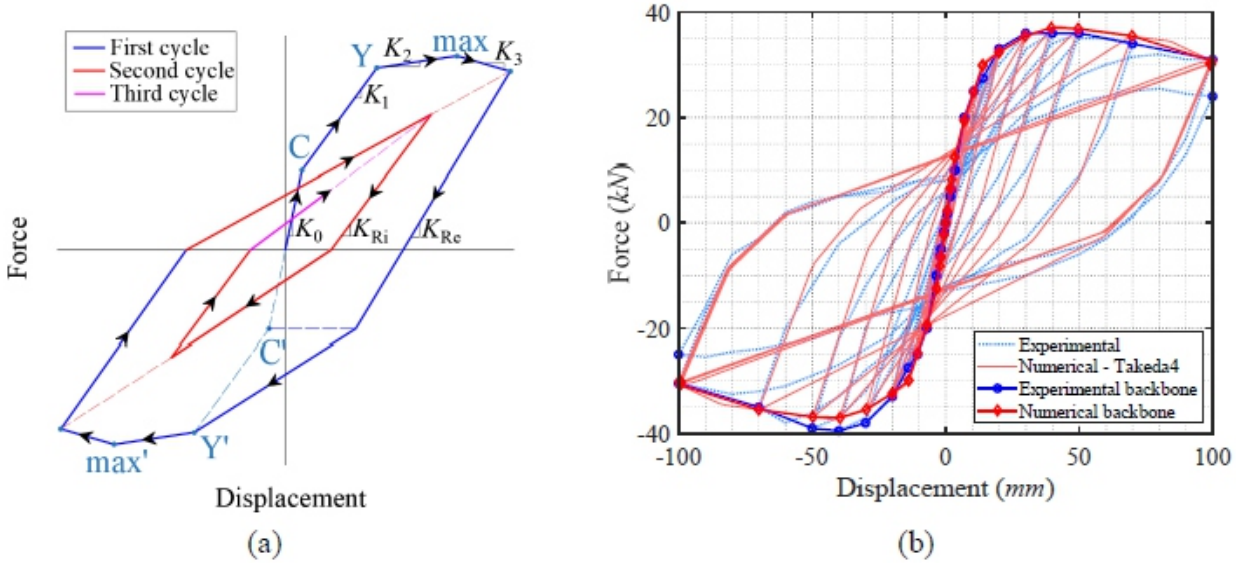

Figure 8. Takeda's tetralinear model. (a) Hinge model, (b) comparison of results.

3.5. Fiber model

The fiber model enables a localized analysis of the non-linear behavior of the frame structure, by discretizing the section of the structural elements into fibers that are associated with each material, whose behavior admits axial deformation only. Thus, the elementary constitutive laws are defined for each material that composes the section instead of a global curve for the entire section [17], further leading to a global constitutive law through the application of an increasing moment/rotation.

The fiber model in Midas-Civil considers that the section remains plane throughout deformation, and perpendicular to the neutral axis, and consequently the reinforcement slippage is not considered. The state of each fiber is assessed through axial and flexural deformations. The axial forces and bending moments are computed based on the level of stress of each fiber, and thus the properties of the section's non-linear behavior are defined by a stress-strain relation of the fibers that compose the section.

The fiber model can effectively represent the non-linear behavior of frame structures, being able to trace the moment-curvature relation of one section, monitoring the neutral axis depth, obtaining the axial force of each fiber, and computing the spread or extension of the plastic hinge. On the other hand, it may be laborious in the subdivision of the respective sections in fibers to which are associated the elementary

constitutive laws, and the constitutive laws have to adequately represent the real behavior of each material, otherwise, the model may not adequately represent the global law of the section under study. In addition, the common uniaxial compressive tests carried out to characterize the behavior of concrete may not adequately estimate the behavior of this material, since concrete's confinement plays an important role in its strength capacity, which becomes more relevant in the case of cyclic loading. Hence, the parameters that characterize the materials were chosen according to the experimental tests, except for concrete, for which different values of confinement were adopted to better fit the experimental results (based on the percentage of transversal reinforcement).

For the current study, the Magenotto-pinto steel model and the Kent and Park concrete model [18], both available in Midas-Civil, were used. The discretization of the beam and columns' critical sections is presented in Figure 9a. It should be referred that the experimental model had a loading device that limited the deformation of the beam during testing, and thus the beam may be in the linear elastic regime. Hence, it is also assumed that the non-linear behavior is lumped at the columns' ends only.

After performing the non-linear analysis of the frame using the fiber model, it was verified that it can provide a good estimate of the experimental model behavior (Figure 9b). The numerical hysteretic curves are found to be very close to the experimental results. However, this model presents some limitations associated with the materials' constitutive laws, being more suitable for moderate lateral displacements and analysis of not only the global behavior but the behavior at the section's level that can calibrate models such as the ones presented in this paper, i.e., polygonal and smooth hysteresis models.

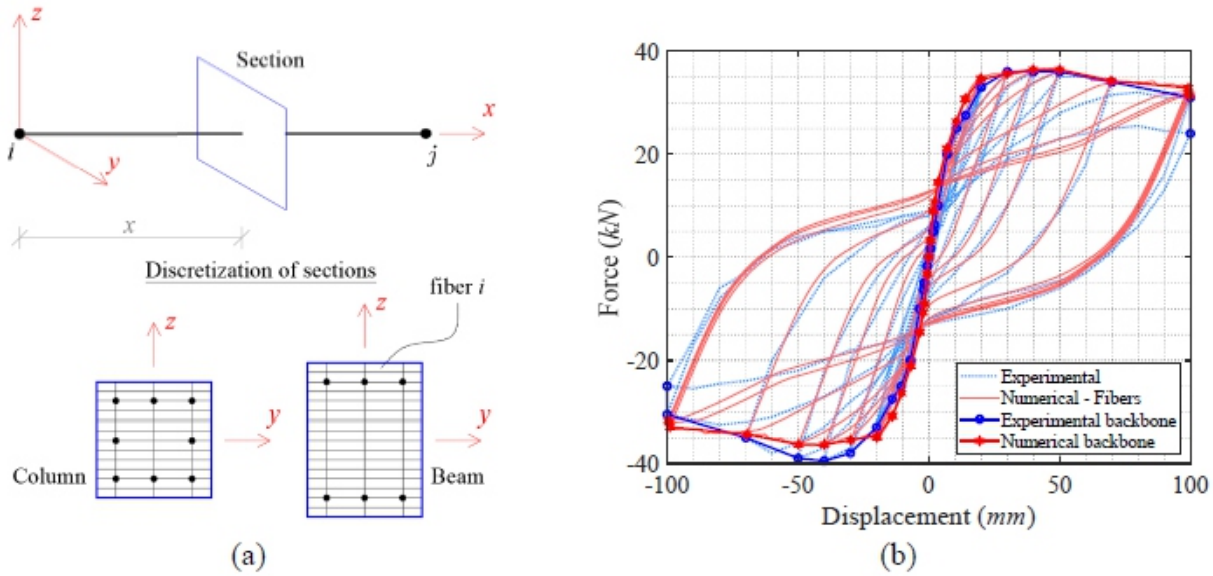

Figure 9. Fiber model. (a) Element's sections discretization used, (b) comparison of results. 3.6. Sivaselvan and Reinhorn's hysteresis model

A different model was used in an attempt to replicate the non-linear behavior of the RC frame structure. This model is a smooth hysteresis model developed by Sivaselvan and Reinhorn [8] and is a subsequent modification of the original Bouc-Wen model [19–21]. A schematic representation of this model is presented in Figure 10a, comprising three springs in combination, being able to simulate different behaviors of a structural system under cyclic loading, viz., strength hardening, the Bauschinger effect, asymmetrical yielding, stiffness and strength degradation, and the pinching effect.

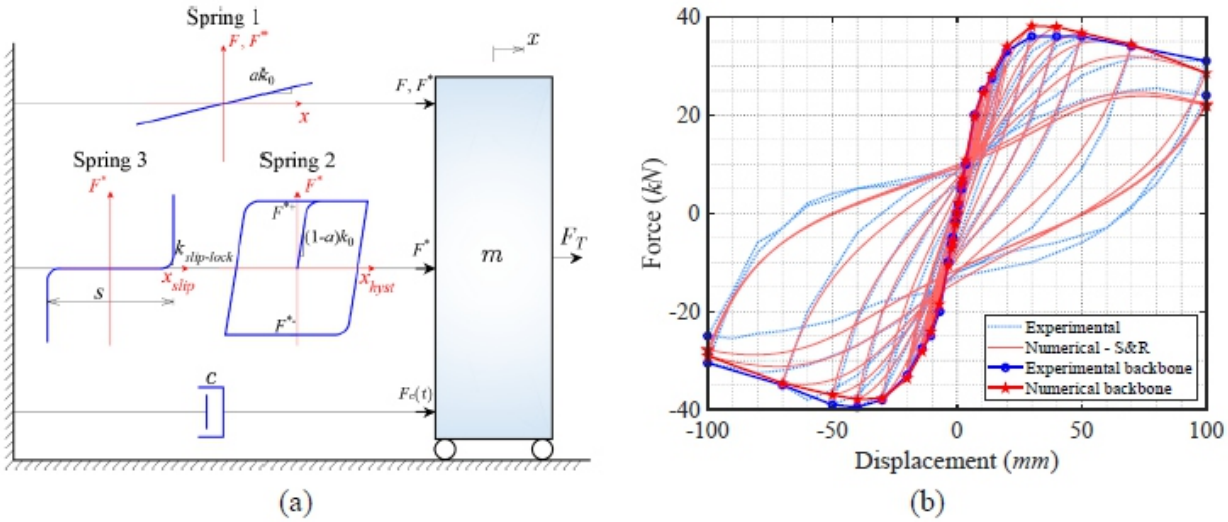

Figure 10. Sivaselvan and Reinhorn's smooth hysteresis model. (a) Hinge model, (b) comparison of results.

This model presents versatility and thus can represent the non-linear behavior of different structural systems and different materials, provided that the respective parameters are adequately chosen. In the present study, the model is used to simulate the global non-linear behavior of the frame structure as a single-degree-of-freedom (SDOF), rather than considering plastic hinges in the critical locations, thus creating a global stiffness matrix of the structure.

An algorithm was developed in MATLAB to use the aforementioned model in the corresponding conditions. The differential equation that computes the hysteretic force is given in rate-dependent form as follows [8],

$$\dot{F}^* = k_{hyst}\dot{x} \Leftrightarrow \dot{F}^* = \dot{x}\left(R_K - a\right)k_0\left\{1 - \left|\frac{F^*}{F_Y^*}\right|^{n_W}\left[\eta_1 sgn\left(F^*\dot{x}\right) + \eta_2\right]\right\} \quad (1)$$

$$k_H = \frac{k_{hyst}k_{slip\text{-}lock}}{k_{hyst} + k_{slip\text{-}lock}} \quad (2)$$

where F* and F^*_Y are the hysteretic force and corresponding yielding force, x is the displacement, k_0 is the initial elastic stiffness, kH is the total non-linear stiffness, k_{hyst} is the hysteretic stiffness, $k_{slip\text{-}lock}$ is the slip-lock stiffness accounting for pinching (related with the pinching parameters: Rs, σ, and λ), R_K is the parameter related with stiffness degradation (that is regulated by parameter α), a is the post-yield to initial stiffness ratio, n_W is the parameter controlling the smoothness transition from the elastic to the post-yielding range, and η_1 and η_2 are parameters controlling the shape of the unloading path (that can be reduced to one parameter, η, in substitution of η_1, provided that $\eta_1 + \eta_2 = 1 \leftrightarrow \eta_2 = 1 - \eta_1$, for compatibility with plasticity). In addition, strength degradation is controlled by parameters β1 and β2, being the latter related with energy demands and the former with ductility demands, and hence associated with the ultimate ductility factor, μult.

$$\frac{dF^*}{dt} = \frac{dx}{dt}(R_K - a)k_0\left\{1 - \left|\frac{F^*}{F_Y^*}\right|^{n_w}\left[\eta_1 sgn\left(F^*\frac{dx}{dt}\right) + \eta_2\right]\right\}$$
$$\Leftrightarrow dF^* = dx(R_K - a)k_0\left\{1 - \left|\frac{F^*}{F_Y^*}\right|^{n_w}\left[\eta_1 sgn\left(F^* dx\right) + \eta_2\right]\right\} \quad (3)$$

and the non-linear equation is solved using a numerical solver such as functions, fzero, fsolve, or vpasolve in MATLAB [16].

The optimization procedure was performed using the function fminsearch in MATLAB [16] that follows the Nelder-Mead simplex algorithm. To narrow down a large number of possibilities of an outcome, and find the optimal set of values for the mentioned parameters, a function called fminsearchbnd [22] was used. This function is based on the fminsearch algorithm, but with bound constraints applied to the variables. This function was used so to minimize the root mean square error (RMSE) between the predicted and experimental values of the restoring force. This error was further normalized (NRMSE) with the range of the experimental restoring force and converted to a percentage. Emphasis was also given to the points in the backbone curve by the calculation of the corresponding NRMSE and by assigning weighting factors to the referred errors. This will aid in the search for an optimal solution that can reasonably estimate the cyclic backbone curve.

To find the optimal values for the parameters defining the smooth hysteresis model that best fit the experimental results a procedure was followed according to the flowchart in Figure 11. The process began with the establishment of the boundary values for the parameters and the choice of an initial guess based on the characteristics of the experimental hysteretic loops. Manual calibration was then performed so to find a reasonable starting point for the use of function fminsearch/fminsearchbnd. If the comparison between the numerical and experimental data returns an NRMSE that is less than 5% and meets the stopping criteria (which were set so that the difference between two subsequent iterations on the calculation of the NRMSE is less than 1 × 10−4), the solution converged. If the solution converges, agreeing with the stopping criteria, the solution is saved and the process terminates.

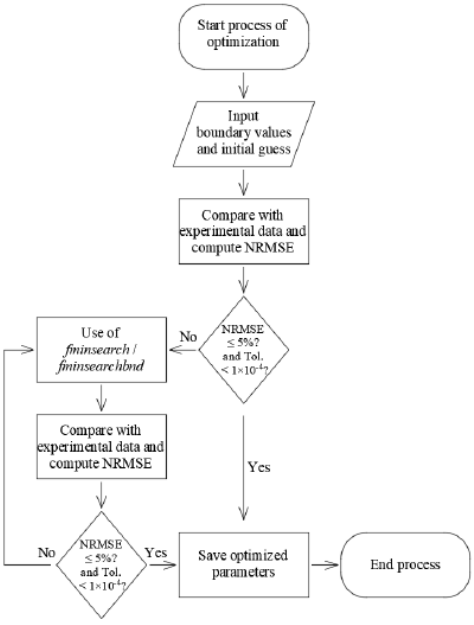

Figure 11. Flowchart of the optimization process used in the MATLAB script.

Within the variables considered, the initial stiffness and the yield force levels in both directions were also considered in the process of optimization, verifying that the optimum values are close to the actual values.

The result of the optimization procedure is presented in Figure 10b and the optimized parameters are: $n_W = 2.07$, $a = -0.061$, $\eta = 0.81$, $\alpha = 1.33$, $\beta_1 = 0.03$, $\beta_2 = 0.005$, $Rs = 0.17$, $\sigma = 0.40$, $\lambda = 0.004$, $k_0 = 3.567 \times 10^6$ N/m, $F^+_{Y0} = 4.8203 \times 10^4$ N, $F_{y0} = 4.9907 \times 10^4$ N, μ^+ ult = 7.85, μ- ult = 14.85. The model can satisfactorily predict the cyclic backbone curve as well as the overall hysteretic curves. It is seen that the model presents some deficiencies in predicting the unloading branches, the transitions from pre- to the post-yielding response of the experimental results, and the actual values of strength degradation.

3.7. Comparison of the dissipated hysteresis energy

To further compare the models considered in this study, the cumulated hysteresis energy dissipation is plotted in function of the cumulative displacement (Figure 12).

Clough's model presented the higher accumulated hysteresis energy dissipation, which is clearly due to the bigger hysteresis loops in Figure 6b. The tetralinear Takeda's model presents a better approximation to the experimental energy dissipation compared to Clough's and trilinear Takeda's model. The fiber model and Sivaselvan and Reinhorn's model presented the best approximations to the cumulative hysteresis energy dissipation, being the latter almost coincident. Although, Sivaselvan and Reinhorn's model was used to represent the non-linear hysteresis behavior of the RC frame in a global/macro way, and the fiber model requires knowledge of the constitutive relations of the materials involved and the parameters tunning may be very difficult.

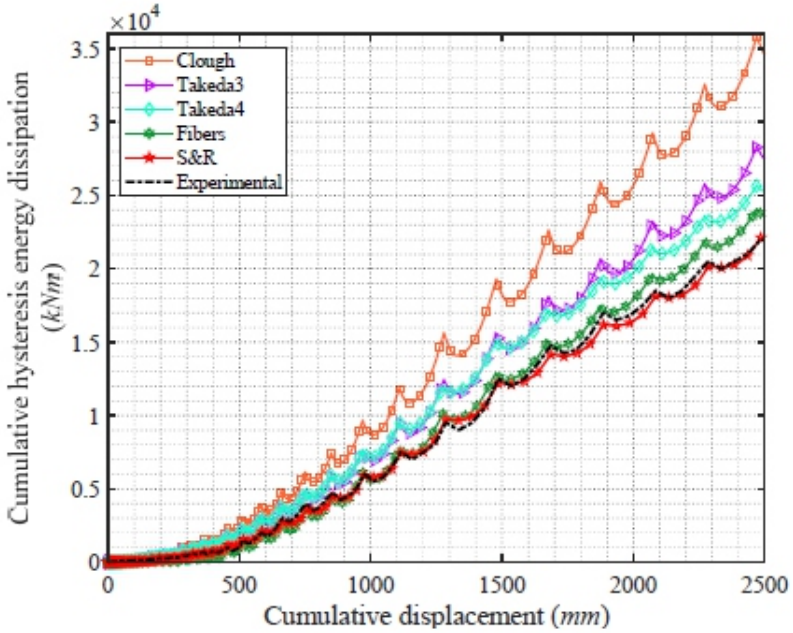

Figure 12. Comparison of the cumulative hysteresis energy dissipation.

4. CONCLUSIONS

This study reveals that the degree of numerical precision in replicating experimental results depends on the level of complexity associated with the constitutive models. It is possible to numerically represent the actual non-linear cyclic behavior of RC frame structures by the suitable selection of a hysteresis model.

Simplified analysis using polygonal hysteresis models to simulate the non-linear behavior at critical sections of structural elements may satisfactorily reproduce the experimental results, as was proven with tetralinear Takeda's model in the present case.

More complex and rigorous models, such as the fiber model, can lead to the best results in fitting the desired response. Nevertheless, the number of parameters involved, the required knowledge of the constitutive laws of the constituent materials, and increased computational demands might not compensate for the increased quality of the obtained results. It was also found that a versatile hysteresis model, emulating the global non-linear cyclic behavior of the RC frame structure, can provide great estimates of the experimental results, provided that a correct selection of the respective parameters is made. Although, this type of model might not be available in commercial software, requiring the prior development and adaptation of algorithms for specific purposes.

Further studies will address validation with more experimental data comprising different hysteretic configurations, and the consideration of non-structural elements within the RC frame structure.

ACKNOWLEDGMENTS

This paper is within the scope of the first author's Ph.D. degree in progress, financially supported by the Portuguese Foundation for Science and Technology (FCT) through the PhD grant reference SFRH/BD/139570/2018 under the programme POCH (N2020-P2020) and subsidized by the European Social Fund (FSE) and national funds from MCTES. This work was financially supported by: Base Funding-UIDB/04708/2020 of the CONSTRUCT-Instituto de I&D em Estruturas e Construções-funded by national funds through the FCT/MCTES (PIDDAC).

CONFLICT OF INTEREST

There is no conflict of interests with the authors and the publication of this paper.

REFERENCES

1. *Belleri A, Brunesi E, Nascimbene R, et al. (2015) Seismic performance of precast industrial facilities following major earthquakes in the Italian territory. J Perform Constru Fac 29: 04014135.*
2. *Perrone D, Calvi P, Nascimbene R, et al. (2019) Seismic performance of non-structural elements during the 2016 central Italy earthquake. B Earthq Eng 17: 5655–5677.*
3. *Brunesi E, Peloso S, Pinho R, et al. (2018) Cyclic testing of a full-scale two-storey reinforced precast concrete wall-slab-wall structure. B Earthq Eng 16: 5309–5339.*
4. *Bianchi F, Nascimbene R, Pavese A (2017) Experimental vs. numerical aimulations: Seismic response of a half scale three-storey infilled RC building strengthened using FRP retrofit. TOCEJ 11: 1158–1169.*
5. *Nascimbene R (2015) Numerical model of a reinforced concrete building: Earthquake analysis and experimental validation. Period Polytech-Civ 59: 521–530.*
6. *Rahnavard R, Rebelo C, Hélder C, et al. (2020) Numerical investigation of the cyclic performance of reinforced concrete frames equipped with a combination of a rubber core and a U-shaped metallic damper. Eng Struct 225: 111307.*
7. *Visintin A (1994) Differential Models of Hysteresis, Germany: Springer-Verlag.*
8. *Sivaselvan M, Reinhorn A (2000) Hysteretic models for deteriorating inelastic structures. J Eng Mech 126: 633–640.*
9. *Pires F (1990) Influência das paredes de alvenaria no comportamento de estruturas reticuladas de betão armado sujeitas a acções horizontais [PhD Thesis]. LNEC, Lisboa.*
10. *Braz-César M, Oliveira D, Barros R (2008) Comparison of cyclic response of reinforced concrete infilled frames with experimental results. The 14th World Conference on Earthquake Engineering, Beijing, China.*
11. *Fardis M, Panagiotakos T (1997) Seismic design and response of bare and masonry-infilled reinforced concrete buildings. Part I: Bare structures. J Earthq Eng 1: 219–256.*

12. *Paulay T, Priestley MJN (1992) Seismic Design of Reinforced Concrete and Masonry Buildings, New York: John Wiley & Sons.*
13. *Clough RW (1966) Effects of stiffness degradation on earthquake ductility requirement. UCB/SESM 1966/16, University of California, Berkeley, USA.*
14. *Takeda T, Sozen MA, Nielsen NN (1971) Reinforced concrete response to simulated earthquakes. OHBAYASHI-GUMI Technical Research Report 5, Tokyo, Japan.*
15. *Midas Inc. (2004) Analysis manual: Inelastic time history analysis, Korea.*
16. *Natick, Massachusetts, MATLAB R2019a 9.6.0.1072779, USA: The MathWorks, Inc.*
17. *Deng H, Chang Y, Lau D, et al. (2003) A simplified approach for nonlinear response analysis of composite structural members. International Workshop on Steel and Concrete Composite Constructions NCREE, Taiwan, 207–216.*
18. *Kent D, Park T (1971) Flexural members with confined concrete. J Struct Div 97: 1969–1990. 19. Bouc R (1968) Forced vibration of mechanical systems with hysteresis, In: Rupakhety R, Olafsson S, Bessaon B, Proceedings of the Fourth Conference on Non-linear Oscillation, Prague: Academia.*
20. *Wen Y (1976) Method for random vibration of hysteretic systems. J Eng Mech-ASCE 102: 249–263.*
21. *Wen Y (1980) Equivalent linearization for hysteretic system under random excitation. J Appl Mech 47: 150–154.*
22. *D'Errico J (2021) fminsearchbnd, fminsearchcon. Available from: https://www.mathworks.com/matlabcentral/fileexchange/8277-fminsearchbnd-fminsearchcon.*

·ISSN : 2372-0484

Parametric Study on A Bouc- Wen Model with Degradation Features for the Study of Cyclic Behavior of A Reinforced Concrete Frame

Pedro Folhento[1], Rui Barros[2] and Manuel Braz-Césa[3,*]

[1] CONSTRUCT, Faculdade de Engenharia da Universidade do Porto (FEUP), PhD student at FEUP, Rua Dr. Roberto Frias, s/n 4200-465 Porto, Portugal

[2] CONSTRUCT, Faculdade de Engenharia da Universidade do Porto (FEUP), Department of Civil Engineering-Structural Division, Rua Dr. Roberto Frias, s/n 4200-465, Porto, Portugal

[3] CONSTRUCT, FEUP. Instituto Politécnico de Bragança-ESTiG, Campus de Santa Apolónia- 5300-253 Bragança, Portugal

* Correspondence: Email: brazcesar@ipb.pt.

ABSTRACT

Non-linear behavior in building frame structures is inevitable and expected in moderate to severe seismic events. This behavior tends to be concentrated at the ends of beams and columns of moment-resisting frames. These critical regions, where plastic hinges form, are important for the global stability of the structural system. Depending on the available ductility, these mechanisms are responsible for the permanent deformations that the structure undergoes, leaving the remaining parts of the structural elements in the elastic regime, and hence in the safe zone. The importance of these mechanisms led to the search for an adequate model capable of well-capturing the non-linearity phenomena involved. The development of versatile hysteresis models with degradation features has been the aim of different studies. Hence, this paper presents a parametric study based on a smooth hysteresis model, a further modification to the well-known Bouc-Wen model, developed by Sivaselvan and Reinhorn, with a physical interpretation appropriate to the study of the non-linear behavior of civil engineering structures, particularly, building structures. Furthermore, an optimization procedure is implemented to calibrate the mentioned model's parameters, attempting to replicate the actual cyclic response of a reinforced concrete frame structure. The effect of each parameter in the hysteresis response will help on the understanding and on the possibilities of this kind of model in simulating different types of structural systems or different materials.

Keywords: hysteresis models; parametric study; non-linear behavior; cyclic response; optimization

1. INTRODUCTION

Nonlinearities of hysteresis are present in several phenomena of science and technology, such as physics (e.g. plasticity, friction, ferromagnetism, ferroelectricity, superconductivity, adsorption, and desorption, etc.), chemistry, biology, mechanics, even economics and experimental psychology, but particularly in the present scope, in civil engineering [1,2].

According to Visintin [2], hysteresis is regarded as a rate-independent memory effect. Rate independence requires that the couple (input and output) is invariant to any increasing time homeomorphism, meaning that at any instant of time, the output only depends on the range of the restriction of the input and on the order in which values have been attained, being independent of the derivatives of the input, which may even fail to exist. Hysteresis is then a phenomenological concept that is based on experimental data relating to the aforementioned couple.

In reality, the response of structural systems depends always on the rate of the applied load, and when this needs to be considered, viscosity will be introduced. Although generally in seismic response of structures viscosity and hysteresis contribute to the overall energy dissipated by the structure, if the load is applied at a very low rate, the viscosity phenomena can be neglected [3].

Hysteresis models represent constitutive relationships of a structural system or element. These represent a relationship between a couple of two physical quantities, that in the present scope can be resistance-deformation or stress-strain, shear-distortion, force-displacement, and moment-curvature. More realistic hysteresis models are essential to accurately characterize an inelastic response analysis of a structural system subjected to dynamic loads, such as seismic excitations.

Several hysteresis models were created and studied over the years. These models were developed based on how a certain structural system composed of a certain material behaves under lateral cyclic loading. The characterization of the mechanical non-linear behavior of structural components, e.g., structural elements and connections, and the assessment of the seismic response of structural systems (moment frames, braced frames, and shear and masonry walls) constitute the main purpose in the development of these hysteresis models [4].

The non-linear or inelastic behavior that a structural system exhibits when subjected to a dynamic excitation, can be simulated using a special kind of hysteresis model, an empirical hysteresis model. This kind of model, as the name suggests, is based on a phenomenological approach. The hysteresis characteristics observed in experimental tests of a certain structural system are idealized in a hysteresis model capable of expressing the resistance-deformation relations under any loading history with load reversals [5].

The early models in this context were mainly developed based on experimental observations of reinforced concrete (RC) and steel structural members' behavior. The later and recent hysteresis models are focused on more versatile models capable of simulating different structural systems and different materials under diverse loading conditions. Recent works have presented model formulations capable of accurately simulating complex hysteretic phenomena in rate-independent mechanical systems and materials [6,7], and the complex hysteretic response of elastomeric isolation bearings for seismic isolation [8]. Other studies have presented hysteretic models capable of reproducing damage of structural systems and components presenting stiffness and strength degradation [9,10].

Depending on the loading conditions of a structural member, its behavior can be dominated by flexure, shear, or axial deformation. The interaction between these behaviors can be complex and must be taken into account to obtain more reliable simulations.

These models can be generally divided into two types, polygonal hysteresis models (PHMs) and smooth hysteresis models (SHMs) [11].

The PHMs are based on piecewise linear behavior and driven by real behavioral stages of an element or structure, such as initial or elastic, cracking, yielding, stiffness and strength degradation stages, and crack and gap closures [11]. Many PHMs were developed over the years mostly to simulate the flexure-dominance behavior of structural members (e.g. elastic-perfectly-plastic bilinear model, strength-hardening bilinear model, Clough's model [12], degrading bilinear model [13], modified Clough's

model [14], trilinear degrading model [15], Takeda's model [16,17]. Additionally, to account for shear interaction other models have been developed simulating the pinching effect (e.g. slip-type Takeda's model [18], Kabeyasawa et al. model [19], Three-parameter model [20], Costa and Costa model [21], Rodrigues et al. [22].

Smooth hysteresis models present continuous stiffness changes due to yielding but with sharp changes due to unloading and deteriorating behavior [11]. Different SHMs were developed over the years, although the most popular ones are the Bouc-Wen models, which are a set of models including the original and its further modifications. With proper mathematical manipulations, this constitutive model can represent many different empirical behaviors in a phenomenological way, i.e., softening/hardening and smoothly varying hysteresis curves, e.g., stiffness and strength degradation and the pinching effect.

Bouc-Wen models' can be considered as "semi-physical" models since they come from a combination of some physical understanding of the hysteresis system along with some kind of black-box modeling rather than a detailed analysis of the physical behavior of the systems with hysteresis [23]. This model essentially consists of a first-order non-linear differential equation relating an input displacement and an output restoring force in a hysteresis form. With the proper choice/tuning of parameters, it is possible to replicate the response of the model regarding real hysteresis behavior.

One example of the set of Bouc-Wen models is the Sivaselvan and Reinhorn smooth hysteresis model [11,24]. This model was developed based on previous models, viz., Bouc [25], Wen [26,27], Baber and Noori [28], Foliente [29], and Reinhorn et al. [30]. It is a versatile model that carries a physical interpretation that is appropriate to model the non-linear behavior of structural systems and structural components.

In this paper a parametric variation of a smooth hysteresis model based on the works of Sivaselvan and Reinhorn's [11,24] is performed, to evaluate the role of each parameter for further calibration, attempting to emulate the global cyclic behavior of an experimental RC frame structure using a macro model developed in MATLAB [31].

2. PARAMETRIC STUDY

2.1. Characteristics of the experimental frame structure

To study the cyclic response of RC frame structures with or without infill masonry walls an experimental campaign was performed at Laboratório Nacional de Engenharia Civil (LNEC) [32]. The RC bare frame structure used in this experimental study is represented in Figure 1a. A constant vertical load of 100 kN is applied at each column, and the structure is submitted to an increasing cyclical load/displacement pattern, as represented in Figure 1b, at the beam's center level.

The materials used in the experimental frame structure were concrete of the class C20/25, longitudinal steel reinforcement of S400, and transverse reinforcement (stirrups) of S500. At the critical regions, i.e., location of the expected plastic hinges, near the extremities of the structural members (Figure 1c), adequate concrete confinement is provided by tightening the spacing between the stirrups as detailed in Figure 1d.

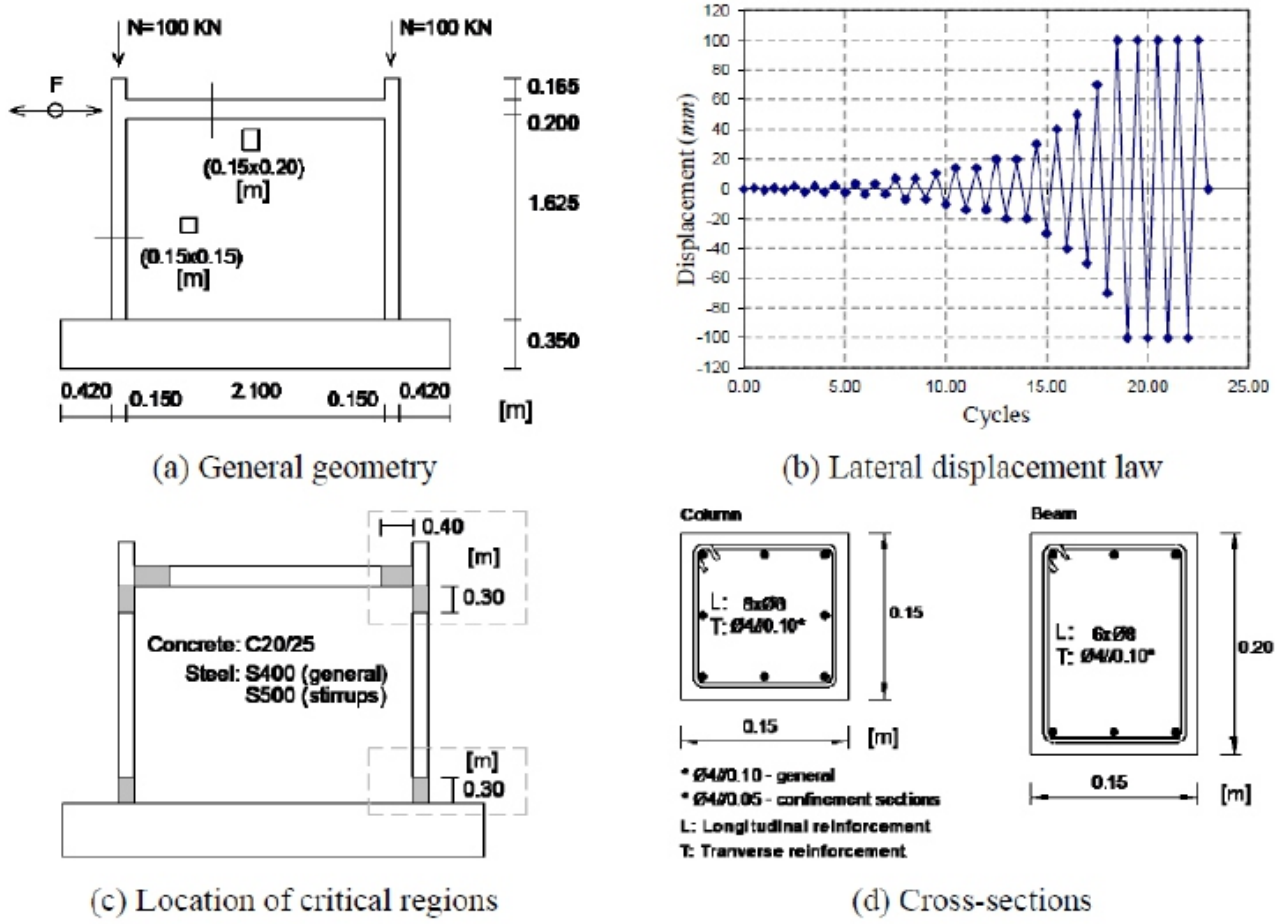

Figure 1. Reinforced concrete frame structure and respective confinement of the critical regions [33].

The experimental model was cyclically loaded in a quasi-statical way by displacement control, according to the displacement law in Figure 1b. Hence, the equation of motion will only comprise the restoring force, which will be further divided into the elastic and inelastic components. Having the displacement that the structure is subjected to and the structure's stiffness, the restoring force can be determined..

The following parametric variation will make use of the structural properties and loading conditions of the described experimental frame structure and testing, presenting all or only specific hysteresis cycles according to the current parameter under study.

2.2. Brief description of the smooth hysteresis model considered

Sivaselvan and Reinhorn developed a polygonal and a smooth hysteresis model [11,24] with degradation features. As mentioned, this modification to the original Bouc-Wen model offers a more physical understanding than preceding modifications since the parameters are selected in a way to have physical meaning. A brief description of the model used in this study is outlined below based on [11].

The model considered herein comprises three different springs (Figure 2): a post-yielding spring (Spring 1); a hysteresis spring (Spring 2), and a slip-lock spring (Spring 3).

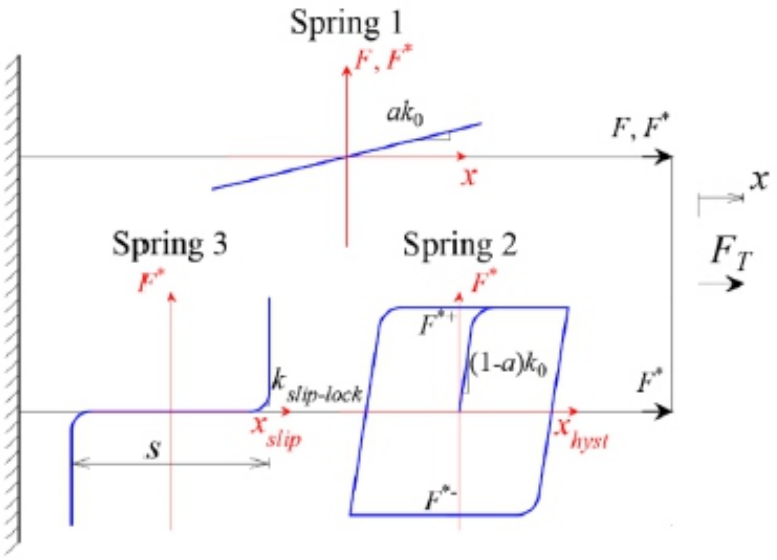

Figure 2. Springs set of the Sivaselvan and Reinhorn's smooth hysteresis model.

MATLAB was used to develop an algorithm to apply the aforementioned model. The differential equation that computes the hysteretic force is given in rate-dependent form as follows [11],

$$\dot{F}^* = k_{hyst}\dot{x} \Leftrightarrow \dot{F}^* = \dot{x}\left(R_K - a\right)k_0\left\{1 - \left|\frac{F^*}{F_Y^*}\right|^N \left[\eta_1 sgn\left(F^*\dot{x}\right) + \eta_2\right]\right\} \quad (1)$$

in which F* and F^*_Y are the hysteretic force and respective yielding force, x is the total displacement, k0 is the initial elastic stiffness, k_H is the total non-linear stiffness, k_{hyst} is the hysteretic stiffness, a is the post-yielding to initial stiffness ratio, N is the parameter controlling the smoothness transition from the elastic to the post-yielding range, and η_1 and η_2 are parameters controlling the shape of the unloading path. RK is related to stiffness degradation, having a positive decreasing value, [11]

$$R_K = \frac{F^* + \alpha F_Y^*}{k_0 x + \alpha F_Y^*} \quad (2)$$

where α controls the degree of stiffness degradation. In addition, stiffness degradation of the elastic spring, i.e., the post-yielding stiffness $k_{post\text{-}yield} = ak_0$, can also be considered, as used by other authors [3,34], by the following modification in the elastic spring

$$k_{post\text{-}yield,deg} = k_{post\text{-}yield}\left[1 - \eta_d\left(\frac{\left|x_{\max}^{+/-}\right|}{x_{ult}^{+/-}}\right)\right] \quad (3)$$

The slip lock stiffness, $k_{slip\text{-}lock}$, translated by Spring 3 is thus implemented in the model in series with the hysteresis spring to simulate pinching behavior. The combined stiffness can thus be obtained by the following expression [11]

$$k = k_{post\text{-}yield} + \frac{k_{hyst}k_{slip\text{-}lock}}{k_{hyst} + k_{slip\text{-}lock}} \quad \text{where} \quad k_{slip\text{-}lock} = \left\{\sqrt{\frac{2}{\pi}}\frac{s}{\sigma F_Y^*}exp\left[-\frac{1}{2}\left(\frac{F^* - \lambda F_Y^*}{\sigma F_Y^*}\right)^2\right]\right\}^{-1} \quad (4)$$

where s is the slip length, Rs controls the slip length, σ controls the fraction of the yield force beyond which slip will not occur, and λ defines the part of yield force about which slip will occur.

The deterioration of the strength capacity can be simulated by using a rule based on continuous energy degradation and backbone degradation due to the exceeded maximum deformation. This rule can be given by the following expression [11]

$$F_Y^{+/-} = F_{Y0}^{+/-}\left[1-\left(\frac{x_{max}^{+/-}}{x_{ult}^{+/-}}\right)^{\frac{1}{\beta_1}}\right]\left[1-\frac{\beta_2}{1-\beta_2}\frac{E_h}{E_{hult}}\right] \quad (5)$$

where $FY^{+/-}$ and $F_{y0}^{+/-}$ are the yield force and the initial yield force, respectively, $x_{max}^{+/-}$ is the maximum displacement, $x_{ult}^{+/-} = x_Y \times \mu_{ult}^{+/-}$ is the ultimate displacement (product between the yield displacement and the ultimate ductility factor), and β_1 and β_2 are parameters based on ductility and energy demands, respectively. The hysteresis energy can be given in incremental form as follows [11]:

$$\Delta E_h = \left[\frac{F+(F+\Delta F)}{2}\right]\left(\Delta x - \frac{\Delta F}{R_K k_0}\right) \quad (6)$$

and the ultimate hysteretic energy under monotonic loading until the ultimate deformation without degradation can be computed by the following expression

$$E_{hult} = \frac{F_{Y0}x_Y}{2} + F_{Y0}\left(x_{ult} - x_Y\right) \quad (7)$$

Asymmetric yielding can also be considered by using the following expression [11]:

$$F_Y^* = (1-a)\left[\left(\frac{1+\mathrm{sgn}(\dot{x})}{2}\right)F_Y^+ + \left(\frac{1-\mathrm{sgn}(\dot{x})}{2}\right)F_Y^-\right] \quad (8)$$

The experimental model was loaded in a quasi-static cyclic way. Hence, Eq 1 is rewritten for quasi-statically loaded systems, eliminating dt and noting that sgn(ẋ) = sgn(dx) [30], considering now the motion independent of time,

$$\begin{aligned} &\frac{dF^*}{dt} = \frac{dx}{dt}(R_K - a)k_0\left\{1-\left|\frac{F^*}{F_Y^*}\right|^{n_w}\left[\eta_1 sgn\left(F^*\frac{dx}{dt}\right)+\eta_2\right]\right\} \\ &\Leftrightarrow dF^* = dx(R_K - a)k_0\left\{1-\left|\frac{F^*}{F_Y^*}\right|^{n_w}\left[\eta_1 sgn\left(F^* dx\right)+\eta_2\right]\right\} \end{aligned} \quad (9)$$

and the non-linear equation is solved using a numerical solver such as functions, f_{zero}, f_{solve}, or vpasolve [31].

2.3. Model parameters variation

The following parametric variation investigates the meaning and the influence of each parameter in the above-presented model. The first graph of Figures 3–13 corresponds to the 18th cycle for different parameter values, and the second plot is the complete hysteretic response for specific parameters' values.

2.3.1. Parameter N

Figure 3 presents the variation of parameter N, controlling the smoothness transition from preto the post-yielding range. As can be observed the model becomes approximately bilinear from N = 15, showing very little variation between this value and the last one considered (N = 250).

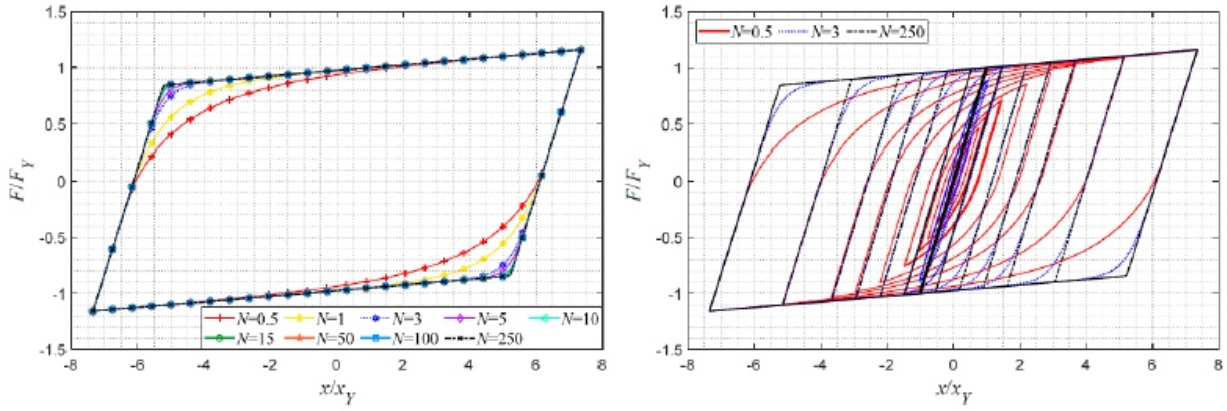

Figure 3. Variation of parameter N (R_s = 0, σ = 1, λ = 0, α = 50, η = 0.5, η_d = 0, a = 0.025, $\beta_1 = \beta_2$ = 0).

2.3.2. Parameters η_1 and η_2

These two parameters can be reduced to one, η, if one considers the following operation: $\eta_1 + \eta_2 = 1$, leading to [11]:

$$\dot{F}^* = k_{hyst}\dot{x} \Leftrightarrow \dot{F}^* = \dot{x}(R_K - a)k_0\left\{1 - \left|\frac{F^*}{F_Y^*}\right|^N \left[\eta sgn\left(F^*\dot{x}\right) + \eta - 1\right]\right\} \quad (10)$$

This is the result of prior studies [35,36], that suggest parameter A (in the original model [26]) is equal to one (Eq 1 and 10) due to redundancies in the model and for mathematical consistency, restoring the physical significance of the initial stiffness; and the previous operation ($\eta_1 + \eta_2 = 1$) is considered for compatibility with plasticity, i.e., returns the physical meaning of the yield force. It should be referred that these values correspond, respectively, to β and γ in the original model [26].

Variation of parameter η is presented in Figure 4 as combinations of η_1 and η_2. It can be verified that this parameter or parameters control the shape of the unloading path, i.e., the variation of the unloading stiffness, as well as the size of the hysteresis loop, in terms of area and shape. Parameter η will take only positive real values, which corresponds to positive real values for η_1 and positive or negative real values for η_2. When $\eta < 0.5$ the discharge path is linear. For $\eta < 0.5$ the unloading path is non-linear, compressing the loop area, and thus reducing the energy dissipation. For $\eta > 0.5$ the unloading path is also non-linear, although the loop area increases by slightly enlarging the cycle.

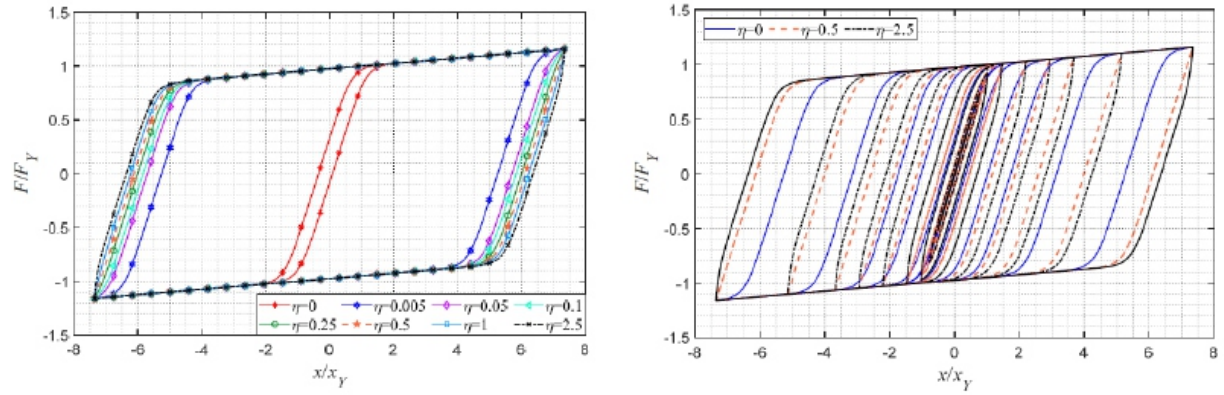

Figure 4. Variation of parameter η (R_s = 0; σ = 1; λ = 0; α = 100; N = 5; $η_d$ = 0; a = 0.025; $β_1$ = $β_2$ = 0).

Other parametric studies [36,37] revealed that if parameters $η_1$ and $η_2$ are allowed to vary independently in the context of the original Bouc-Wen model, softening and hardening hysteresis behavior can be obtained for larger and smaller values of $η_1$, respectively.

2.3.3. Parameters a and $η_d$

Figures 5 and 6 show, respectively, the variation of the values of parameters a and $η_d$, while fixing the remaining parameters.

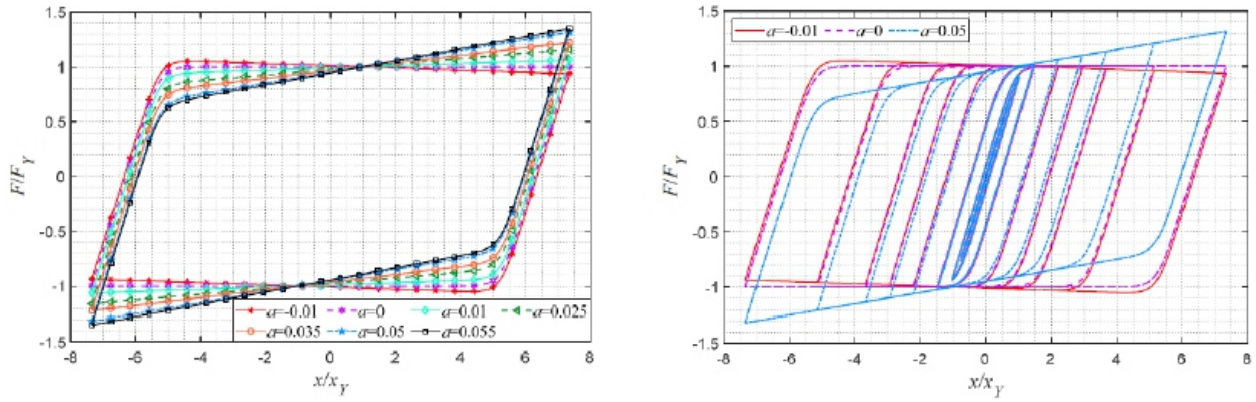

Figure 5. Variation of parameter a (R_s = 0, σ = 1, λ = 0, N = 5, η = 0.5, ηd = 0, α = 100, $β_1$ = $β_2$ = 0).

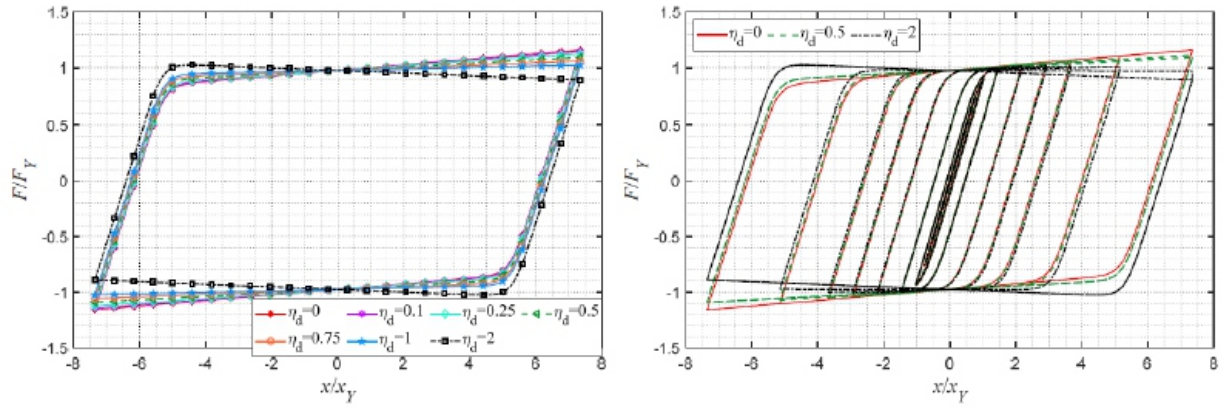

Figure 6. Variation of parameter ηd (R_s = 0, σ = 1, λ = 0, N = 5, η = 0.5, α = 100, a = 0.025, $β_1$ = $β_2$ = 0).

As mentioned, parameter a accounts for the value of stiffness after yielding, i.e., in the plastic range. This parameter may be seen as a percentage of the initial elastic stiffness. Recent studies [38,39] proposed the use of negative values for this parameter, resulting in a strain-softening behavior after yielding. Hence, this variation also accounts for negative values of a. The effect of a negative value of parameter a leads to a clockwise rotation of the hysteresis loops, which allied to the softening behavior results in an increase of strength capacity at the end of the reloading phase, since this model is a Masing type hysteresis model.

The degradation of the post-yielding stiffness can also be implemented in the model [3,34] using the degradation parameter η_d, whose effect presented in Figure 6 reveals higher degradation for larger values of the maximum displacement and parameter η_d.

2.3.4. Parameter α

Hysteresis stiffness degradation is regulated by parameter α, which takes positive real values. This parameter is implemented in the pivot rule [20], leading to a positive decreasing function, R_k (Eq 2), with the unity as its initial and maximum value.

From Figure 7 it is evident that for larger values of α the less stiffness degradation occurs. For values of α between 50 and 250, stiffness degradation is almost inexistent. Despite the influence in the stiffness of the unloading path, an obvious correlation with the hysteresis energy dissipation is seen by observing the reduced area of the hysteresis loops.

Severe stiffness degradation can be verified for values below α = 5. Values of α below 0.5 may not represent results with physical significance.

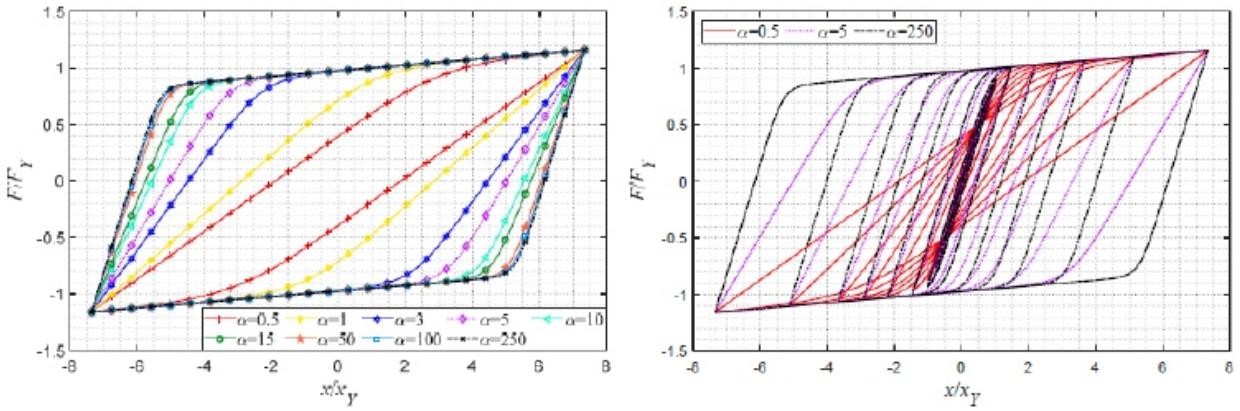

Figure 7. Variation of parameter α (R_s = 0, σ = 1, λ = 0, N = 5, η = 0.5, η_d = 0, a = 0.025, β_1 = β_2 = 0). 2.3.5. Parameters β_1 and β_2

Figures 8 and 9 show the variation of the parameters controlling the strength deterioration in terms of ductility and energy demands, respectively, β_1 and β_2.

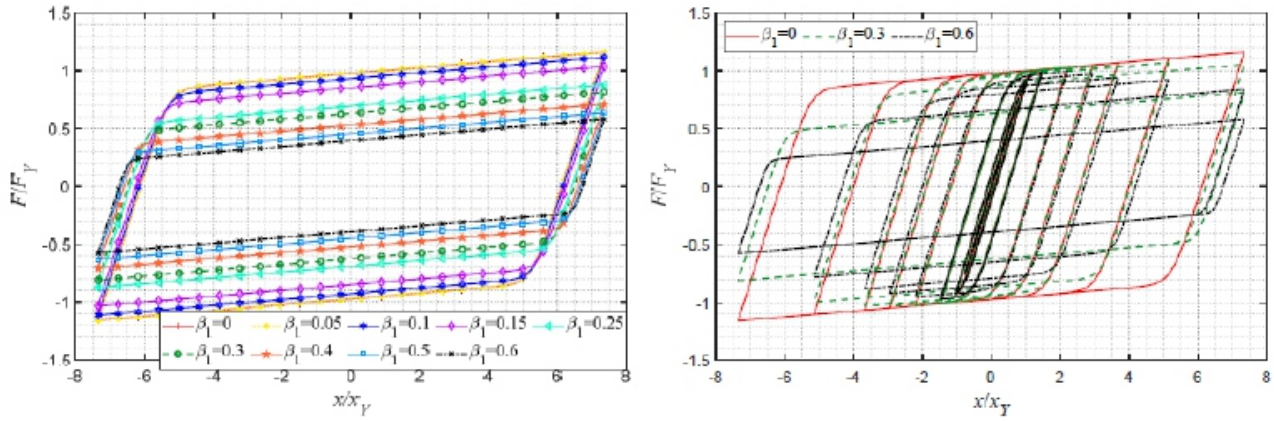

Figure 8. Variation of parameter β_1 (R_s = 0, σ = 1, λ = 0, N = 5, α = 100, η = 0.5, η_d = 0, a = 0.025, β_2 = 0).

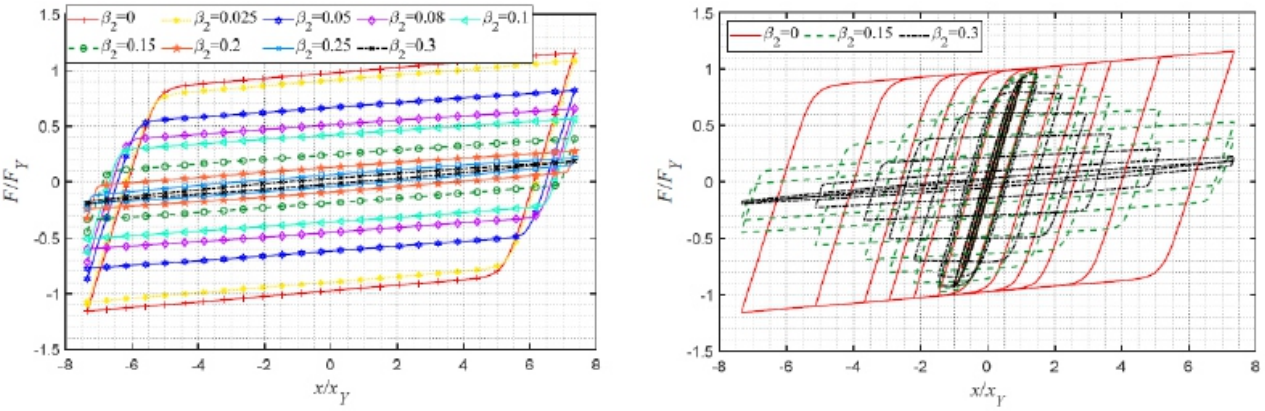

Figure 9. Variation of parameter β_2 (R_s = 0; σ = 1; λ = 0; N = 5; α = 100, η = 0.5; η_d = 0; a = 0.025; β_1 = 0).

Parameter β_1 depends on the maximum displacement achieved as can be verified by the second term of Eq 5. Hence, whenever a maximum displacement is attained, degradation of the strength capacity occurs by reducing the backbone curve's ordinate. Figure 8 shows severe strength degradation for values between 0.4 and 0.6, and minor strength deterioration for values below 0.1.

Different from β_1, parameter β_2 exhibits continuous resistance degradation based on the incremental energy dissipation. This leads to greater degrees of deterioration for smaller values of β_2 compared with β1. As can be observed severe resistance degradation can be verified for values of β_2 above 0.15. Values above 0.3 led to numerical instabilities for this case under study.

2.3.6. Parameters R_s, σ, and λ

In this subsection variation of the parameters' values related to the pinching effect is carried out, viz., parameters R_s, σ and λ.

The slip length s (Figure 2) is regulated by parameter R_s that possess positive real values. The higher the value of R_s the more pronounced the pinching effect is as can be observed by Figure 10.

The severe pinching effect can be verified for values bigger than Rs = 0.4, and minor pinching effect for very small values of this parameter.

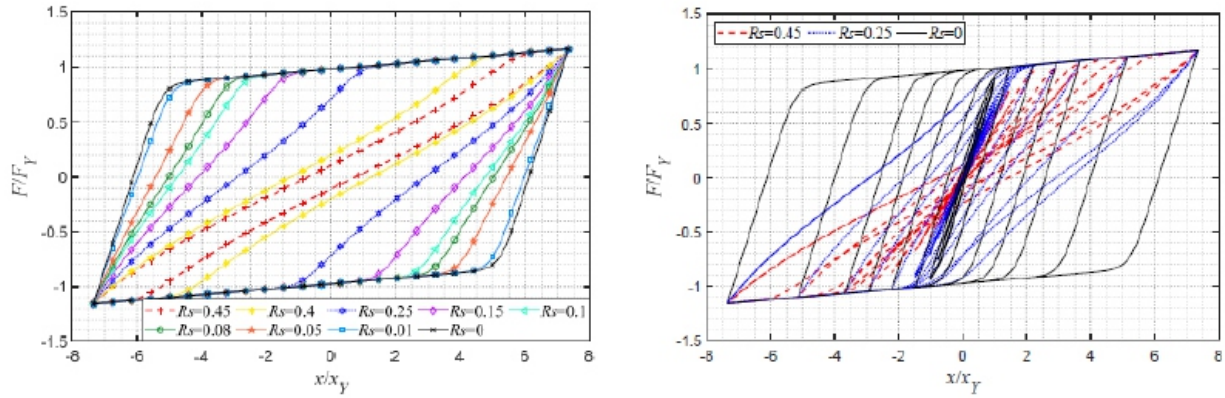

Figure 10. Variation of parameter R_s ($\sigma = 0.75$, $\lambda = 0$, N = 5, $\alpha = 100$, $\eta = 0.5$, $\eta_d = 0$, a = 0.025, $\beta_1 = \beta_2 = 0$).

The effect of parameter σ is clear by the observation of Figure 11, focusing the pinching effect in a smaller region near the center for smaller values of σ. Slip or the pinching effect will not occur beyond the fraction defined by σ. A value of σ near the unity leads to an almost uniform distribution of the pinching effect in the loading/reloading and unloading branches. Numerical instabilities occur for values of σ very close to zero.

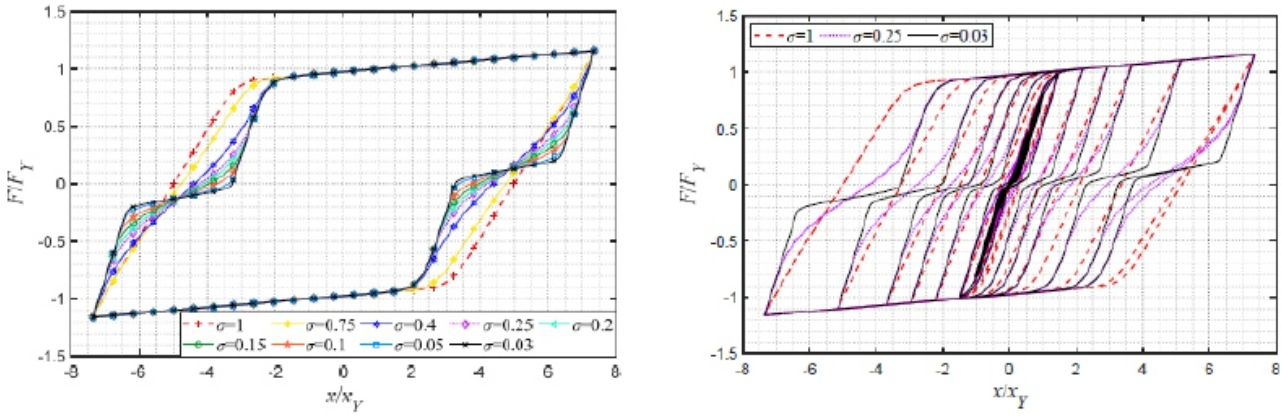

Figure 11. Variation of parameter σ ($R_s = 0.1$, $\lambda = 0$, N = 5, $\alpha = 100$, $\eta = 0.5$, $\eta_d = 0$, a = 0.025, $\beta_1 = \beta_2 = 0$).

Parameter λ defines the location around which slip will occur. It can take positive or negative real values, and has the positive or negative unity as its maximum or minimum value, respectively. A value different from zero introduces an asymmetric pinching effect in the numerical model. A null value for this parameter means that the structural element or the structure is symmetric. Figure 12 shows the effect of this parameter, which becomes more pronounced for values close to positive or negative one.

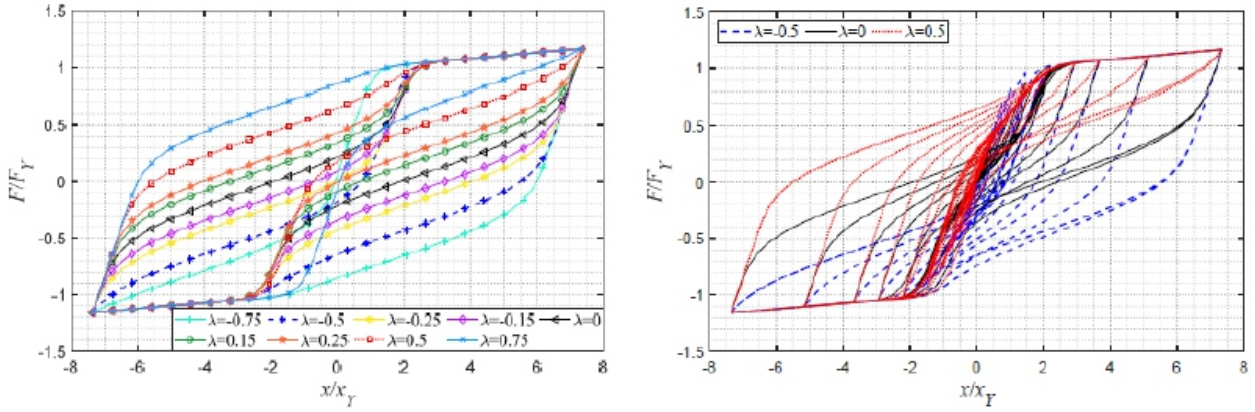

Figure 12. Variation of parameter λ (R_s = 0.25, σ = 0.25, N = 5, α = 50, η = 0.5, η_d = 0, a = 0.025, $\beta_1 = \beta_2 = 0$).

2.3.7. Asymmetric yielding

Asymmetric yielding can be considered by the use of Eq 8. Figure 13 shows this feature by varying the yield force in the negative direction to have lower and higher yielding levels than in the positive direction. This feature is important since structural systems are not perfect or ideal, and yielding will possibly have different values in opposite directions.

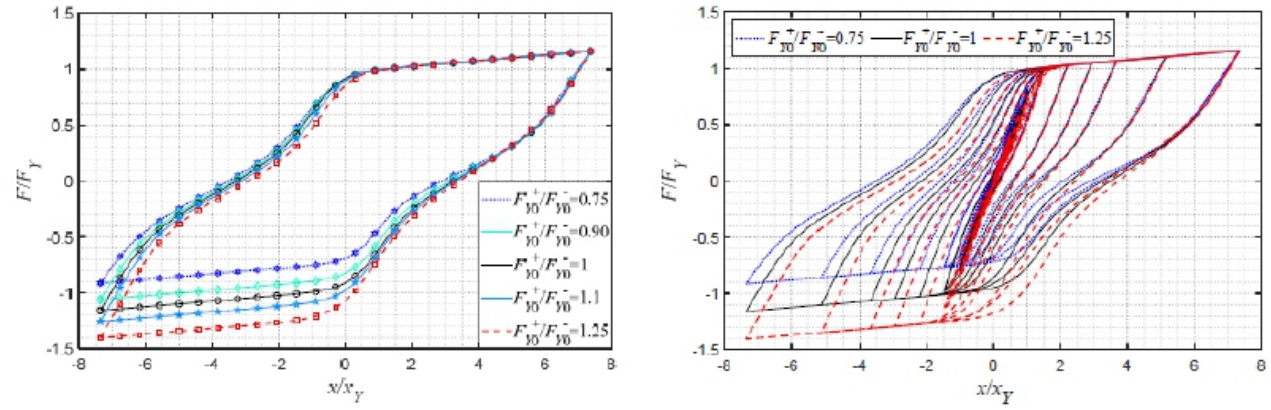

Figure 13. Variation of the yield force in the negative direction (R_s = 0.1, σ = 0.25, λ = 0, N = 5, α = 5, η = 0.5, η_d = 0, a = 0.025, $\beta_1 = \beta_2 = 0$).

3. CALIBRATION OF MODEL PARAMETERS

The cyclic response of the RC experimental bare frame is presented in Figure 14a. It can be verified a smooth evolution with a subsequent maximum before concrete cracking at the top and bottom ends of the columns. Then, a gradual stiffness decrease occurs without collapse, although with substantial damage, strength deterioration, and inelastic hinge spread in the columns.

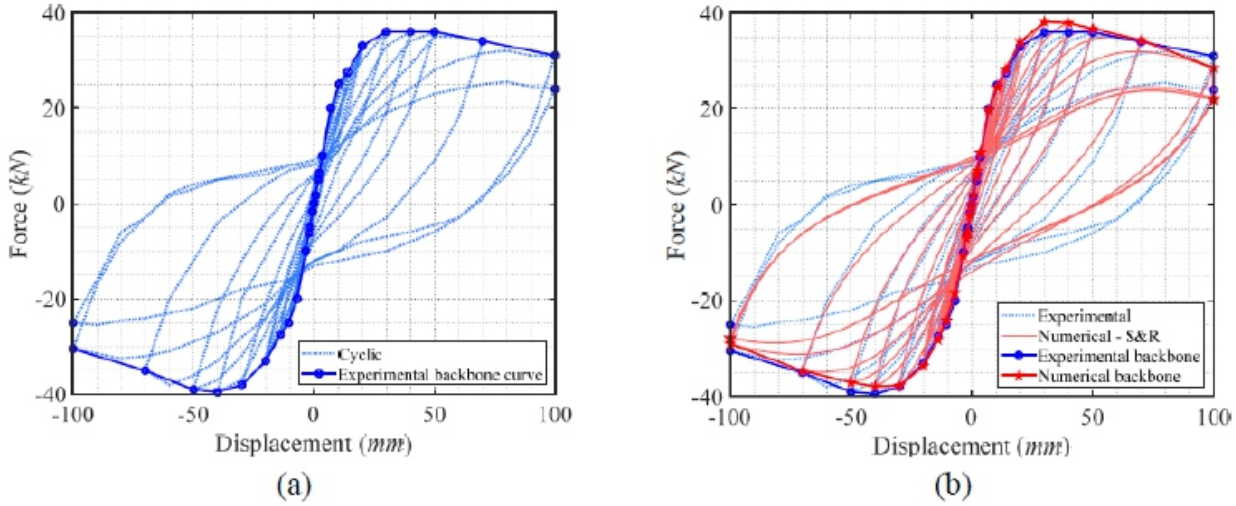

Figure 14. Cyclic response and corresponding backbone curve of the RC frame structure. (a) Experimental, (b) numerical.

Based on the previous parametric study that investigated the influence and effect of each parameter in the hysteresis response, an optimization procedure is carried out to search for the parameters' values that provide the best fit to the experimental data.

The optimal parameters' values defining the smooth hysteresis model that provide the best fitting to the experimental data are obtained by following the procedure illustrated in Figure 15 through a flowchart. The procedure starts with a manual calibration to obtain a starting point or initial guess of the hysteretic parameters for the implementation of function lsqcurvefit in MATLAB [31]. This function aims to minimize the sum of squares error between the numerical and experimental results of the restoring force. The optimized results with this function are then used as an initial guess for the use of function, fminsearchbnd [40], based on the fminsearch function algorithm [31] that follows the Nelder-Mead simplex algorithm, although with bound constraints applied to the parameters. This function aims to minimize the root mean square error (RMSE) of the same results mentioned, with emphasis given to the points belonging to the cyclic backbone curve through the use of weighting factors. This error was further normalized (NRMSE) with the range of the experimental restoring force and converted to a percentage. The stopping criteria considered for a converged solution were an NRMSE less than 5% and a tolerance less than 1×10^{-4} for the difference between two subsequent iterations on the calculation of the NRMSE.

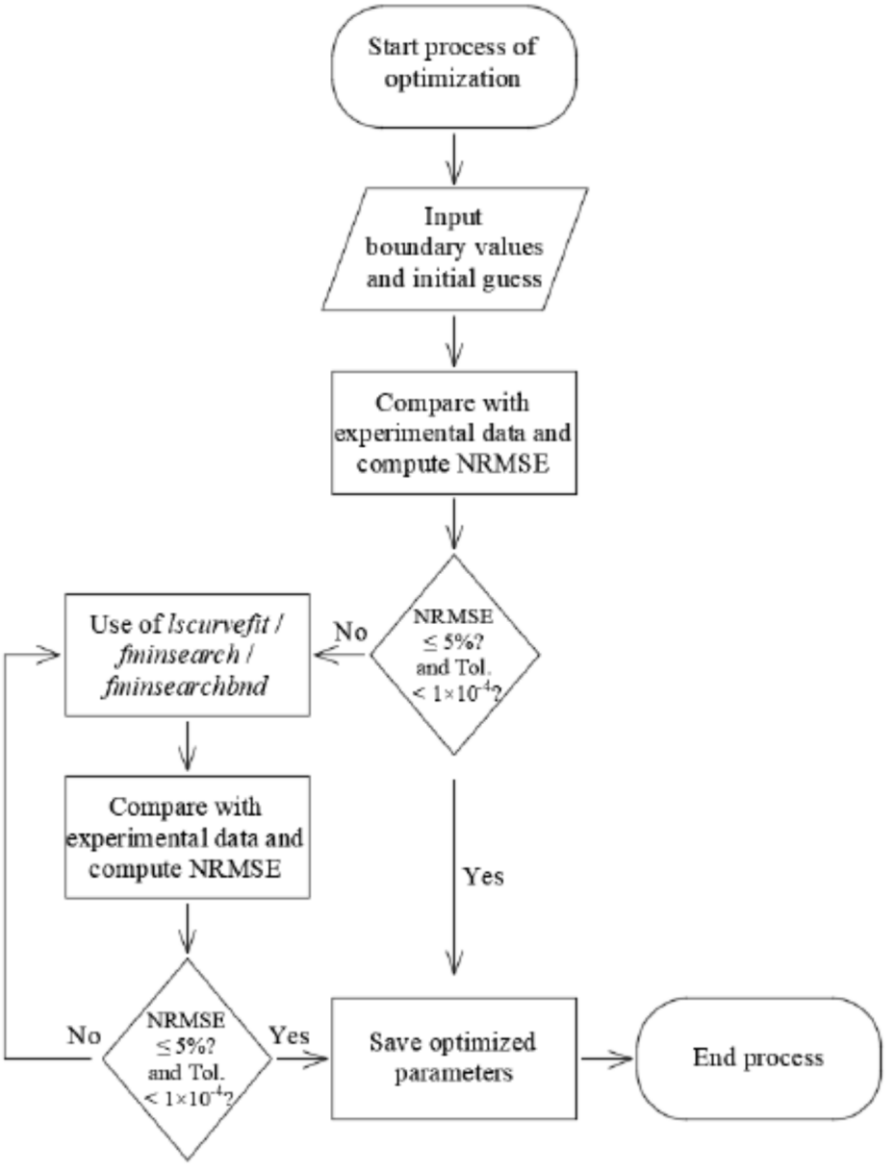

Figure 15. Flowchart of the optimization procedure undertaken in the present study.

The initial stiffness and the yielding force in both directions were also considered in the optimization procedure, verifying that the optimum values are relatively close to the actual values. Figure 14b presents the outcome of the optimization with the following optimized parameters: $N = 2.07$, $a = -0.061$, $\eta_d = 0$, $\eta = 0.81$, $\alpha = 1.33$, $\beta_1 = 0.03$, $\beta_2 = 0.005$, $R_s = 0.17$, $\sigma = 0.40$, $\lambda = 0.004$, $k_0 = 3.567 \times 106$ N/m, $F^{+}_{Y0} = 4.8203 \times 104$ N, $F_{y0} = 4.9907 \times 104$ N, $\mu^{+}_{ult} = 7.85$, $\mu^{-}_{ult} = 14.85$. The model can reasonably estimate the cyclic backbone curve as well as the global hysteretic cycles. The model presents some setbacks in the estimation of the experimental unloading branches and transitions from elastic to plastic range. In addition, further improvements may be applied in the model for the present purpose, viz., in the strength degradation parameters, whose influence and numerical values seem to not correspond to the level of deterioration in the experimental model, taking very small values. However, the small values of these parameters might be explained by the high degree of stiffness degradation and pinching effect.

The functions used for optimization gave satisfactory results, though a large number of variables were used, exceeding their limit of good performance. As a future development, an optimization procedure should be created to verify if a better solution exists to fit the experimental data.

4. CONCLUSIONS

The parametric study performed herein highlighted the importance of each parameter in the hysteresis model investigated. The knowledge of the effect of each parameter in the model provides the necessary insight into the possibilities of the model to estimate real behavior, in the present scope, the non-linear cyclic behavior of RC frame structures.

Based on the parametric study carried out, the calibration of the model's parameters was performed using an optimization procedure to replicate the cyclic behavior of an experimental RC bare frame structure. Satisfactory results were obtained, though a large number of variables were used in the process of optimization, which may compromise the good performance of the implemented functions. Hence, a different optimization approach should be considered to support the current and future solutions.

Further improvements may be carried out for the present purpose, namely, to the strength deterioration formulation to better predict the experimental response, since the values obtained for the corresponding parameters are very small, which may not represent the actual behavior of deterioration. Nevertheless, the level of stiffness degradation and the pinching effect may also explain such low values of the strength deterioration parameters.

Future investigations may comprise validation of the studied hysteresis model with more experimental data considering different hysteretic configurations.

ACKNOWLEDGMENTS

This paper is within the scope of the first author's Ph.D. degree in progress, financially supported by the Portuguese Foundation for Science and Technology (FCT) through the PhD grant reference SFRH/BD/139570/2018 under the programme POCH (N2020-P2020) and subsidized by the European Social Fund (FSE) and national funds from MCTES. This work was financially supported by: Base Funding-UIDB/04708/2020 of the CONSTRUCT-Instituto de I&D em Estruturas e Construções-funded by national funds through the FCT/MCTES (PIDDAC).

CONFLICT OF INTEREST

There is no conflict of interests with the authors and the publication of this paper.

REFERENCES

1. *Krasnosel'skij MA, Pokrovskij AV (1983) Systems with Hysteresis, Berlin, Germany: Springer.*
2. *Visintin A (1994) Differential Models of Hysteresis. Berlin Heidelberg, Germany: Springer-Verlag.*
3. *Apostolos B (2017) Effects of strength hardening, stiffness degradation, strength deterioration and pinching on the seismic response of SDoF systems [Master's thesis]. Delft University of Technology, The Netherlands.*
4. *Federal Emergency Management Agency (FEMA) (2009) Effects of strength and stiffness degradation on seismic response, P440A, California.*
5. *Otani S (2002) Nonlinear earthquake response analysis of reinforced concrete buildings. University of Tokyo, Japan.*
6. *Vaiana N, Sessa S, Marmo F, et al. (2018) A class of uniaxial phenomenological models for simulating hysteretic phenomena in rate-independent mechanical systems and materials. Nonlinear Dynam 93: 1647–1669.*
7. *Vaiana N, Sessa S, Rosati L (2021) A generalized class of uniaxial rate-independent models for simulating asymmetric mechanical hysteresis phenomena. Mech Syst Signal Pr 146: 106984.*
8. *Vaiana N, Capuano R, Sessa S, et al. (2021) Nonlinear dynamic analysis of seismically base-isolated structures by a novel openSees hysteretic material model. Appl Sci 11: 900.*
9. *Do T, Filippou F (2017) A damage model for structures with degrading response. Earthq Eng Struct D 47: 311–332.*

10. *Mazza F (2019) A plastic-damage hysteretic model to reproduce strength stiffness degradation. B Earthq Eng 17: 3517–3544.*
11. *Sivaselvan M, Reinhorn A (2000) Hysteretic models for deteriorating inelastic structures. J Eng Mech 126: 633–640.*
12. *Clough RW (1966) Effects of stiffness degradation on earthquake ductility requirement, UCB/SESM 1966/16, University of California, Berkeley, USA.*
13. *Nielsen N, Imbeault F (1971) Validity of various hysteretic systems, Proceedings of the 3rd Japan National Conference on Earthquake Engineering, 707–714.*
14. *Otani S (1981) Hysteresis model of reinforced concrete for earthquake response analysis. J Fac Eng 36: 407–441.*
15. *Fukada Y (1969) Study on the restoring force characteristics of reinforced concrete buildings, Proceedings Kanto Branch Symposium, Architectural Institute of Japan, 40: 121–124 (in Japanese).*
16. *Takeda T, Sozen M, Nielsen N (1970) Reinforced concrete response to simulated earthquakes. J Struct Div 96: 2557–2573.*
17. *Takeda T, Sozen MA, Nielsen NN (1971) Reinforced concrete response to simulated earthquakes, OHBAYASHI-GUMI Technical Research Report 5, 19–26, Tokyo, Japan.*
18. *Eto H, Takeda T (1973) Elasto plastic earthquake response analysis of reinforced concrete frame structure, Architectural Institute of Japan, 1261–1262, Tokyo, Japan (in Japanese).*
19. *Kabeyasawa T, Shiohara H, Otani S, et al. (1983) Analysis of the full-scale seven-story reinforced concrete test structure. J Fac Eng 37: 431–478.*
20. *Park Y, Reinhorn A, Kunnath S (1987) IDARC: Inelastic Damage Analysis of Reinforced Concrete Frame-Shear-Wall Structures, NCEER-87-0008, National Center for Earthquake Engineering Research, University at Buffalo, State University of New York, Buffalo, New York, USA.*
21. *Costa AG, Costa AC (1987) Modelo histerético das relações forças-deslocamentos adequado à análise sísmica de estruturas, Laboratório Nacional de Engenharia Civil (LNEC), Lisbon, Portugal.*
22. *Rodrigues H, Varum H, Costa A (2005) Modelo numérico não-linear para painéis de alvenaria de enchimento em pórticos de betão armado, VII Congreso de Métodos Numéricos en Ingeniería (SEMINI) and IX Congresso Nacional de Mecânica Aplicada e Computacional (APMTAC), 381: 4–7, Granada, Spain.*
23. *Ismail M, Ikhouane F, Rodellar J (2009) The hysteresis Bouc-Wen model, a survey. Arch Comput Method E 16: 161–188.*
24. *Sivaselvan M, Reinhorn A (1999) Hysteretic models for cyclic behavior of deteriorating inelastic structures, MCEER-99-0018, Multidisciplinary Center for Earthquake Engineering Research, New York.*
25. *Bouc R (1968) Forced vibration of mechanical systems with hysteresis, In: Rupakhety R, Olafsson S, Bessaon B, Proceedings of the Fourth Conference on Non-linear Oscillation, Prague: Academia.*
26. *Wen Y (1976) Method for random vibration of hysteretic systems. J Eng Mech-ASCE 102: 249–263.*
27. *Wen Y (1980) Equivalent linearization for hysteretic system under random excitation. J Appl Mech 47: 150–154.*
28. *Baber TT, Noori MN (1985) Random vibration of degrading pinching systems. J Eng Mech-ASCE 11: 1010–1026.*
29. *Foliente G (1995) Hysteresis modeling of wood joints and structural systems. J Struct Eng 121: 1013–1022.*
30. *Reinhorn A, Mandan A, Valles R, et al. (1995) Modeling of masonry infill panels for structural analysis, NCEER-95-0018, National Center for Earthquake Engineering, USA.*
31. *The MathWorks, Inc, MATLAB R2019a 9.6.0.1072779, Natick, Massachusetts, USA.*
32. *Pires F (1990) Influência das paredes de alvenaria no comportamento de estruturas reticuladas de betão armado sujeitas a acções horizontais [PhD Thesis]. LNEC, Lisboa.*
33. *Braz-César M, Oliveira D, Barros R (2008) Comparison of cyclic response of reinforced concrete infilled frames with experimental results. 14th World Conference on Earthquake Engineering, Beijing, China.*
34. *Ray T, Reinhorn A (2014) Enhanced smooth hysteretic model with degrading properties. J Struct Eng 140: 04013028.*
35. *Ma F, Zhang H, Bockstedte A, et al. (2004) Parameter analysis of the differential model of hysteresis. J Appl Mech 71: 342–349.*
36. *Charalampakis A (2010) Parameters of Bouc-Wen hysteretic model revisited. 9th HSTAM International Congress on Mechanics, Cyprus.*
37. *Braz-César M, Barros R (2013) Experimental and numerical analysis of MR dampers. 4th ECCOMAS Thematic Conference on Computational Methods in Structural Dynamics and Earthquake Engineering, Greece.*
38. *Tsiatas GC, Charalampakis AE (2018) A new hysteretic nonlinear energy sink (HNES). Commun Nonlinear Sci 60: 1–11.*

39. Charalampakis A, Tsiatas G (2018) Effects of hysteresis and negative stiffness on seismic response rreduction: A case study based on the 1999 Athens, Greece earthquake. Front Built Environ 4: 00023.
40. D'Errico J, fminsearchbnd, fminsearchcon. MATLAB Central File Exchange, 2021. Available from: https:/ /www.mathworks.com/matlabcentral/fileexchange/8277-fminsearchbnd-fminsearchcon.

Instructions for Authors

Essentials for Publishing in this Journal

1 Submitted articles should not have been previously published or be currently under consideration for publication elsewhere.

2 Conference papers may only be submitted if the paper has been completely re-written (taken to mean more than 50%) and the author has cleared any necessary permission with the copyright owner if it has been previously copyrighted.

3 All our articles are refereed through a double-blind process.

4 All authors must declare they have read and agreed to the content of the submitted article and must sign a declaration correspond to the originality of the article.

Submission Process

All articles for this journal must be submitted using our online submissions system. http://enrichedpub.com/ . Please use the Submit Your Article link in the Author Service area.

Manuscript Guidelines

The instructions to authors about the article preparation for publication in the Manuscripts are submitted online, through the e-Ur (Electronic editing) system, developed by **Enriched Publications Pvt. Ltd**. The article should contain the abstract with keywords, introduction, body, conclusion, references and the summary in English language (without heading and subheading enumeration). The article length should not exceed 16 pages of A4 paper format.

Title

The title should be informative. It is in both Journal's and author's best interest to use terms suitable. For indexing and word search. If there are no such terms in the title, the author is strongly advised to add a subtitle. The title should be given in English as well. The titles precede the abstract and the summary in an appropriate language.

Letterhead Title

The letterhead title is given at a top of each page for easier identification of article copies in an Electronic form in particular. It contains the author's surname and first name initial .article title, journal title and collation (year, volume, and issue, first and last page). The journal and article titles can be given in a shortened form.

Author's Name

Full name(s) of author(s) should be used. It is advisable to give the middle initial. Names are given in their original form.

Contact Details

The postal address or the e-mail address of the author (usually of the first one if there are more Authors) is given in the footnote at the bottom of the first page.

Type of Articles

Classification of articles is a duty of the editorial staff and is of special importance. Referees and the members of the editorial staff, or section editors, can propose a category, but the editor-in-chief has the sole responsibility for their classification. Journal articles are classified as follows:

Scientific articles:

1. Original scientific paper (giving the previously unpublished results of the author's own research based on management methods).

2. Survey paper (giving an original, detailed and critical view of a research problem or an area to which the author has made a contribution visible through his self-citation);

3. Short or preliminary communication (original management paper of full format but of a smaller extent or of a preliminary character);

4. Scientific critique or forum (discussion on a particular scientific topic, based exclusively on management argumentation) and commentaries. Exceptionally, in particular areas, a scientific paper in the Journal can be in a form of a monograph or a critical edition of scientific data (historical, archival, lexicographic, bibliographic, data survey, etc.) which were unknown or hardly accessible for scientific research.

Professional articles:

1. Professional paper (contribution offering experience useful for improvement of professional practice but not necessarily based on scientific methods);
2. Informative contribution (editorial, commentary, etc.);
3. Review (of a book, software, case study, scientific event, etc.)

Language

The article should be in English. The grammar and style of the article should be of good quality. The systematized text should be without abbreviations (except standard ones). All measurements must be in SI units. The sequence of formulae is denoted in Arabic numerals in parentheses on the right-hand side.

Abstract and Summary

An abstract is a concise informative presentation of the article content for fast and accurate Evaluation of its relevance. It is both in the Editorial Office's and the author's best interest for an abstract to contain terms often used for indexing and article search. The abstract describes the purpose of the study and the methods, outlines the findings and state the conclusions. A 100- to 250-Word abstract should be placed between the title and the keywords with the body text to follow. Besides an abstract are advised to have a summary in English, at the end of the article, after the Reference list. The summary should be structured and long up to 1/10 of the article length (it is more extensive than the abstract).

Keywords

Keywords are terms or phrases showing adequately the article content for indexing and search purposes. They should be allocated heaving in mind widely accepted international sources (index, dictionary or thesaurus), such as the Web of Science keyword list for science in general. The higher their usage frequency is the better. Up to 10 keywords immediately follow the abstract and the summary, in respective languages.

Acknowledgements

The name and the number of the project or programmed within which the article was realized is given in a separate note at the bottom of the first page together with the name of the institution which financially supported the project or programmed.

Tables and Illustrations

All the captions should be in the original language as well as in English, together with the texts in illustrations if possible. Tables are typed in the same style as the text and are denoted by numerals at the top. Photographs and drawings, placed appropriately in the text, should be clear, precise and suitable for reproduction. Drawings should be created in Word or Corel.

Citation in the Text

Citation in the text must be uniform. When citing references in the text, use the reference number set in square brackets from the Reference list at the end of the article.

Footnotes

Footnotes are given at the bottom of the page with the text they refer to. They can contain less relevant details, additional explanations or used sources (e.g. scientific material, manuals). They cannot replace the cited literature.
The article should be accompanied with a cover letter with the information about the author(s): surname, middle initial, first name, and citizen personal number, rank, title, e-mail address, and affiliation address, home address including municipality, phone number in the office and at home (or a mobile phone number). The cover letter should state the type of the article and tell which illustrations are original and which are not.

Address of the Editorial Office:

Enriched Publications Pvt. Ltd.
S-9,IInd FLOOR, MLU POCKET,
MANISH ABHINAV PLAZA-II, ABOVE FEDERAL BANK,
PLOT NO-5, SECTOR -5, DWARKA, NEW DELHI, INDIA-110075,
PHONE: - + (91)-(11)-45525005

Note